Phase Behaviour of Colloidal Fluids with Competing Attractive and Repulsive Effective Potentials

Wheater, Rhys

Award date:
2016

Awarding institution:
University of Bath

Phase Behaviour of Colloidal Fluids with Competing Attractive and Repulsive Effective Potentials

Rhys James Wheater

A thesis submitted for the degree of Doctor of Philosophy

University of Bath
Department of Physics

September 2015

COPYRIGHT

Abstract

For some time it was believed that simple, single - component, fluid phase behaviour was limited to a homogeneous gas and homogeneous liquid phase separated by a line of first order phase transitions. However, recent studies have demonstrated that simple fluid behaviour can be extended to richer phase diagrams through tuning of the effective potential.

Fluids whose constituent particles feel a strong attraction at close range and weak repulsion at longer ranges have been shown, under certain conditions, to assemble into heterogeneous structures such as spherical and cylindrical clusters, lamellae and spherical and cylindrical voids.

Lattice Monte Carlo simulations are used to explore the phase diagram of a single - component fluid following a hard - core effective potential with an attractive and a repulsive Yukawa tail. The relative strengths of attractive and repulsive potentials are found for which heterogeneous structures become stable. Then the region of stability of heterogeneous structures is delimited through the use of histogram reweighting to map out the locus of points at which the homogeneous and heterogeneous states have equal free energy. A transition matrix Monte Carlo biasing technique is used to reveal the system behaviour inside the free - energy barrier at low temperatures, when the gas - liquid phase transition appears to have re-asserted itself. Finally, a discussion as to the mechanism for assembly of the heterogeneous structures is offered.

Acknowledgements

Special thanks to my supervisor Prof. Nigel Wilding, whose guidance and insights-made this thesis possible.

I also wish to thank my friends and colleagues who have provided both thoughtful discussion and emotional support.

Finally, thanks go to my parents Richard Wheater and Bethan Williams and my sister Rhian Wheater, who have always been ready to listen.

Contents

List of Figures

List of Abbreviations

AW Archer and Wilding

CNT Classical nucleation theory

CPU Central processing unit

DFT Density functional theory

HC2Y Hard - core 2 (double) Yukawa

HC2YF Hard - core 2 (double) Yukawa fluid

HMSA Hyper mean spherical approximation

HNC Hypernetted chain

HRT Hierarchical reference theory

IET Integral equation theory

MC Monte Carlo

MCS Monte Carlo sweep

MF Mean field

MSA Mean spherical approximation

OZ Ornstein - Zernike

PY Percus - Yevick

RPA Random phase approximation

SALR Short - ranged attractive, long - ranged repulsive

SCOZA Self - consistent Ornstein - Zernike approximation

Chapter 1

Introduction

In this thesis we use computational techniques to further our understanding of the phase behaviour of fluid systems whose constituents interact via a short range attractive, long range repulsive (SALR) potential.

This introductory chapter will first outline the phase behaviour one would expect from a simple, purely attractive, fluid, and then go on to describe the effective potential chosen, before discussing some techniques used to determine the phase behaviour.

1.1 Statistical mechanics

Statistical mechanics seeks to bridge the gap between the view of the world put forward by traditional thermodynamics, in terms of temperature, heat, entropy etc. of a system, and the state of that system at the microscopic level (atomic and molecular positions, velocities etc.) [7]. That is, the positions and momenta of all the particles that are constituent to the system, its microstate. For non-trivial cases it is extremely difficult, if not impossible, to have complete information on a system's microstate and, for systems with large numbers of particles, the number of available microstates can be enormous, even for systems with a relatively modest number of degrees of freedom per particle. Hence it is generally impractical to draw conclusions on the thermodynamic behaviour of a large system by trying to observe its microscopic behaviour. Instead we look at the macroscopic properties of

a microstate (its macrostate), e.g. its total energy.

There is the potential for any given macrostate to be represented by a large number of microstates. This many-to-one relation between microstates and macrostates is known as state degeneracy, the number of microstates which yield the same macrostate. If we assume that all physically permitted microstates are equally likely for fixed conditions, then the most likely macrostate is the one represented by the greatest number of microstates (the highest degeneracy). The more disordered a given macrostate is, the greater the number of microstates that may represent it and hence the greater its degeneracy. A macrostate with a higher degeneracy offers more routes which the system may take to reach it than a macrostate with a lower degeneracy, hence the relation between degeneracy and likelyhood.

1.2 A statistical definition of temperature

Consider two large thermal systems that can exchange energy with one another, but are thermally isolated from their surroundings. We give the two systems energies E_1 and E_2 respectively and assume that the total energy $E = E_1 + E_2$ is a constant. Each of these systems can be in a number of possible microstates corresponding to their energies. Let us assume that the first system can be in any one of $\Omega_1(E_1)$ microstates and the second system in any one of $\Omega_2(E_2)$ microstates. Thus the total number of microstates available to the combined system is the product of the number of microstates available to each system $\Omega_1(E_1)\Omega_2(E_2)$.

If the two systems are in thermal equilibrium, such that E_1 and E_2 are constant and that the combined system will favour the macrostate which maximises its total number of available microstates, we can then maximise the expression $\Omega_1(E_1)\Omega_2(E_2)$ with respect to E_1 by writing

$$\frac{d}{dE_1}\Omega_1(E_1)\Omega_2(E_2) = 0 \tag{1.1}$$

which expands to

$$\Omega_2(E_2)\frac{d\Omega_1(E_1)}{dE_1} + \Omega_1(E_1)\frac{d\Omega_2(E_2)}{dE_2}\frac{dE_2}{dE_1} = 0. \tag{1.2}$$

Since the total energy $E = E_1 + E_2$ is fixed

$$\frac{dE_2}{dE_1} = -1 \tag{1.3}$$

so equation (1.2) becomes

$$\frac{1}{\Omega_1}\frac{d\Omega_1}{E_1} - \frac{1}{\Omega_2}\frac{d\Omega_2}{dE_2} = 0 \tag{1.4}$$

and hence

$$\frac{d\ln\Omega_1}{dE_1} = \frac{d\ln\Omega_2}{E_2}. \tag{1.5}$$

Since this describes the two systems in thermal equilibrium, we can identify $\frac{d\ln\Omega}{dE}$ with the temperature T and so we have a statistical definition of temperature as

$$\frac{1}{k_B T} = \frac{d\ln\Omega}{dE} \tag{1.6}$$

which is often expressed as the inverse temperature $\beta = \frac{1}{k_B T}$ with k_B the Boltzmann constant [8].

1.3 Statistical ensembles

Since we cannot control the microscopic state of a system in an experiment, when trying to describe the state of a thermal system in terms of probability we should

consider a large (potentially infinite) number of copies of a system, each of which represents a possible state that the real system might be in. A statistical ensemble is a description of all of these copies and may be used to provide information about the state of a thermodynamic system [9]. Three commonly used statistical ensembles are the canonical (constant number N, volume V, temperature T), isobaric-isothermal (constant number N, pressure p, volume V) and grand canonical (constant chemical potential μ, volume V, temperature T) ensembles.

1.3.1 Canonical (constant NVT) ensemble

Consider a system with a fixed number of particles N, volume V and temperature T in thermal equilibrium with a large heat bath. We fix the total energy of the system E_s and heat bath E_b such that $E = E_S + E_b$ is constant. This is known as the canonical ensemble [10].

The probability $P(E_s)$ that the system has energy E_s is proportional to the number of microstates which are accessible to the heat bath mulltiplied by the number of microstates that are accessible to the system [11]

$$P(E_s) \propto \Omega(E_b - E_s). \tag{1.7}$$

Since we have an expression for temperature in terms of $\ln \Omega$ from equation (1.6), and since $E_s \ll E_b$, we can perform a Taylor expansion of $\ln \Omega(E_b - E_s)$ around $E_s = 0$ such that

$$\ln \Omega(E_b - E_s) = \ln \Omega(E_b) - \beta E_s + ... \tag{1.8}$$

where β is the inverse temperature of the heat bath. Further terms in the Taylor expansion can be neglected on account of $E_s \ll E_b$, leaving us with

$$\Omega(E_b - E_s) = \Omega(E_b)\mathrm{e}^{-\beta E_s}. \tag{1.9}$$

The probability distribution is thus

$$P(E_s) \propto \mathrm{e}^{-\beta E_s} \tag{1.10}$$

with $\mathrm{e}^{-\beta E_s}$ being known as the Boltzmann factor.

In order to quantify P_i the probability that the system is in microstate i with energy E_i the probability distribution must be normalised such that

$$P_i = \frac{\mathrm{e}^{-\beta E_i}}{\sum_r \mathrm{e}^{-\beta E_r}} \tag{1.11}$$

where the sum in the denominator over all possible micostates r serves as a normalisation constant. This normalisation constant is known as the partition function and is given the symbol Z. Thus the partition function of the canonical ensemble is

$$Z_c = \frac{1}{\sum_r \mathrm{e}^{-\beta E_r}} \tag{1.12}$$

with E_r the total energy of the system when in microstate r.

1.3.2 Isobaric-isothermal (constant NpT) ensemble

The isobaric-isothermal ensemble (as its name suggests) describes a system with a fixed number of particles N at a constant pressure p and temperature T. In addition to the internal energy fluctuating through random particle displacements (as in the canonical ensemble) the volume of the system is also permitted to change. Hence the total system energy for the isobaric-isothermal ensemble is the sum of the internal energy U and the energy cost associated with having volume V given pressure p, such that

$$E = U + pV \tag{1.13}$$

where the internal energy U is defined as the energy contained within the system (as provided by the positions and momenta etc. of the constituent particles), excluding energy due to external force fields acting upon the system. This gives us the partition function

$$Z_{ii} = \sum_i e^{\beta(U_i + pV)} \tag{1.14}$$

for the isobaric-isothermal ensemble.

1.3.3 Grand canonical (constant μVT) ensemble

The grand canonical ensemble describes a system of fixed volume in equilibrium with a large reservoir with which it is permitted to exchange both particles and thermal energy.

The total system energy in the grand canonical ensemble is the sum of the internal energy U and the energy associated with the number of particles in the system N given the chemical potential μ such that the partition function may be written as

$$Z_{gc} = \sum_i e^{\beta(U_i - \mu N)} \tag{1.15}$$

1.3.4 The partition function

The partition function provides a great deal of information about the system properties. For instance, the expected (average) value of the system energy $\langle E \rangle$ is defined as the sum of all possible values, weighted by their relative probabilities

$$\langle E \rangle = \sum_i E_i P_i \tag{1.16}$$

which (from equation 1.5) may be written as

$$\langle E \rangle = -\frac{1}{Z_c}\frac{dZ}{d\beta} = -\frac{d}{d\beta}\ln Z_c \tag{1.17}$$

which is a useful form since the partition function is usually expressed in terms of β.

It is also possible to define the Helmholtz free-energy F in terms of the partition function as

$$F = \frac{-\ln Z_c}{\beta} \tag{1.18}$$

Several thermodynamic properties can be defined in terms of partial derivatives of the Helmholtz free energy, and hence the partition function, including entropy,

$$S = -\left.\frac{\partial F}{\partial T}\right|_V = k_B \ln Z_c + k_B T \left.\frac{\partial \ln Z_c}{\partial T}\right|_V \tag{1.19}$$

heat capacity,

$$C_V = T\left.\frac{\partial S}{\partial T}\right|_V = k_B T Z_c \left.\frac{\partial \ln Z}{\partial T}\right|_V + T\left.\frac{\partial^2 \ln Z_c}{\partial T^2}\right|_V \tag{1.20}$$

and pressure,

$$p = -\left.\frac{\partial F}{\partial V}\right|_T = k_B T \left.\frac{\partial \ln Z_c}{\partial V}\right|_T \tag{1.21}$$

Additionally, we may use the definitions for energy and pressure (equations 1.17 and 1.21) to describe the enthalpy

$$H = U + pV = k_B T \left(T \left.\frac{\partial \ln Z_c}{\partial T}\right|_V + V \left.\frac{\partial \ln Z_c}{\partial V}\right|_T \right) \tag{1.22}$$

Hence, statistical mechanics - through the partition function - is able to provide definitions for the macroscopic thermodynamic properties of a system from a statistical treatment of its microscopic behaviour.

1.4 Simple fluid phase behaviour

Part of a schematic of the phase diagram of a simple, purely attractive, single-component fluid containing two phase regions is depicted in figure 1.1. The substance described by this phase diagram can exist in either the liquid or the gas phase, depending on the values of the temperature T and the chemical potential μ. The line on the phase diagram in figure 1.1 separating the liquid and gas phases is known as the 'phase boundary' and it terminates at the gas-liquid critical point. Beyond the critical point it is no longer possible to distinguish between the gas and liquid phases. For this reason the region beyond the critical point is often referred to as the 'single-phase' region.

A system in thermodynamic equilibrium under constant pressure and temperature will seeek to minimise its Gibbs free energy [12]. Consider such a system with N_1 particles of phase 1 in equilibrium with N_2 particles of phase 2. Since chemical potential μ is the Gibbs free energy per particle the total Gibbs free energy is [13]

$$G_{tot} = N_1\mu_1 + N_2\mu_2, \tag{1.23}$$

and since our system is in equilibrium

$$dG_{tot} = 0 \tag{1.24}$$

must be true. Hence

$$dG_{tot} = dN_1\mu_1 + dN_2\mu_2 = 0. \tag{1.25}$$

However, if we increase the value of N_1, the value of N_2 must decrease by the same amount in order for the total number of particles in the system to be preserved, so $dN_1 = -dN_2$. This leaves us with

$$\mu_1 = \mu_2 \tag{1.26}$$

Therefore when two coexisting phases are in equilibrium, they must have equal chemical potential. Thus we may draw a 'line of coexistence' on the phase diagram for our system between two phases where their chemical potentials are equal. Figures 1.2 and 1.3 give examples of gas-liquid binodals for a lattice and off-lattice simple fluid respectively. They show the densities of the pure gas and pure liquid phases along the line of coexistence as a line drawn in the temperature - density ($T - \rho$) plane.

When two phases are out of coexistence, the one with the lower chemical potential is favoured and so dN_1 and dN_2 are unbalanced. If we change the conditions (e.g. temperature) of a system in phase 1 such that phase 2 is now unfavoured, the system will undergo what is known as a phase transition from phase 1 to phase 2. If there is a discontinuity in the first differential of the Gibbs free energy as the temperature is increased past the point of phase coexistence then the system is said to have undergone a *first order* phase transition [14][15].

1.5 Grand canonical Monte Carlo

Monte Carlo (MC) simulations employ a stochastic process to generate a sequence of equilibrium configurations for the model system. Physical properties are then measured as configurational averages over the sequence. For example, by measuring how the average internal energy U of the model is affected by changes in the temperature T, one might determine the heat capacity $\frac{dU}{dT}$.

The precise method by which MC simulations generate the sequence of configurations varies depending on the nature of the system and the statistical ensemble chosen. MC simulations in the canonical ensemble, for instance, generate new configurations by attempting to displace particles in the system at random. For this reason, canonical MC simulations are sometimes called 'local move' MC.

In this thesis we shall focus on the use of MC simulations in the grand canonical

ensemble. In a grand canonical MC simulation the model is held at a fixed volume V, temperature T and chemical potential μ. T and μ span the phase diagram and by tuning them we are able to induce the system to undergo phase transitions between phases of interest. The internal energy U and particle number N of the model are permitted to reach thermal quilibrium with an external bath by exchanging particles with the bath. The particle exchange is simulated by attempting to insert new particles into the system at some random location or by attempting to delete a randomly selected particle from the system. A flowchart of the grand canonical MC simulation algorithm is shown in fig 1.4. A deletion or insertion is attempted with equal probability. For an insertion, a random location is chosen and the energy change ΔU associated with inserting a particle at that location is calculated. The insertion is accepted with probability $p(N \to N+1)$

$$p(N \to N+1) = \min\left(1, \frac{V}{N+1} \mathrm{e}^{-\beta(\Delta U_{N\to N+1} - \mu)}\right) \tag{1.27}$$

For a deletion, a particle is selected at random and the energy change ΔU associated with removing that particle from the system is calculated. The deletion is accepted with probability $p(N \to N-1)$

$$p(N \to N-1) = \min\left(1, \frac{N}{V} \mathrm{e}^{-\beta(\Delta U_{N\to N-1} + \mu)}\right) \tag{1.28}$$

These acceptance probabilities have been designed to maintain detailed balance, the requirement that, at thermal equilibrium, any given MC move must have the same probability as its reverse, which ensures that our system is able to reach thermodynamic equilibrium. More detailed discussions of the grand canonical MC algorithm (including the differences between lattice and off-lattice models) and detailed balance are to be found in the relevant sections of chapter 3.

There is no need to have explicit particle displacement moves in grand canonical MC since these are realised implicitly through repeated deletions and insertions. This focuses the computational effort on the fluctuations in the number density, which is the most important variable for the system's evolution through phase space near the gas - liquid phase transition. In addition, when the pairwise interactions are truncated (as is standard practice in MC simulations) the value of ΔU, used to

calculate the acceptance probability, becomes dependent only on local interactions. These factors combine to make grand canonical MC simulations an efficient means of obtaining data on equilibrium phase behaviour.

1.5.1 Observing phase coexistence with grand canonical Monte Carlo

The most useful observables of a computer simulation are those which are directly affected by the simulation technique chosen, as they are the variables which give us the most direct information about the system state. In statistical mechanics these variables are called 'order parameters' and in the case of grand canonical MC the order parameters are the particle number density ρ and the internal energy U. In particular, the fluctuations of the density ρ, provide a great deal of information about the nature of phase coexistence. In the simulation we can compute $p(\rho)$, the probability density function of ρ as a histogram averaged over a large number of configurations. Fig 1.5 shows a sketch of the form of such a distribution close to gas - liquid coexistence. The most important (and most notable) feature of this distribution is its double - peaked shape. Each peak corresponds to one of the pure phases. The low density peak corresponds to the gas phase and the high density peak to the liquid phase. For values of μ and T on the line of gas-liquid phase coexistence, the weights of the two peaks (the integrated area beneath them) are equal. If we wish to locate a point of gas - liquid coexistence, then we must tune μ and T until $p(\rho)$ has a double - peak and the weights of the two peaks are equal. However, in order to obtain accurate measures of the weights of the two peaks we may need many independent samples of configurations from each of the two phases. Hence we must run our simulation for enough time for us to obtain good statistics on each peak. This requirement can become problematic when the energy calculations become computationally intensive, or when the free - energy barrier to transition between states is large, such that it may take a long time to obtain a large enough statistical sample.

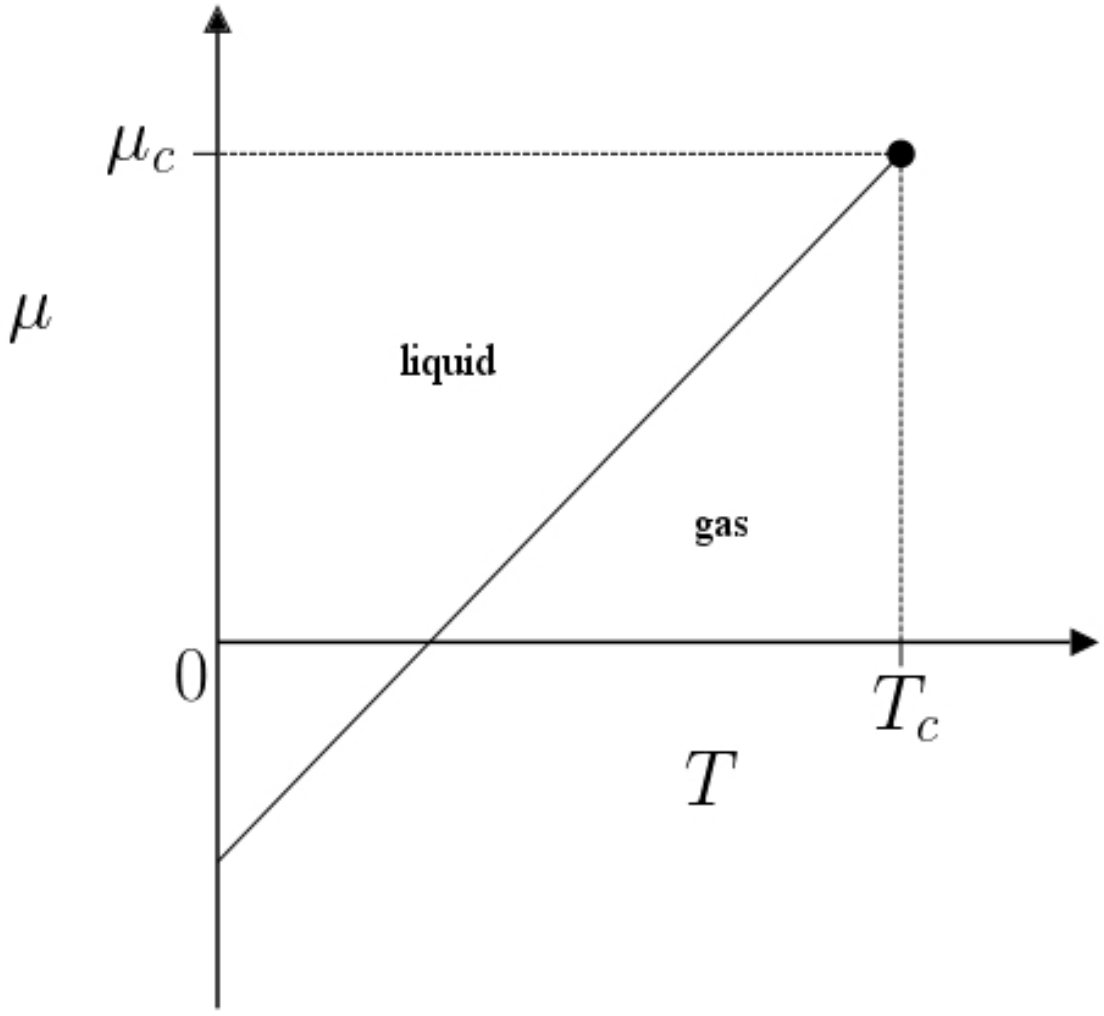

Figure 1.1: Sketch of a typical phase diagram for a simple, purely attractive, fluid in the (T, μ) plane. The solid line represents a line of first order phase transitions separating a gas and liquid phase. The line terminates at a critical point (T_c, μ_c), denoted by a black circle.

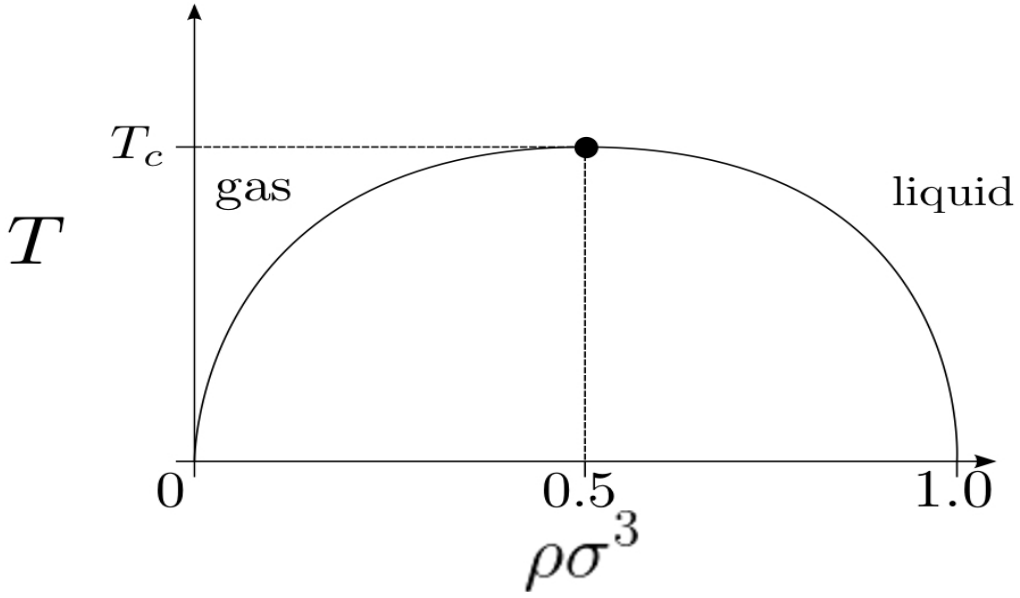

Figure 1.2: Schematic of a gas - liquid binodal, showing the densities ρ of the two coexisting phases as a function of temperature T for an Ising lattice gas model. For the lattice model, the critical density $\rho_c = 0.5$.

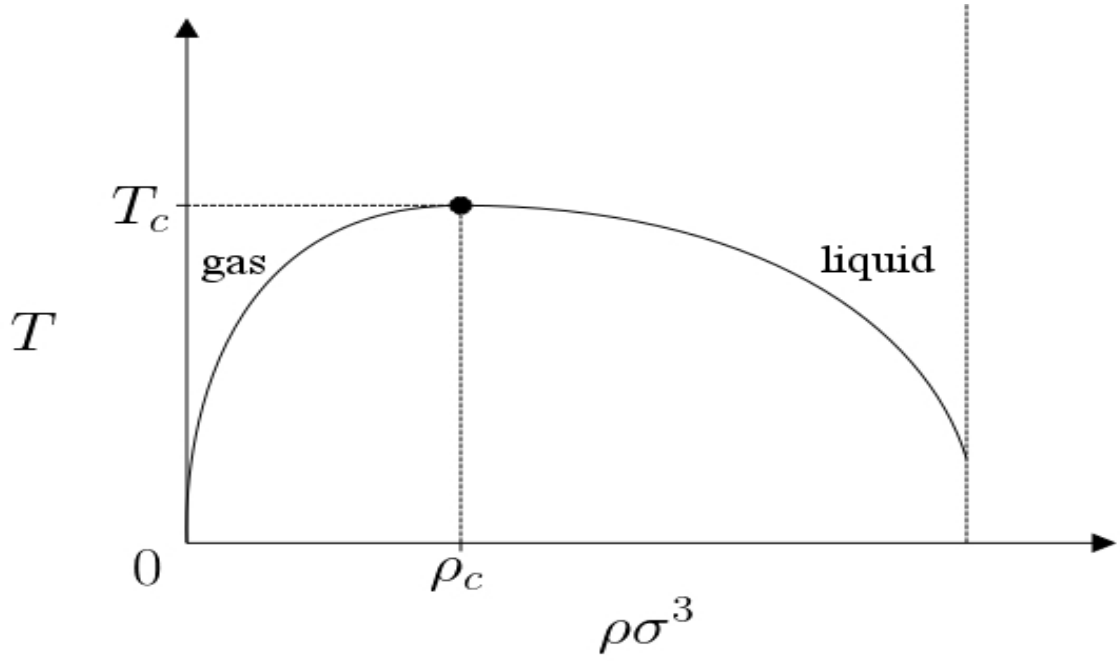

Figure 1.3: Schematic of a gas - liquid binodal, showing the densities ρ of the two coexisting phases as a function of temperature T for an off - lattice fluid.

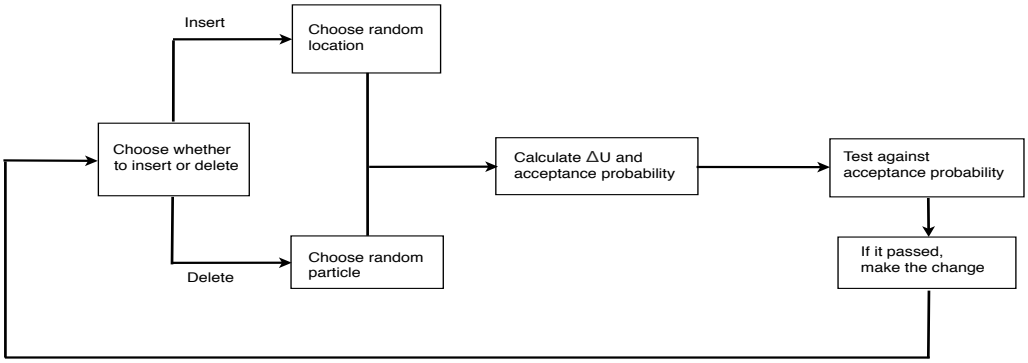

Figure 1.4: A flow chart to illustrate the grand canonical Monte Carlo simulation algorithm. We begin by choosing to do either an insertion or a deletion, with equal probability. If we are making an insertion, then a random location is chosen within the system for the insertion. If we are making a deletion, then a random particle is chosen from those present in the system. We then calculate the change in internal energy ΔU associated with the proposed change by summing the interactions of all other particles with the particle we are proposing to insert or delete, out to the truncation length of the pair potential. This then tells us the acceptance probability of the move as per equations (1.27) and (1.28). We decide whether to accept or reject the move by testing the acceptance probability against a pseudo random number generator. If the move is accepted, we make the change. Once the move has been either accepted or rejected we record the new state of the system and generate another random move.

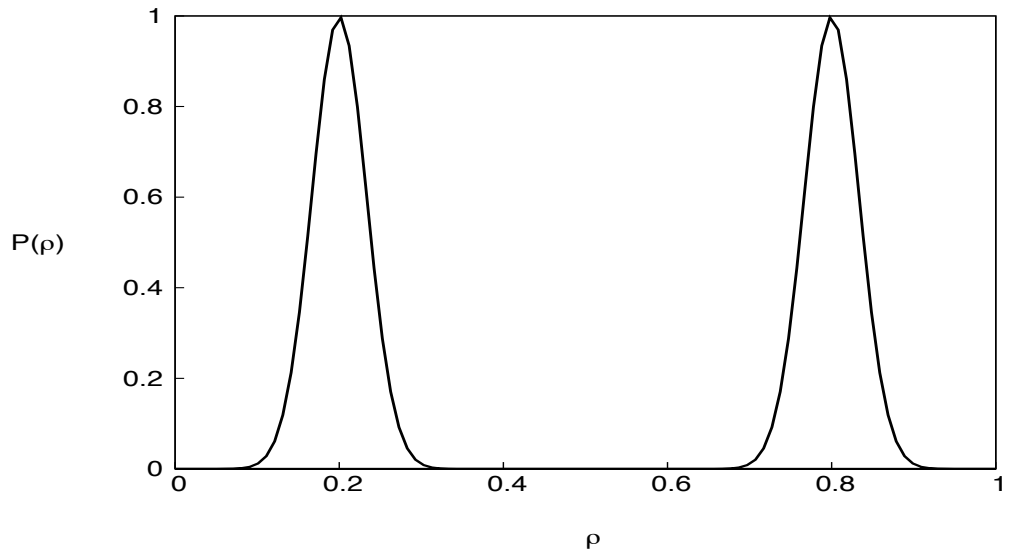

Figure 1.5: A schematic of a distribution of densities sampled $P(\rho)$ by a grand canonical Monte Carlo simulation of an Ising lattice gas. The distribution shows two peaks, showing the densities at which the gas and liquid phases may be found. One can determine that the two phases are in thermodynamic coexistence by the fact that the two peaks in the distribution have equal weight.

1.6 Examples of short-ranged attractive, long-ranged repulsive potentials

The simplest example of a short-ranged attractive, long-ranged repulsive (SALR) effective potential would be a double square-well potential:

$$\beta v(r) = \begin{cases} \infty & r < \sigma \\ -\epsilon & \sigma \leq r < z_1\sigma \\ A & z_1\sigma \leq r < z_2\sigma \\ 0 & r \geq z_2\sigma \end{cases} \tag{1.29}$$

with $\beta = \frac{1}{k_B T}$ is the inverse temperature, σ is the particle diameter, ϵ is the strength of the attraction, A is the strength of the repulsion and z_1 and z_2 are the attractive and repulsive lengthscales respectively. An example of such a double square well potential is shown in figure 1.6 for $\epsilon = 2.7$, $A = 2.0$, $z_1 = 2$ and $z_2 = 4$.

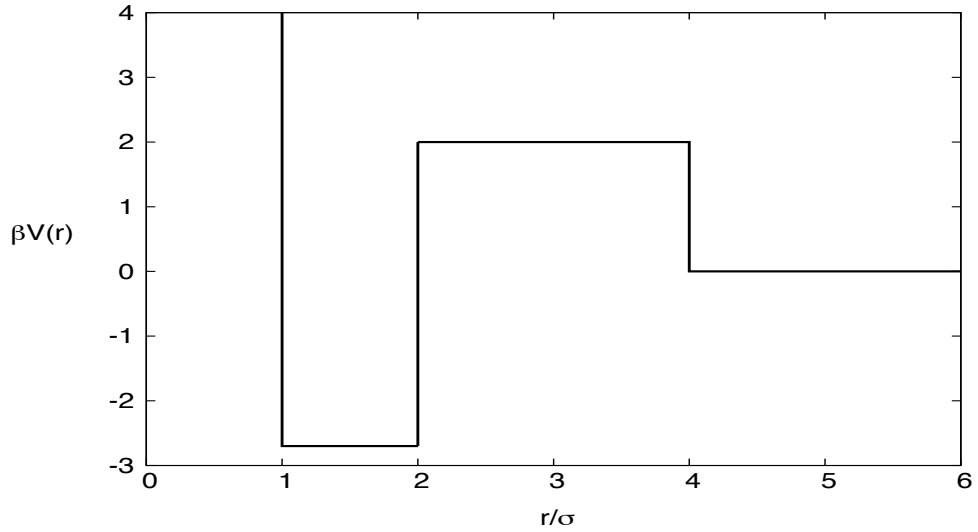

Figure 1.6: An example of a double square well potential for $\epsilon = 2.7$, $A = 2.0$, $z_1 = 2$ and $z_2 = 4$.

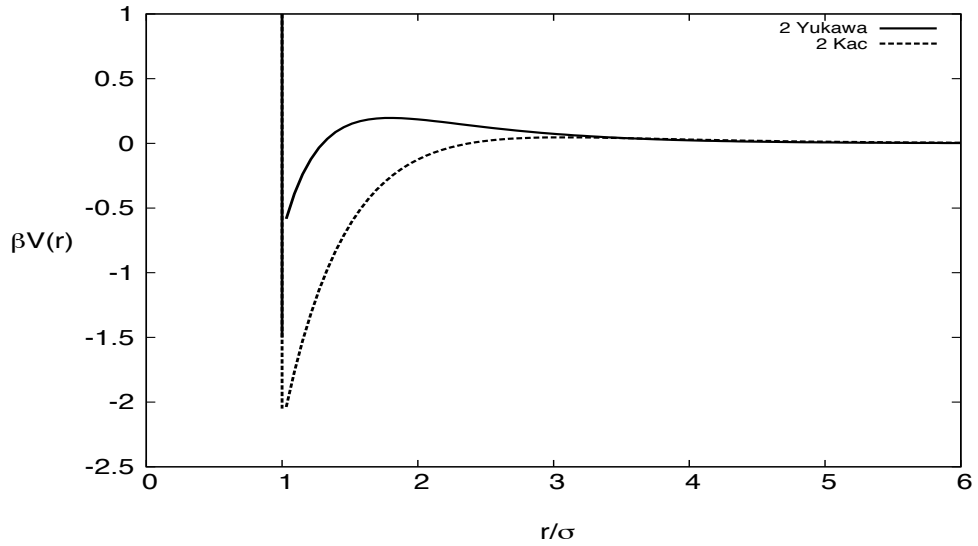

Figure 1.7: Example 2-Yukawa (solid line) and 2-Kac (broken line) potentials. The parameters are $\epsilon = 2.7$, $A = 1.0$, $z_1 = 2$ and $z_2 = 1$ in both cases.

While the double square-well potential is easy to describe, the truncation of the potential for $r > z_2\sigma$ can cause an error in our energy calculations [16]. While truncation of potentials beyond a certain cutoff range r_c is common practice in Monte Carlo simulations, it seems best to choose a potential which tends towards zero as $r \to r_c$ so as to minimise the introduced error. Two examples of such potentials are the double Yukawa and double Kac potentials. The double Yukawa potential has the form

$$\beta v(r) = \begin{cases} \infty & r < \sigma \\ -\frac{\epsilon\sigma}{r} e^{-z_1((\frac{r}{\sigma})-1)} & \\ +\frac{A\sigma}{r} e^{-z_2((\frac{r}{\sigma})-1)} & r \geq \sigma \end{cases}, \tag{1.30}$$

while the double Kac potential has the form

$$\beta v(r) = \begin{cases} \infty & r < \sigma \\ -\epsilon z_1^3 e^{-z_1 \frac{r}{\sigma}} & \\ +A z_2^3 e^{-z_2 \frac{r}{\sigma}} & r \geq \sigma \end{cases}. \tag{1.31}$$

Examples of both of these potentials are shown in figure 1.7 with $\epsilon = 2.7$, $A = 1.0$, $z_1 = 2$ and $z_2 = 1$ in both cases. For both the Yukawa and Kac potentials the first exponential term, amplitude ϵ and lengthscale z_1, controls the short ranged attraction and the second exponential, amplitude A and lengthscale z_2, controls the long ranged repulsion. As can be seen from figure 1.7 both potentials can be tuned such that they tend towards zero as $r \to r_c$. In this thesis we chose to focus on the double-Yukawa interaction potential.

1.7 Integral Equation Theory

The intention of an integral equation theory (IET) is to determine - by analytical or numerical means - the radial distribution function $g(r)$ and the structure factor, $S(k)$ (related to the Fourier transform of the distribution function) which contain structural information about a thermodynamic system and to use that information to make predictions as to the equilibrium thermodynamic properties of the system.

1.7.1 The Radial Distribution Function

The radial distribution function $g(r)$ measures the probability a particle can be found at distance r, given that there is a particle at the origin. That is, the probability that a pair of particles separated by a distance r can be found somewhere in the system.

As $r \to \infty$, $g(r) \to 1$ and the likelyhood of there being a correlation between any two particle locations approaches zero (the limit of vanishing correlations). Thus we define the pair correlation function $h(r) = g(r) - 1$ such that $h(r) \to 0$ in the limit of $r \to \infty$.

We can formally define a new function $c(r)$ through the Ornstein-Zernike equation [17]

$$h(r) = c(r) + \int d^3r' c(r')\rho h(|\underline{r} - \underline{r}'|) \tag{1.32}$$

An equation which links $h(r)$ and $c(r)$ to the interparticle potential can be obtained from the cluster expansion of $g(r)$ [18, 19]

$$g(r) = \mathrm{e}^{-\beta v(r)+h(r)-c(r)+E(r)} \tag{1.33}$$

with $v(r)$ the interparticle potential and $E(r)$ a function known as the 'bridge' function.

1.7.2 The Hypernetted Chain Approximation

The hypernetted chain (HNC) approximation assumes that the bridge function $E(r) = 0$. This approximation allows equations (1.32) and (1.33) to form a set of closed equations in $g(r)$ and $c(r)$ [20, 21, 22, 23, 24]. These equations are then numerically soluble via an iterative procedure.

Under the HNC approximation equation (1.33) becomes

$$g(r) = e^{-\beta v(r)+h(r)-c(r)} \tag{1.34}$$

introducing the function

$$\theta(r) = h(r) - c(r) \tag{1.35}$$

allows us to express equation (1.34) as

$$c(r) = e^{-\beta v(r)+\theta(r)} - \theta(r) - 1 \tag{1.36}$$

Taking the Fourier transform of equation (1.32) gives

$$h(k) = c(k) + \rho h(k)c(k). \tag{1.37}$$

Combining equations (1.35) and (1.37) and factoring out the terms in $h(k)$ yields

$$\theta(k) = \frac{\rho c^2(k)}{1 - \rho c(k)} \tag{1.38}$$

To begin, we substitute an initial estimate for $\theta(r)$ - described as a set of values over the range of r for which we wish the direct correlation function to be defined - into equation (1.36) to obtain an estimate for $c(r)$. Taking the Fourier transform gives us $c(k)$, which we may substitute into equation (1.38) to provide an estimate for $\theta(k)$. Another Fourier transform yields a new estimate for $\theta(r)$ and the process may be repeated. Generally, this iterative process is repeated until the difference bewteen two successive estimates for $c(r)$ is less than some prescribed level of precision.

Unfortunately such series expansions have a tendency to converge badly at high densitites. One method of overcoming this difficulty is to take a partial sum of particular terms appearing in the series expansion [25][26][27][28]

Once one has a final estimate for the direct correlation function, one may calculate the compressibility

$$\chi_{fluc} = \left(1 - \rho \int_0^\infty c(r) 4\pi r^2 dr\right)^{-1} \tag{1.39}$$

Where the subscript on the χ indicates that the compressibility was calculated via the structure fluctuation route. Since the compressibility diverges in the vicinity of phase coexistence, one may use equation (1.39) to map out the gas-liquid binodal in the ρ, T plane (see figure 1.3).

One advantage of IETs over MC simulations is the smaller timeframe needed to perform the iterative process compared with the computational time needed for a MC simulation to gather enough data to accurately determine the free-energy of phase coexistence. Also IETs can be used to describe larger systems than MC simulations, whose results are vulnerable to bias from finite size effects as a result.

The main drawback of using IETs is that many of them make use of approximations that produce inaccurate results (such as the HNC) while the more refined theories (e.g. modified HNC and reference HNC) suffer from a lack of thermodynamic self-consistency [29].

1.7.3 Thermodynamic Self-Consistency

A theory is thermodynamically self-consistent if it returns the same result when a thermodynamic variable is calculated via two different 'routes' [30][31].

For example, we saw in equation (1.39) that the compressibility may be calculated from the direct correlation function (χ_{fluc}) but we can also calculate it from the virial equation

$$\chi_{vir} = k_B T \frac{\partial \rho}{\partial p}_T \tag{1.40}$$

with p the osmotic pressure and ρ the system density [32]. Hence, one condition for thermodynamic self-consistency should be [33]

$$\left(1 - \rho \int c(r) dr\right)^{-1} = k_B T \frac{\partial p}{\partial \rho}_T \tag{1.41}$$

If a theory does not obey thermodynamic self-consistency then it can produce unreliable results, since the same theory can yield two different values for the same thermodynamic variable, depending on which route was used to obtain it. This causes difficulties when trying to make predictions of phase behaviour.

Chapter 2

Background and Literature Review

2.1 Physical Systems with Competing Interactions

For some time it was believed that the phase behaviour of a single component fluid interacting via an isotropic pair potential was limited to a gas, liquid and solid phase only, as is apparently the case for simple models such as the Lennard - Jones fluid. However, recent studies have shown that systems exist which exhibit a greater variety in their phase behaviour.

Many unrelated two- and three-dimensional systems exhibit heterogeneous domain patterns, such as stripes, islands and circular droplets in two dimensions [34, 35] or sheets, cylinders and spherical droplets in three dimensions, at different length-scales ranging from the nanoscale to the macroscopic [1, 36, 37, 38, 39, 40, 41, 42] (figure 2.1). Such patterns may arise from the formation of heterogenous structures, which are stabilised by competing interactions [43, 44, 45, 46, 47]. For example, in two dimensions, systems as apparently dissimilar as magnetic garnets and Langmuir monolayers both form periodic structures consisting of domains with circular or striped shapes. In the garnets, the magnetisation normal to the plane is high inside these domains and low between them whereas, in the Langmuir films, the number density of molecules inside the circles and stripes is higher than outside. Clearly the mechanism for the formation of the domains in these two systems is

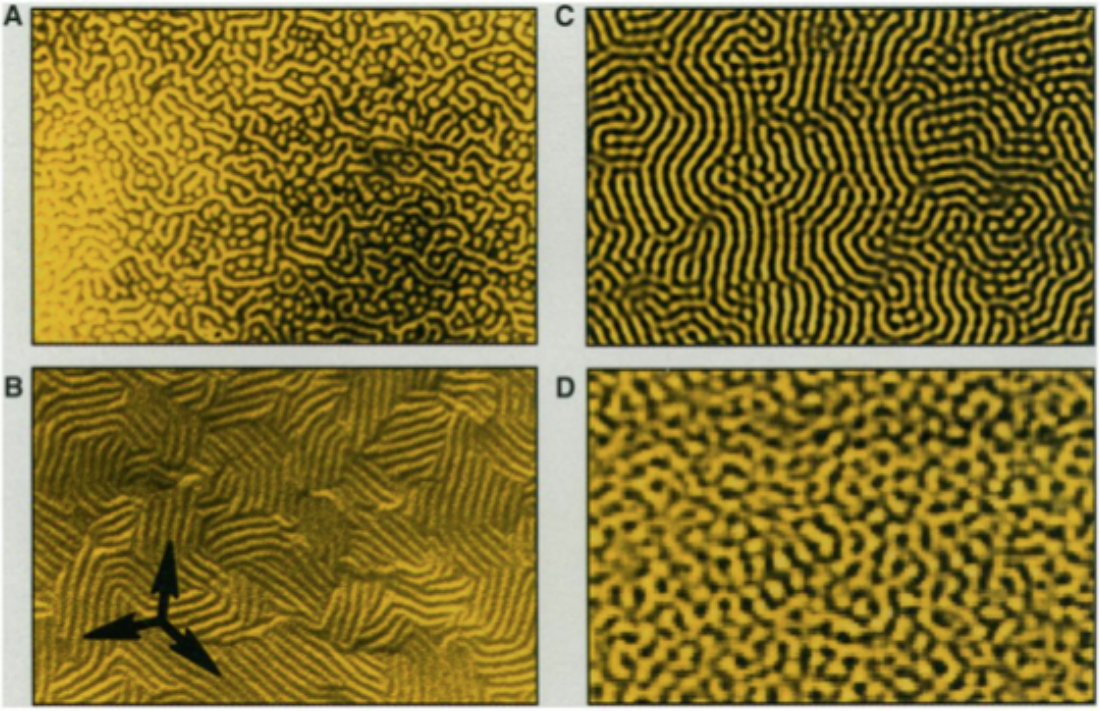

Figure 2.1: Sampling of stripe domain patterns in physical and chemical systems. (A) Alternating superconducting and normal regions in a foil lead of a type I superconductor, in its intermediate state. The pattern was induced by a normal magnetic field and rendered visible by a powder decoration technique; period $7\mu m$. (B) P_β, ("ripple") phase in a vesicle composed of the phospholipid DMPC and DMPE (95:5 molar ratio), rendered visible after rapid freezing by freeze-fracture electron microscopy; period, 240Å. (C) Stationary ("Turing") patterns in a chemical reaction-diffusion system, rendered visible by preferential absorption of light; period, 0.25 mm. (D) Snapshot of fluctuations preceding the appearence of a convective roll pattern in CO2 gas undergoing a Rayleigh-Benard instability, rendered visible by a shadowgraph technique; period, $1cm$. Figure by Seul and Andelman [1].

different, but the effective behaviour is the same [48, 49, 50].

Other examples of physical systems that exhibit heterogeneous structures include the aggregation of atomic monolayers on metallic surfaces and the modulation of surface charge transfer in certain metallic interfaces [51], the spatial dsitribution of normal and superconducting domains in a type I superconducting film in its intermediate state [1] and the clustering and gelation of globular protein solutions, star polymer - linear polymer mixtures and a variety of colloidal systems in different solvents [43, 50, 52, 53, 54, 55, 56]. Surfactant molecules have also displayed a propensity for clustering in similar patterns [57, 58, 59, 60, 61, 62, 63, 64, 65]

In this thesis we shall focus our attention upon the self-assembly of heterogeneous structures by colloids with competing short-ranged attractive and long-ranged repulsive effective potentials (e.g. an attractive depletion force from non-adsorbing polymers and an electrostatic repulsion between like charged particles) [66, 5, 67, 53, 54]. Competing attractive and repulsive effective potentials are also appropriate for describing the effective interactions between solute particles in a subcritical liquid [68], and colloidal monlayers [69, 2] where the short range attraction arises from the van der Waals and capillary forces, while the longer range repulsion is thought to be due to dipole-dipole interactions.

Colloidal suspensions have widespread popularity in a variety of commercial applications. An important factor contributing to this popularity is that their macroscopic properties can be carfully tailored during synthesis by controlling their chemical composition, size and the solvent in which they are suspended. The ability to design a colloidal fluid which forms specific structures has potential applications in display technologies, drug delivery and gene therapy [50, 52, 70, 71]. It is important for all of these appplications that the conditions under which given structures are thermodynamically stable are well understood. As such, a considerable amount of effort has been expended on trying to further our understanding of the behaviour of colloidal systems with competing interactions in the form of Integral Equation Theory (IET) [72, 73, 74, 75, 3, 4, 50] and simulational studies [5, 76, 34, 35, 77], as well as experiments [67, 53, 54, 1, 48].

2.2 Integral Equation Theory Studies

Studies of the behaviour of a hard-core two Yukawa fluid (HC2YF) using a density functional theory (DFT) based on the self-consistent Ornstein Zernike approximation (SCOZA) have determined that the height of the free energy barrier to nucleation of a droplet of the liquid phase in the bulk gas phase is signficantly reduced by the presence of even a very weak long ranged repulsion [78, 79, 80], thereby increasing the droplet nucleation rate. Introducing a long ranged repulsion to the fluid also has the effect of reducing the critical temperature and flattening the gas-liquid binodal [81, 73], as well as greatly enhancing the long range interparticle correlations and the region of high compressibility in the vicinity of the critical point [43, 82]. This

behaviour indicates that the high compressibility is the result of density fluctuations caused by the appearence of clusters of strongly correlated particles.

The structure factor $S(q)$ of a fluid is related to the Fourier transform of its radial distribution function by [28]

$$S(q) = 1 + \rho \int e^{i\underline{q}.\underline{r}}(g(r) - 1)dr, \tag{2.1}$$

and hence gives us information about its long range correlations [82]. A slowly decaying potential (slower than r^{-2}) will make its greatest contribution to the structure factor at $q = 0$ (i.e. infinite lengthscale) since the volume of a spherical shell with fixed width increases with r^2. Hence, when Sear and Gelbart [2] investigated the structure factor of a colloidal system with a 2-Kac potential they found that, for zero repulsion, there was a peak at $S(q = 0)$ in the vicinity of the critical point (figure 2.2). As the inverse temperature is increased, the peak grows. Eventually the peak at $S(q = 0)$ diverges along with the isothermal bulk compressibility $\chi = \frac{S(0)}{\rho kT}$. Within a mean field (MF) theory, such as the one Sear and Gelbart used, the locus of points where χ diverges is called a spinodal and represents the limit of stability of a phase in the system. However, when a repulsive term was added to the potential with amplitude comparable to that of the attraction, with a longer range, the peak in $S(q)$ was shifted to low $q > 0$ (figure 2.3). Since the repulsive term has the longer range, its effect on $S(q)$ (relative to the attractive term) is strongest at $q = 0$, where it dominates the attractive term. As the wavevector q increases, the contribution to the structure factor from the repulsion decays according to the inverse lengthscale z_2, while that of the attraction decays according to the larger inverse lengthscale z_1. Eventually at sufficiently large q the attractive term dominates the repulsive term, and so a peak apears in $S(q)$ at low q. So, while the repulsive term seeks to suppress long-ranged correlations (and hence, compressibility), the attractive term encourages correlations at a shorter wavelength and the fluid separates into domains with different densities.

Groenewold and Kegel [83, 84] constructed a theoretical model in which like charged colloids were suspended in a non-polar solvent. The like charges of the colloids caused a screened Coulmbic repulsion between the colloids, while a depletion interaction between the colloids and solvent caused the colloids to feel a short-

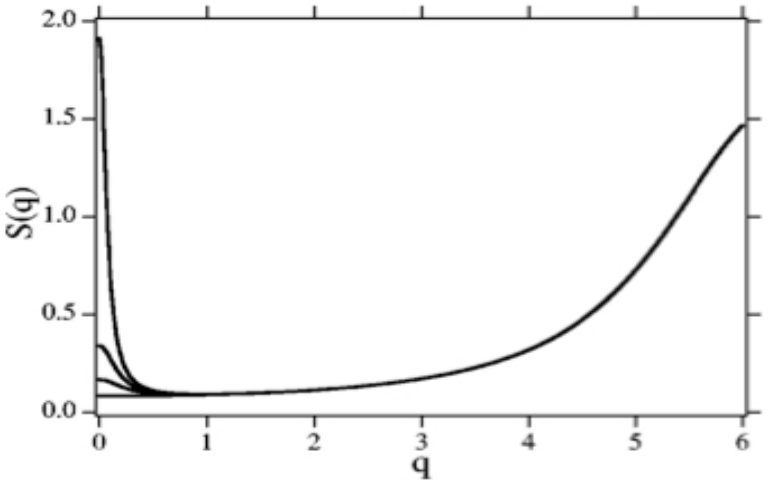

Figure 2.2: The structure factor $S(q)$ from reference [2], plotted for a potential with a purely attractive long-range interaction. The range of the attraction $z_1 = 2$. The system density $\rho = 0.6$. The four curves overlap except near the peak, and correspond, from bottom to top, to attractive strength $\epsilon = 0$ (hard spheres), 0.4, 0.6 and 0.76.

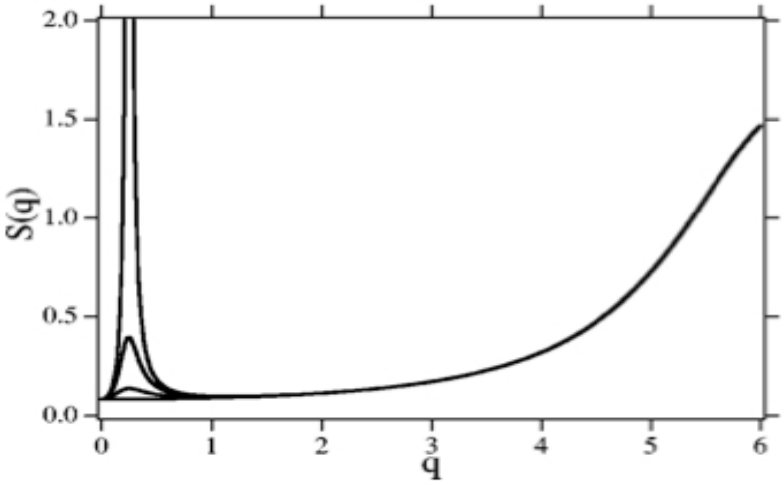

Figure 2.3: The structure factor $S(q)$ from reference [2], plotted for a potential with competing short range attractive and long ranged repulsive interactions at four different temperatures. The lengthscales for the attraction and repulsion are $z_1 = 2$ and $z_2 = 4$ respectively and the ratio between the amplitudes of the attractive and repulsive terms is 1. The system density $\rho = 0.6$. The four curves overlap except near the peak; the curves correspond, from bottom to top, to attractive strength $\epsilon = 0$ (hard spheres), 0.8, 1.6 and 2.0. The peak of the curve at $\epsilon = 2$ has a maximum (not shown) of 6.13; at $\epsilon = 2.03$ the peak diverges.

ranged attraction to one another. By calculating analytically the free energy per particle for a variety of cluster geometries, Groenewold and Kegel demonstrated that symmetrical, spherical clusters are energetically less favourable than clusters with asymmetric geometries such as circular disks or cylinders. This phenomenon was due to the greater repulsive energy induced per colloid in the spherical as opposed to the asymmetric clusters.

In 2008 Archer, Inoescu, Pini and Reatto applied a DFT to a colloidal system with a SALR effective potential [3]. The theory was set up to allow density variation in one dimension. By observing the profile of the local density in the system, they were able to discern two types of thermodynamic phases; one with uniform fluid density (gas or liquid), the other with density modulations of a regular lengthscale. The density profile of the modulated phase showed alternating regions of high and low density (figure 2.4), indicating the existence of a λ-transition. The λ-line is is a line of continuous transitions from a uniform phase to a modulated phase with some specific periodicity of modulations. This is charactersed by the correlation functions becomeing purely oscillatory with a given wavelength, which is the cause of the divergence of the low-q peak in $S(q)$ seen by Sear and Gelbart [3][85].

The authors predicted that if density fluctuations were permitted to occur in 3 dimensions, then other modulated phases would become visible, and indeed Ciach in similar studies with density fluctuations in 3 dimensions obtained results for systems with a variety of modulated phases [50, 4]. Ciach predicted that colloids would aggregate to form spherical clusters and that in a system containing a large number of such clusters, they would form a bcc lattice as the most thermodynamically stable structure. Ciach also saw that as clusters grew they became elongated (as predicted by Groenewold and Kegel) becoming cylinders which arrange themselves into hexagonal lattices. For $\rho < \rho_c$ (i.e. system densities less than the critical density) the density modulations consisted of clusters (regions of relatively high density) whereas for $\rho > \rho_c$ the modulations consisted of voids (regions of relatively low density). Both Ciach and Archer *et al.* saw remarkably similar phase diagrams for systems with different effective interaction parameters, indicating the relative stability of the modulated phases. In fact, the greatest impact of the effective potential parameters appears to be the lengthscale of the density modulations (figures 2.5 and 2.6).

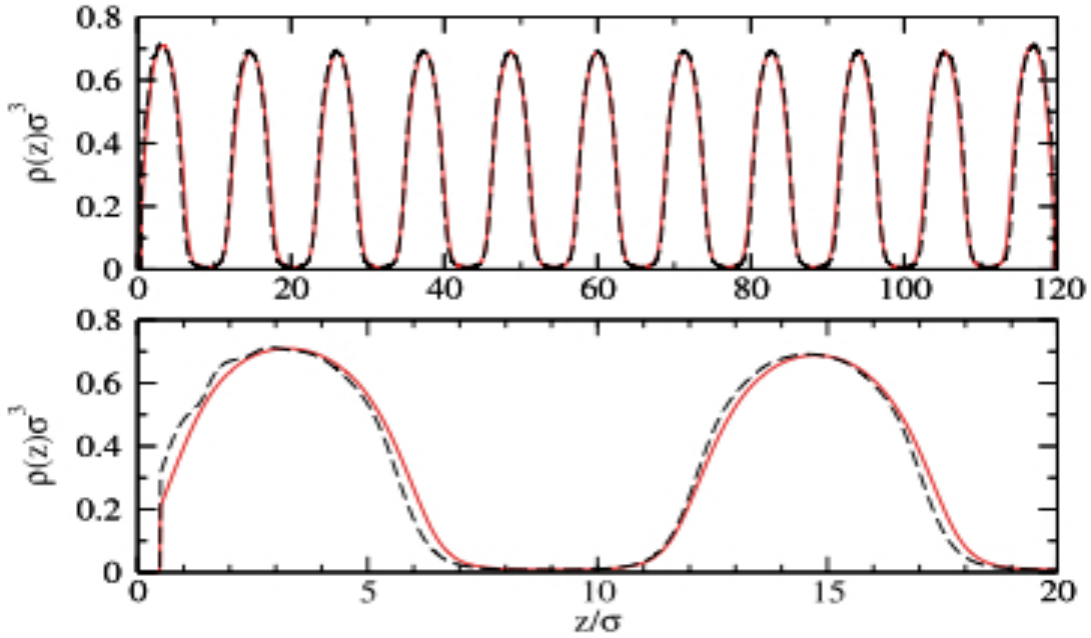

Figure 2.4: Density profiles from reference [3]. In the upper pane is displayed the density profile for the fluid in the case with inverse attractive strength $\epsilon^{-1} = 0.65$, repulsive strength $A = 0.5$, attractive and repulsive lengthscales $z_1 = 1$ and $z_2 = 0.5$ respectively and average fluid density $\overline{\rho} = 0.25$. In the lower pane, a magnification of the left-hand portion of the density profile is displayed.

2.2.1 Limitations of Theoretical Studies

In spite of the SCOZA's accuracy at predicting fluidic behaviour [86], it is unable to describe the formation of inhomogeneous phases because it's core condition is violated in the vicinity of the λ-line. The core condition of the SCOZA requires that [66]

$$\begin{cases} g(r) = 0 & r \leq \sigma \\ c(r) = K(\rho_b, \beta)v(r) & r > \sigma \end{cases} \tag{2.2}$$

in order for its solutions to be analytic. Here $g(r)$ is the radial distribution function and the condition $g(r) = 0$ for $r \leq \sigma$ is satisfied by the presence of the hard-core term in the interaction potential, $c(r)$ is the density correlation function with amplitude K determined by a function of the bulk density ρ_b and inverse temperature β. $v(r)$ comes from the interaction potential $\beta v(r)$.

In the vicinity of the λ - line, where the peak in $S(q > 0)$ diverges, the Fourier

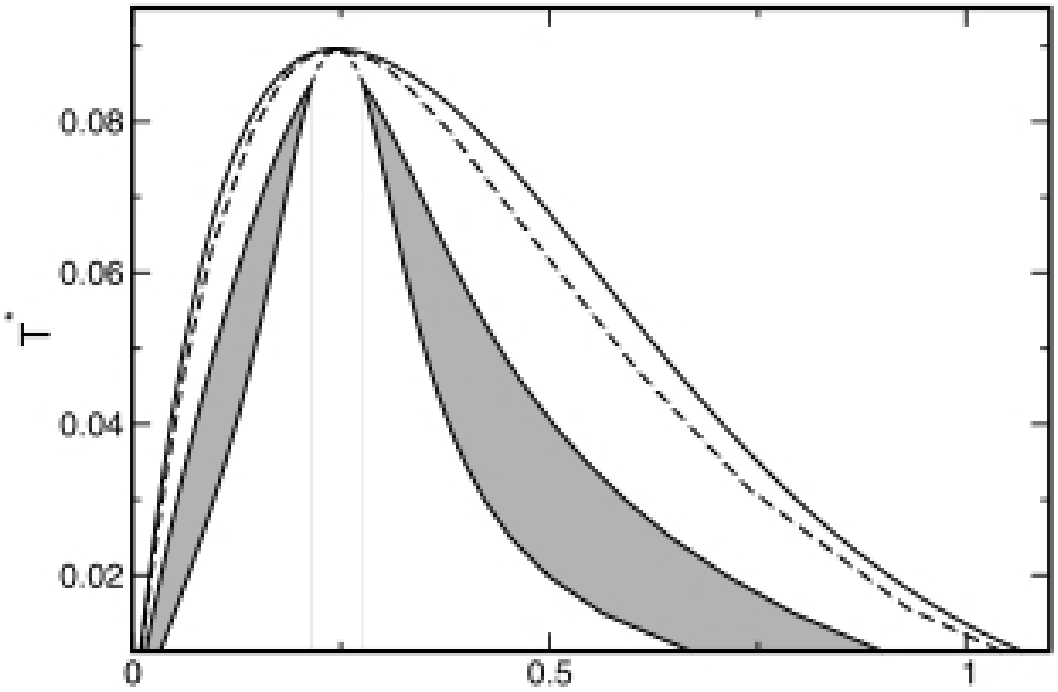

Figure 2.5: Phase diagram obtained by Ciach [4] with a MF (mean field) approximation for attractive $\epsilon = 1$ and repulsive $A = 0.2$ strengths, and respective lengthscales $z_1 = 1$ and $z_2 = 0.5$. The outer solid lines are the coexistence lines between the uniform fluid and bcc phase, the bcc and hexagonal phases coexist along the dashed lines, along the dotted lines the hexagonal and lamellar phases coexist, and inside the shaded regions the gyroid phase is stable.

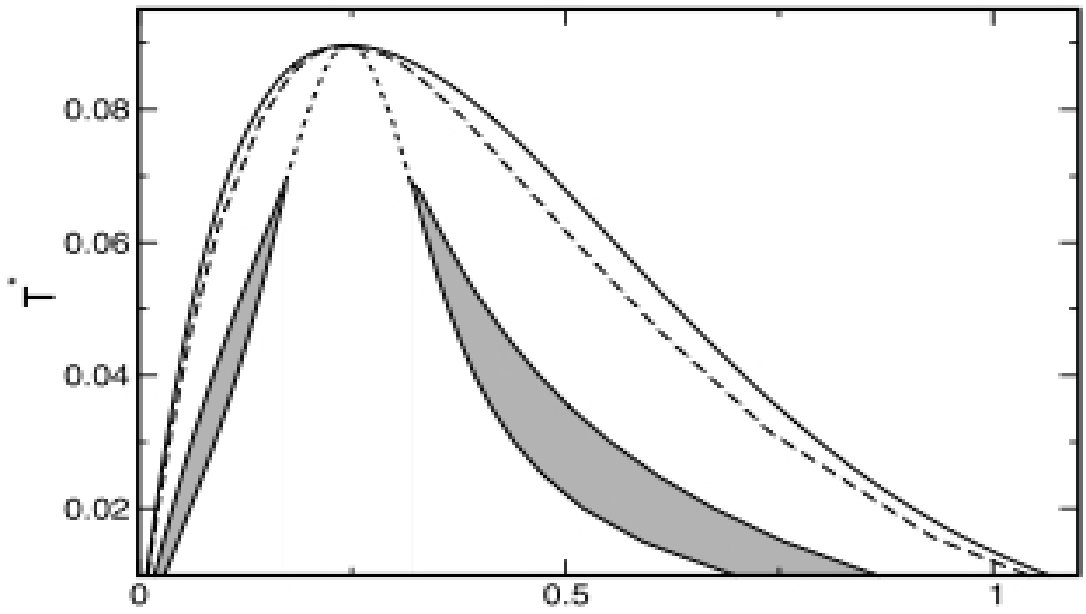

Figure 2.6: Phase diagram obtained by Ciach [4] in the MF (mean field) approximation for attractive $\epsilon = 1$ and repulsive $A = 0.05$ strengths, and respective length-scales $z_1 = 3$ and $z_2 = 0.5$. The outer solid lines are the coexistence lines between the disordered and the bcc crystal phases, the bcc and hexagonal phases coexist along the dashed lines, along the dotted lines the hexagonal and lamellar phases coexist, and inside the shaded region the gyroid phase is stable.

transform $\hat{c}(q)$ of the density correlation function also diverges and, since

$$c(r) = \int_{-\infty}^{\infty} \hat{c}(q) e^{2\pi i r q} dq \qquad r \in R \tag{2.3}$$

the density correlation function $c(r)$ becomes undefined. Thus the core condition is no longer satisfied and the SCOZA cannot produce analytic results.

DFTs suffer similarly in the vicinity of the λ-line. Archer *et al.* [66, 5], making use of random phase approximation (RPA), hypernetted chain (HNC) and mean spherical approximation (MSA) DFTs applied to a system with a HC2Y pair potential, found that all 3 suffered from regions of no solution in the vicinity of the λ-line, as has been known to happen with such theories [87][88][89][90]. Attempts were made to obtain a solution for the vapour-cluster transition with the Percus-Yevick (PY) approximation, but were unsuccessful due to a lack of thermodynamic self-consistency in the theory.

While DFTs take short-ranged structure into account quite precisely, the problem with their application to systems with inhomogeneous structure stems from their use of MF approximations to deal with long-ranged fluctuations, since MF theory assumes that long-ranged structure is uniform [91], and while the use of hierarchical reference theories (HRTs) and coarse graining procedures has improved this situation somewhat [92, 93, 94, 95], they are limited in their use to the vicinity of the critical point.

2.3 Monte Carlo Simulation

Equilibrium Monte Carlo (MC) simulations of SALR fluids have been demonstrated to exhibit transitions to cluster fluids [96][97] and have been used in comparison to theoretical models to gauge their predictions.

Bomont et al. drew conclusions as to the relative accuracy of a number of IETs when comparing data obtained from MC sumulations in the canonical, constant NVT, ensemble (also known as 'local move' MC) with those provided by the HNC, HMSA (Hybrid Mean Spherical Approximation), HRT and SCOZA theories, finding

reasonable agreement in their predictions for internal energy U and excess chemical potential μ^{ex} [30]. Similar studies have shown good agreement between IETs and MC in the onset of the cluster peak in the structure factor [98, 96].

There are several benefits to using MC simulations to study fluids with competing interactions. Unlike some of the theoretical techniques listed, MC simulations do not suffer from regions of no-solution, are not limited in their use to the vicinity of the critical point, are always thermodynamically self-consistent and deal with both short- and long-ranged interactions explicitly [91, 99, 100].

While the simulational studies previously mentioned focus on local move MC, less attention has been paid to MC in the grand canonical (constant μVT) ensemble. By allowing the internal energy U and particle number N to fluctuate via particle insertions and deletions, grand canonical MC can provide a highly efficient route to fluid equilibrium (see section 1.5).

Direct particle simulations of the HC2Y fluid have revealed the structure of non-homogeneous micro-phases, demonstrating the existence of spherical clusters, cylindrical networks, lamellae and spherical voids at particle-level detail. Such detailed structure information would have been very difficult to achieve via experimental or theoretical means [101, 102, 97].

In 2007 Archer and Wilding, while modelling a HC2YF with MC simulations in the grand canonical ensemble, found that as the attractive strength increases, kinks (discontinuities) start to appear in the mean system density as a function of chemical potential $\overline{\rho}(\mu)$, see figure 2.7. Inspection of the system density distributions in the vicinity of those kinks revealed a double-peaked structure (figure 2.8) with one peak corresponding to a homogneous gas and the other corresponding to a custered phase. Archer and Wilding were able to trace out the shape of the system phase diagram by drawing the locus of these double-peaked distributions in figure 2.9.

Despite the benefits of utilising MC simulations and it's ability to provide data which is complementary to experimental and theoretical results, running simulations of systems with competing interactions is computationally expensive. This is due to the long range of interactions ($\sim 10-20$ times the particle diameter) requiring large summations of pairwise interactions, which is compounded by the need to simulate large systems on account of the lengthscales of the structures that are formed. The

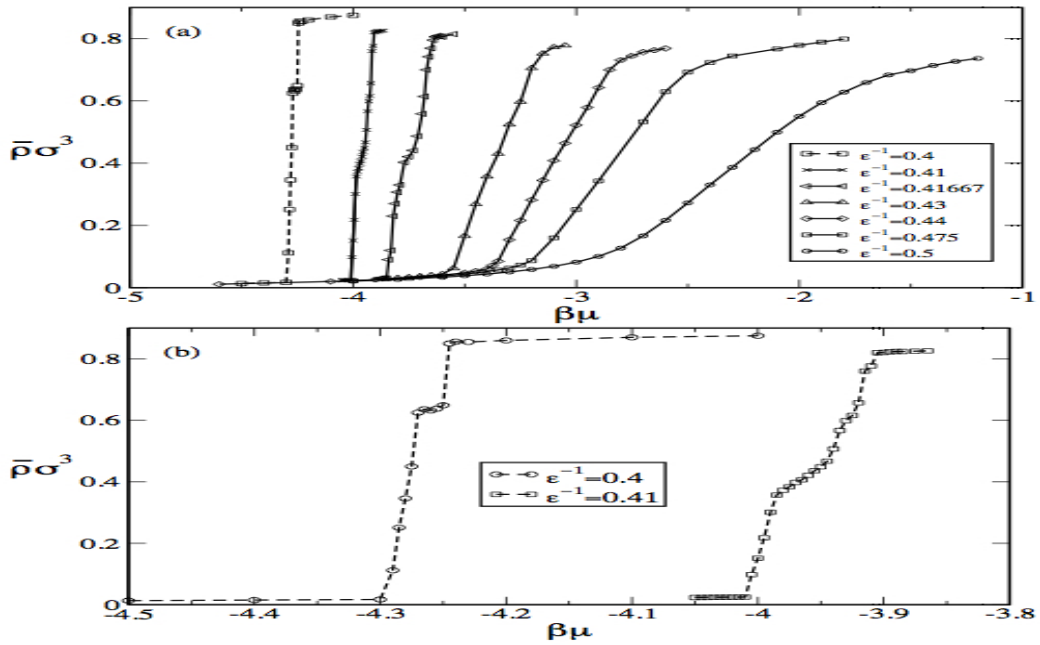

Figure 2.7: Plots of the mean system density as a function of chemical potential from MC simulations of a HC2YF by Archer and Wilding [5]. As the attractive strength is increased, the gradient of the curve becomes steeper and eventually kinks start to appear when $\epsilon^{-1} \sim 0.4$.

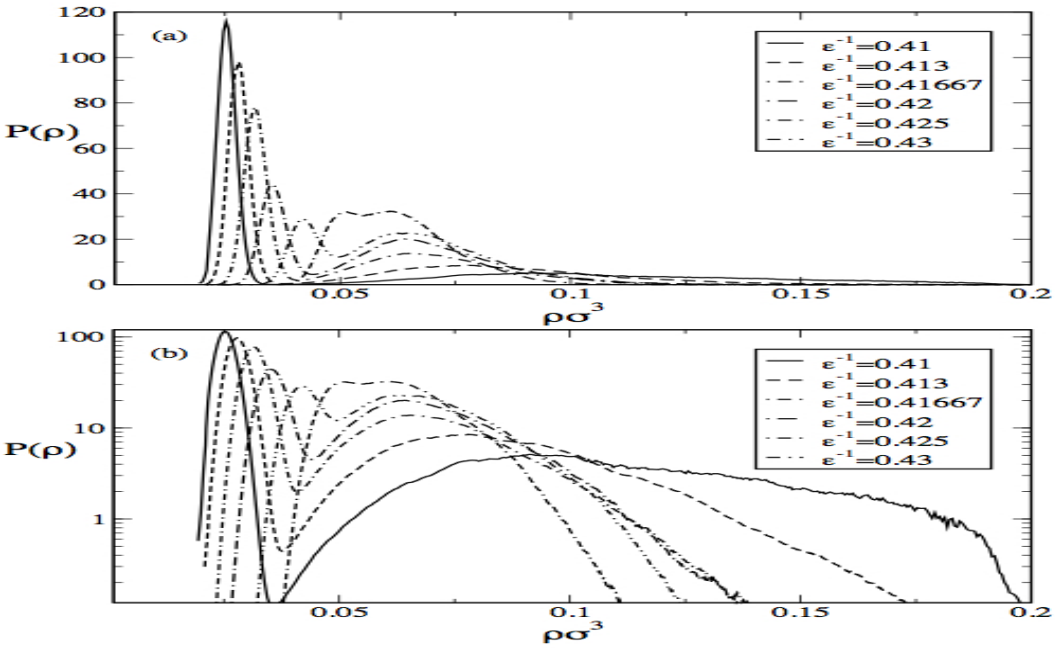

Figure 2.8: Distributions of densities sampled during MC simulations of a HC2YF by Archer and Wilding [5], plotted on both a linear (top panel) and logarithmic (bottom panel) scale.

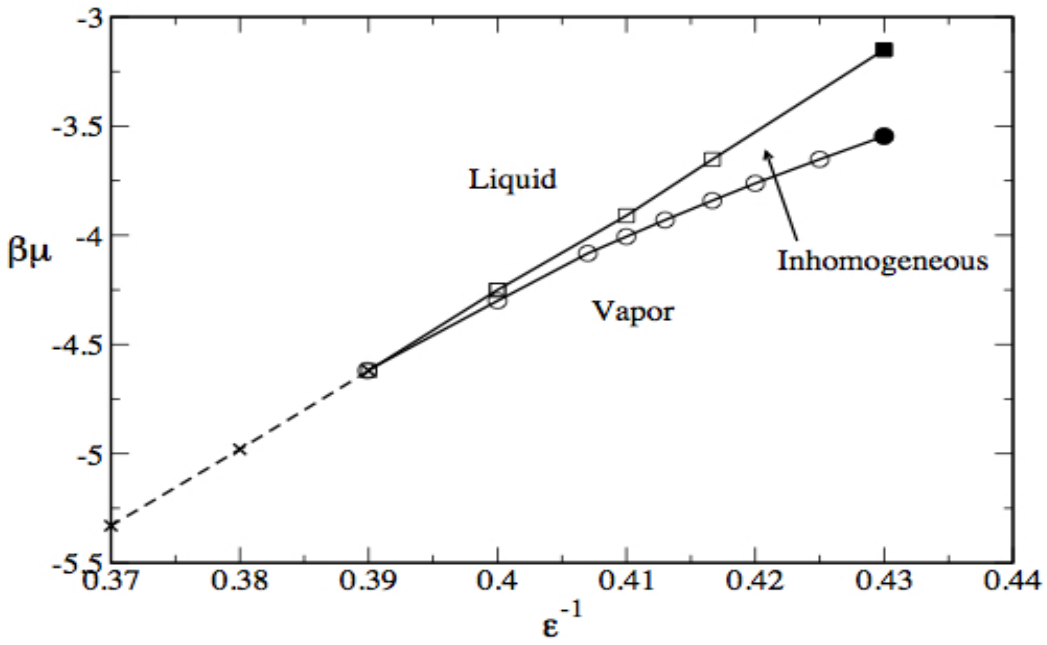

Figure 2.9: A sketch of the phase diagram for a HC2YF drawn by Archer and Wilding [5]. The line of liquid - vapour first order phase transitions diverges at $\epsilon^{-1} \approx 0.39$ and a region of inhomogeneous structures appears between the homogeneous phases.

prohibitive nature of this computational expense has left many questions regarding the phase behaviour of systems with competing interactions unanswered. The lack of data for different system sizes raises the question of the effect of finite system size on the simulation results. There is little in the way of understanding the nature of the coexistence of the clustered and unclustered phases and only few data points are available at higher densities. Finally there is the question as to how the phase diagram evolves as a long range repulsion is introduced to a purely attractive system.

In this thesis we attempt to mitigate much of the computational expense of MC by using a lattice MC model in the grand canonical ensemble. By placing the simulation on a lattice we are able to tabulate all of the pairwise interactions, significantly improving performance and thus the amount of data which can be collected. Our intention is to use this model to answer some of the questions listed above.

Chapter 3

Methods

3.1 Model Fluid

The model fluid which is the subject of this investigation is a colloidal fluid interacting via a hard–core two–Yukawa effective potential of the form

$$\beta v(r) = \begin{cases} \infty & r < \sigma \\ -\frac{\epsilon\sigma}{r} e^{-z_1((\frac{r}{\sigma})-1)} & \\ +\frac{A\sigma}{r} e^{-z_2((\frac{r}{\sigma})-1)} & r \geq \sigma \end{cases} \tag{3.1}$$

Here, $\beta = \frac{1}{k_B T}$ is the inverse temperature, while σ is the particle diameter. The first exponential Yukawa term represents an interparticle attraction whose strength is controlled by $\epsilon > 0$, while the second term represents a repulsion, with strength determined by $A > 0$. We shall focus on the regime where the range of the repulsion exceeds that of the attraction i.e. $z_1 > z_2$, which gives the potential an attractive head and repulsive tail.

When choosing the values of $z_1$and $z_2$we must take into account a number of competing factors. The attaction should not be so short ranged that the equilibrium liquid–vapour phase behaviour is preempted by freezing [43]. The range of the repulsion must be greater than that of the attraction and be sufficiently large enough that meaningful comparisons may be made with mean field theories, which become more accurate with increasing potential range. Finally, the range should not be so

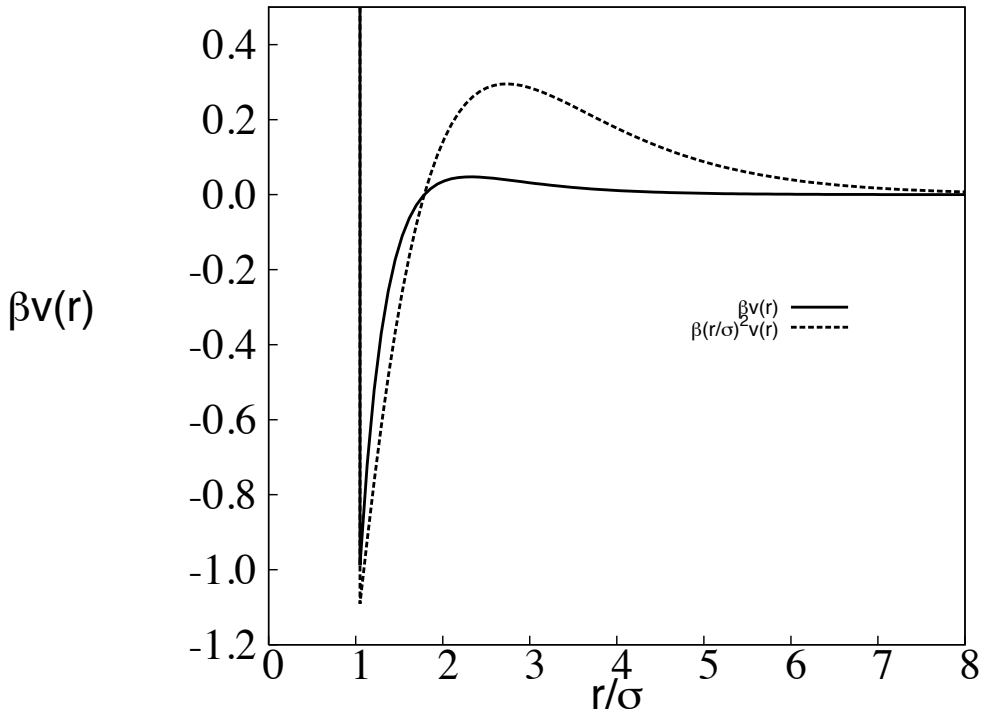

Figure 3.1: The form of the potential $\beta v(r)$ for $\epsilon = 2.2$, $A = 1$, $z_1 = 2$ and $z_2 = 1$. Also shown for comparison is the form of $(\frac{r}{\sigma})^2 \beta v(r)$

large that very large system sizes are needed to reduce the effect of cutoff artifacts when the potential is truncated. Choosing to set $z_1 = 2$ and $z_2 = 1$ seems to be a reasonable compromise between each of these considerations. An example of the form of the potential $\beta v(r)$ is presented in fig. 3.1. Also shown is $r^2 \beta v(r)$, which provides a useful indication of the total contribution of all neighbours along the potential.

3.2 Grand Canonical Monte Carlo

The grand canonical (constant chemical potential μ, volume V, temperature β) ensemble describes a system in thermodynamic equilibrium with an external reservoir. The internal energy and number density of the system are allowed to fluctuate by permitting particles to be exchanged with the external reservoir. In a Monte

Carlo simulation of a system with N particles, this is represented by proposing random trial moves that may either be particle insertions ($N \rightarrow N+1$) or removals ($N \rightarrow N-1$). The change in potential energy due to the proposed move is then calculated and the move accepted with a probability chosen such that the system follows a Boltzmann distribution.

Under Boltzmann statistics, the probability of a system being in state i with energy E_i is

$$p_i \propto \mathrm{e}^{-\beta E_i} \tag{3.2}$$

and the ratio of the probabilities of being in i and j is

$$\frac{p_j}{p_i} = \mathrm{e}^{-\beta \Delta E_{i \rightarrow j}} \tag{3.3}$$

with $\Delta E_{i \rightarrow j} = E_j - E_i$ the change in energy due to the transition from i to j . In the grand canonical ensemble, we define the total energy to be the sum of the potential energy from particle interactions U_i and the contribution from the chemical potential $-\mu N_i$, giving $\Delta E_{i \rightarrow j} = \Delta U_{i \rightarrow j} - \mu \Delta N_{i \rightarrow j}$ [103]. Hence the probability of a particle insertion ($N \rightarrow N+1$) is [104]

$$p_{N \rightarrow N+1} = \min\left(1, X\mathrm{e}^{-\beta(\Delta U_{N \rightarrow N+1} - \mu)}\right) \tag{3.4}$$

and for a particle removal

$$p_{N \rightarrow N-1} = \min\left(1, Y\mathrm{e}^{-\beta(\Delta U_{N \rightarrow N-1} + \mu)}\right) \tag{3.5}$$

where X and Y have yet to be determined.

To ensure that the ergodicity in the Monte Carlo simulation, it is sufficient to demonstrate that it observes detailed balance [105]. For detailed balance to be

observed, one must be able to demonstrate that, at equilibrium, the probability of transitioning from state i to state j is equal to the probability of the transition being reversed, for all i and j . The probability of $i \to j$ occuring is given by

$$\pi_{i\to j} = p_i \alpha_{i\to j} p_{i\to j} \tag{3.6}$$

with p_i the probability that the system is in state i , $\alpha_{i\to j}$ the probability that the move $i \to j$ is proposed and $p_{i\to j}$ being accepted, given that the system is in state i (the acceptance). Similarly, $\pi_{j\to i}$ is

$$\pi_{j\to i} = p_j \alpha_{j\to i} p_{j\to i}. \tag{3.7}$$

Hence, if detailed balance is observed it must be possible to demonstrate

$$\frac{\pi_{N\to N+1}}{\pi_{N+1\to N}} = 1. \tag{3.8}$$

Let $i \to j$ be a particle insertion and $j \to i$ be the removal that reverses it, such that

$$\frac{p_N}{p_{N+1}} \frac{\alpha_{N\to N+1}}{\alpha_{N+1\to N}} \frac{p_{N\to N+1}}{p_{N+1\to N}} = 1. \tag{3.9}$$

We know from equation (3.3) that

$$\frac{p_N}{p_{N+1}} = \mathrm{e}^{-\beta(\Delta U_{N+1\to N}+\mu)}. \tag{3.10}$$

Substituting this into equation (3.9) and choosing $\Delta E_{N\to N+1} < 0$ we are left with

$$\frac{1}{Y} \frac{\alpha_{N\to N+1}}{\alpha_{N+1\to N}} \frac{\mathrm{e}^{-\beta(\Delta U_{N\to N+1}+\mu)}}{\mathrm{e}^{-\beta(\Delta U_{N+1\to N}+\mu)}} = 1 \tag{3.11}$$

which then cancels to give

$$Y = \frac{\alpha_{N\to N+1}}{\alpha_{N+1\to N}}. \tag{3.12}$$

By definition

$$\alpha_{N\to N+1} = \frac{1}{V} \tag{3.13}$$

and

$$\alpha_{N+1\to N} = \frac{1}{N+1}. \tag{3.14}$$

So therefore, for detailed balance to be observed

$$Y = \frac{N+1}{V}. \tag{3.15}$$

By making a similar argument

$$\frac{p_{N+1}}{p_N}\frac{\alpha_{N+1\to N}}{\alpha_{N\to N+1}}\frac{p_{N+1\to N}}{p_{N\to N+1}} = 1 \tag{3.16}$$

we can also show that

$$X = \frac{V}{N+1}. \tag{3.17}$$

Hence, we can show that the grand canonical Monte Carlo simulation with insertion acceptance

$$p_{N\to N+1} = \min\left(1, \frac{V}{N+1}\mathrm{e}^{-\beta(\Delta U_{N\to N+1}-\mu)}\right) \tag{3.18}$$

and removal acceptance

$$p_{N\to N-1} = \min\left(1, \frac{N}{V}\mathrm{e}^{-\beta(\Delta U_{N\to N-1}-\mu)}\right) \tag{3.19}$$

does indeed observe detailed balance.

3.2.1 Grand canonical lattice Monte Carlo

One significant difference between the implementation of a lattice and off–lattice grand canonical Monte Carlo model is in the way we choose whether to attempt an insertion or deletion. In the off–lattice model, we first choose between an attempted insertion or deletion with equal probability and then choose which particle to attempt to delete or where to attempt an insertion accordingly. In the lattice model, we instead choose a lattice site at random and if it is empty, attempt to insert a particle there or if it is occupied, attempt to delete the occupying particle.

The effect of this subtle difference is that the values of X and Y described in the previous section are not required in the acceptance probabilities for trial moves in the lattice model, since they are already included in the probability of choosing an occupied or unoccupied lattice site. Therefore, for the lattice grand canonical Monte Carlo model the acceptance probabilities are

$$p_{N\to N+1} = \min\left(1, \mathrm{e}^{-\beta(\Delta U_{N\to N+1}-\mu)}\right) \tag{3.20}$$

and

$$p_{N\to N-1} = \min\left(1, \mathrm{e}^{-\beta(\Delta U_{N\to N-1}+\mu)}\right) \tag{3.21}$$

As described in chapter 1, one of the motivations for this project was to run simulations which are faster than the off–lattice model used by Archer and Wilding. Hence the decision was made to use a lattice Monte Carlo. The main benefit of using lattice Monte Carlo is the finite number of positions a particle may have relative

to its neighbour. This allows all possible pair–wise interactions to be calculated in advance and the values stored in a lookup table, which can greatly reduce the amount of time and resources spent on performing energy calculations over the course of the simulation. The major drawback of using a lattice model is the reduced degrees of freedom of particles in the system, which may introduce artifacts into the system behaviour which would not have appeared in an off–lattice model.

3.2.2 Calculating the Lattice Energy

Since the acceptance probability of a trial move in a grand canonical lattice MC simulation is dependent on the internal lattice energy U, we need a way to calculate the energy after each successful move.

For a lattice of volume V the total number of particles on the lattice N is given by

$$N = \sum_{i=1}^{V} s_i \tag{3.22}$$

with $s_i = 0$, 1 the occupancy of the lattice site i.

The interaction potential felt by a particle at site i as a result of a particle at site j is given by the interparticle potential from equation 3.1 with $r = \sigma = 1$ and $i \neq j$:

$$\beta v_{ij} = -\epsilon \mathrm{e}^{-z_1(r_{ij}-1)} + A\mathrm{e}^{-z_2(r_{ij}-1)} \tag{3.23}$$

where r_{ij} is the separation between sites i and j.

The lattice energy is the total energy as a result of all pair-wise interactions between particles on the lattice. This can be written in terms of the sum of the interaction potentials between all pairs of lattice sites $< i, j >$

$$U = \frac{1}{2} \sum_{<i,j>} s_i s_j \beta v_{ij} \tag{3.24}$$

where the factor of $\frac{1}{2}$ allows for double-counting and the product of s_i and s_j allows only contributions from pairs for which both sites are occupied.

It is common practice in computer simulations to truncate a pair-wise interaction potential, disregarding interactions of length greater than some cut off distance r_c [16]. The case where $R_c < \frac{L}{2}$, with L the length of the simulation box, is of particular interest when periodic boundary conditions are used, as in that case only interactions between a given particle and the nearest periodic image of any other particle need to be taken into account. If the interparticle potential is not zero for $r > r_c$ then truncation introduces an error into the energy calculation. For all results presented in this thesis a cutoff range of $r_c = 5\sigma$ was chosen, for which it was assumed that the value of $\beta v(r > r_c)$ was suitably small that any error introduced by the truncation was negligible.

3.3 Cluster Identification

When investigating the structure of a cluster forming fluid, it is useful to be able to determine the number of clusters, as well as the number of particles that make up those clusters. Figure 3.2 helps to illustrate how we do this. We begin by selecting a particle in the system at random (particle number 1 in figure 3.2) and finding all of its neighbours in the cluster (particles 2 to 5). These neighbours are then listed as being part of the same cluster as particle 1. We then look at each of these particles in turn and determine each of their neighbours, also listing them as being part of the same cluster. Once there are no more particles in the cluster with unlisted neighbours, we have found all of the particles in the cluster and hence its size. This process is repeated across all particles in the system until every particle has been listed as part of a cluster. Particles with no neighbours are listed as being in a cluster of size 1.

Since our system has long-range continuous interactions, we must allow for the fact that particle pairs that do not sit on adjacent sites may still be strongly interacting. As such, when determining whether two particles are neighbours we adopt a criterion which is similar to that used by Largo and Wilding [106]. We determine a pairwise interaction energy v between all pairs of paticles within the cutoff ra-

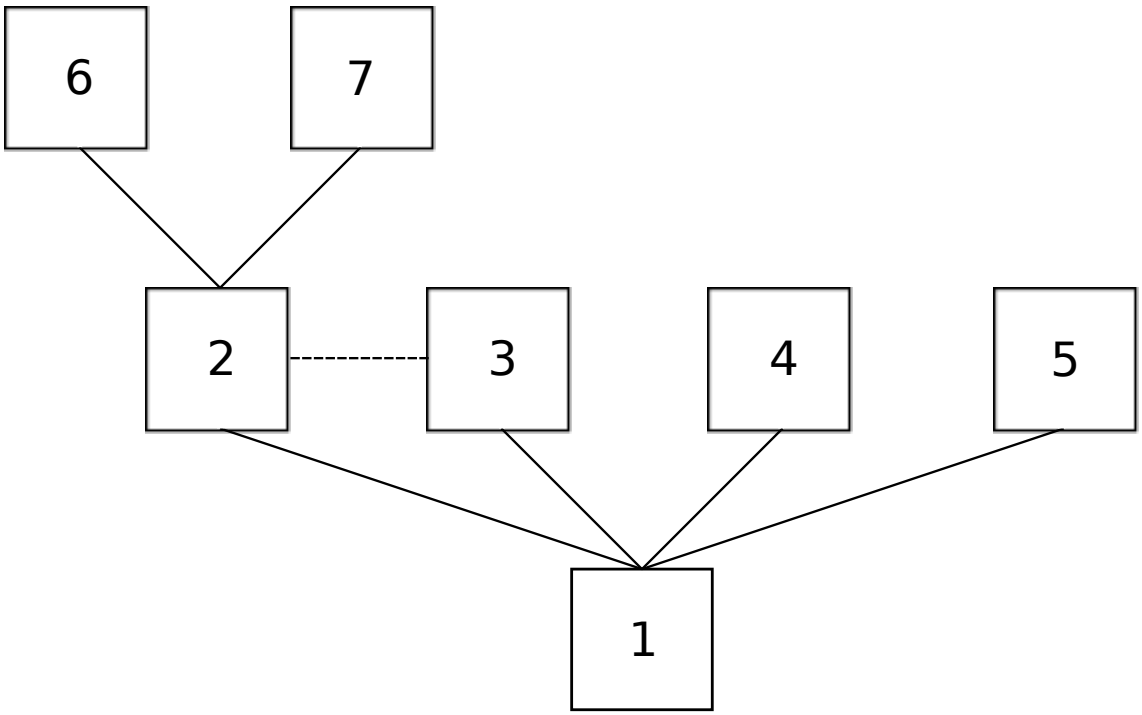

Figure 3.2: A diagram representing a sample cluster. Each box represents a single particle and the connections indicate neighbouring particles. Solid lines indicate that the neighbouring particles have yet to be marked as part of the same cluster, while dashed lines denote those that have. Choosing a particle at random (particle 1) we determine that particle's neighbours (particles 2 to 5). Each neighbour is marked as being in the same cluster as particle 1. We then look for the neighbours of each of these particles in turn. Particle 2 has one marked (particle 3) and two unmarked neighbours (particles 6 and 7), so we mark 6 and 7 as also being part of the same cluster. When there are no particles with unmarked neighbours remaining, we have found all particles in the cluster and thus know it's size. This process is repeated until all particles in the system are marked as part of a cluster. If a particle has no neighbours, it is placed into a cluster of size 1.

dius and assign a bond with probability $P_{\text{bond}} = 1 - \mathrm{e}^{(\beta v - \Delta)}$, with Δ an arbitrary parameter that we may use to tune the probability function.

3.4 Biasing in grand canonical Monte Carlo

First order phase transitions are characterised by a discontinuity in the first derivative of the order parameter [15]. As an example, figure 3.3 shows plots of system density as a function of time (in Monte Carlo sweeps) of lattice Monte Carlo simulations of an SALR fluid in the grand canonical ensemble with system parameters $\epsilon = 3.2$, $A = 1.0$, $z_1 = 2$, $z_2 = 1$ and $\mu = 6.5$ for a lattice of size 15^3 when the system starts with an empty (solid line) and full (dotted line) lattice. The simulation that was started in the empty lattice configuration, after remaining in a low density gas phase for some time, undergoes a sudden and large change in the particle number density, forming a high density liquid phase which is again very stable in time.

A schematic density distribution of a system near coexistence between two phases (gas and liquid) separated by a first order phase transition is shown in figure 3.4. The distribution has two distinct peaks that are close to being equal in weight and are separated by a wide region of low probability. It is this deep low-probability barrier which is the reason for the high stability of the two phases, the low probability of the system entering one of the configurations that separates the two peaks means that transitions between the two phases are rare. This stability acts as a barrier to the system finding its free energy minimum, since it may become trapped in a stable phase which is far from the absolute free energy minimum. Figure 3.3 illustrates this. Both the simulation started in the gas phase and the one started in the liquid phase remain in their initial state for a long time. It is only after $\sim 3 \times 10^5$ MCS that the simulation that was started in the gas phase finally transitions to the liquid phase. The phenomenon whereby a system's state is dependent on its starting condition is called hysteresis and in molecular simulations it can manifest itself as a blurring of the line of phase transitions.

Figure 3.5 serves as an example of the effect of hysteresis when we are trying to locate gas-liquid coexistence. It shows the mean density over the course of a simulation plotted as a function of the chemical potential for a hard-core 2-Yukawa

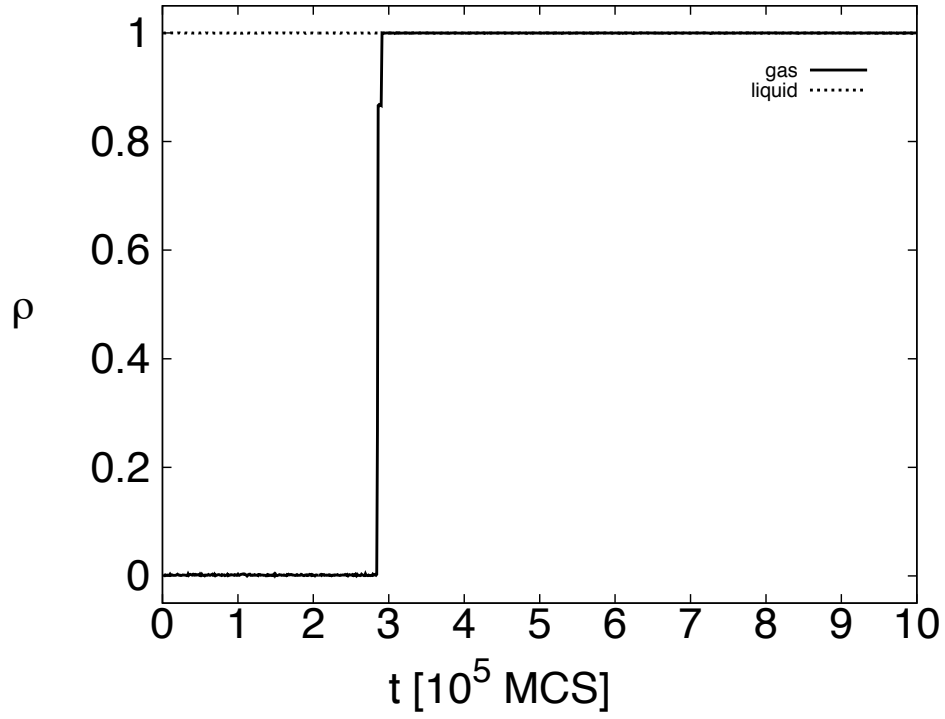

Figure 3.3: Data showing $\rho(t)$ for two simulations with identical parameters $\epsilon = 3.2$, $A = 1.0$, $z_1 = 2$, $z_2 = 1$ and $\mu = 6.5$, initialised in the gas (solid line) and liquid (dotted line) phases. The simulation initialised at low density remains at low density until approximately 30,000 lattice updates, when it undergoes a step change and ends up in the liquid phase.

fluid with $\epsilon = 3.2$, $A = 1.0$, $z_1 = 2$ and $z_2 = 1$ in a system with lattice size 15^3. Each point on the line represents the mean density measured for a single simulation at the given value of μ. Points on the solid line represent simulations that were started with an empty lattice (gas phase) and points on the dotted line represent simulations started with a full lattice (liquid phase).

Simulations started in the liquid phase underwent transitions to the gas phase for values of $\mu < -8.0$ whereas simulations started in the gas phase underwent transitions to the liquid phase for values of $\mu > -6.7$. If we were using these data to determine the value of μ at which the phase transition occurs then this represents a significant blurring of the line of phase transition. Indeed, even for $\mu > -6.7$ the mean densities for some of the simulations started in the gas phase dip well below 1.0. This is likely due to these simulations taking a considerable length of time to undergo the phase transition, further highlighting the effects of hysteresis.

3.4.1 Umbrella sampling

For a system in the grand canonical (constant V, β, μ) ensemble the number probability density function $p(N)$ takes the form of an average over all possible particle positions:

$$p(N) = \frac{1}{Z} \prod_{i=1}^{N} \left\{ \int_V dr_i \right\} \mathrm{e}^{-\beta E} \tag{3.25}$$

with $\mathcal{H}(\{\boldsymbol{r}\}, N) \equiv E(\{\boldsymbol{r}\}) - \mu N$ the Hamiltonian, Z the partition function and $\{\boldsymbol{r}\}$ the set of all particle coordinates [107][108][109].

Instead of sampling from a simple Boltzmann distribution with Hamiltonian $\mathcal{H}(\{r\}, N)$, an umbrella sampled simulation follows a modified distribution with effective Hamiltonian

$$\tilde{\mathcal{H}} = \mathcal{H} + \eta(N), \tag{3.26}$$

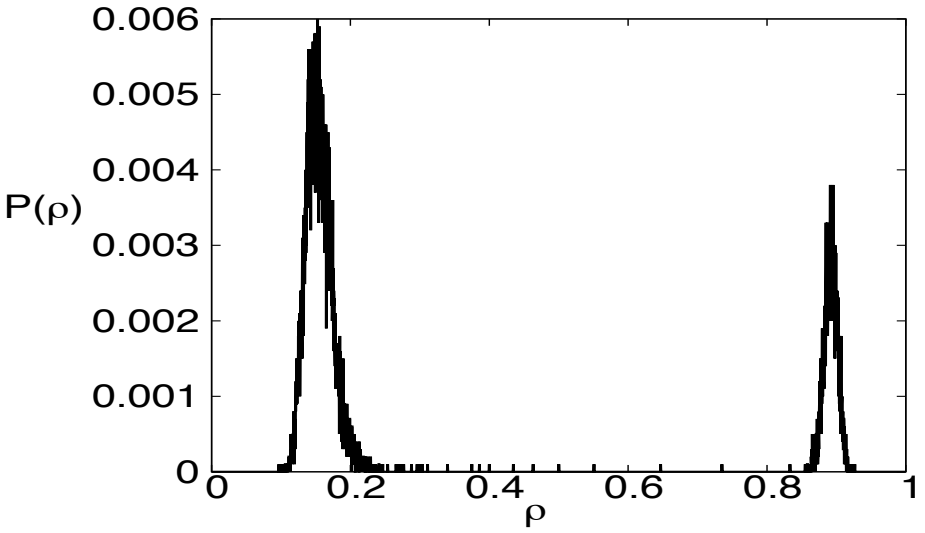

Figure 3.4: A density distribution showing two peaks corresponding to two coexisting phases. Between the two peaks is a region of low probability through which the system must traverse to transition from one phase to the other.

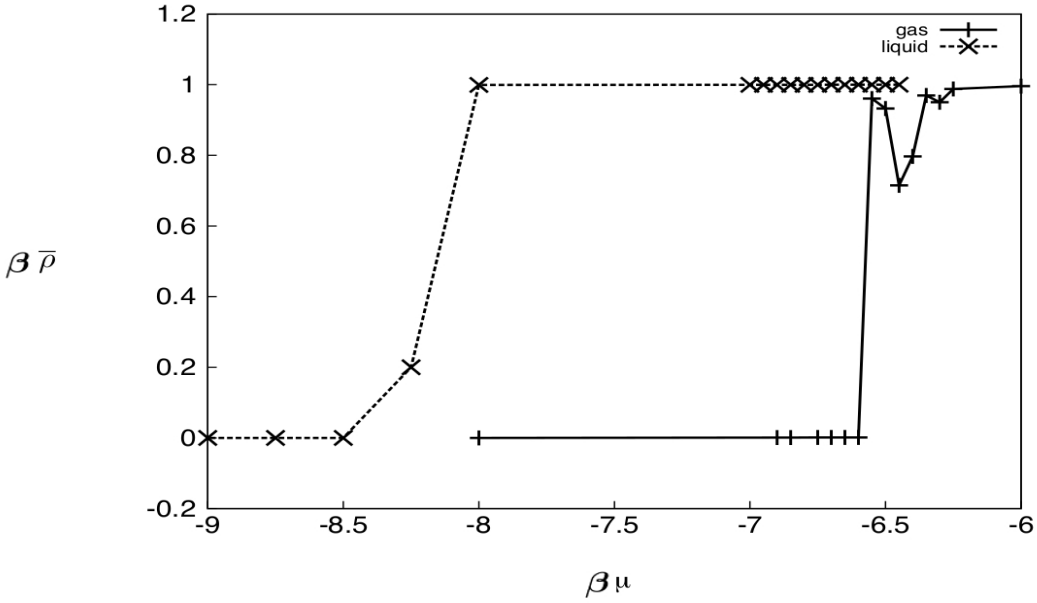

Figure 3.5: Plot of the mean density $\overline{\rho}$ as a function of chemical potential μ for simulations initialised in the gas (solid line) and liquid (dotted line) phases. The effects of hysteresis can be seen by the strong correlation between the initial and mean densities.

where $\eta(N)$ is a preweight function in particle number N.

The probability distribution from such a simulation is given by

$$\tilde{p}(N) = \frac{1}{Z} \prod_{i=1}^{N} \left\{ \int_V dr_i \right\} \mathrm{e}^{-\beta \tilde{\mathcal{H}}}. \tag{3.27}$$

If one were to choose $\eta(N) = \ln p(N)$ such that $\tilde{\mathcal{H}} = \mathcal{H} + \ln p(N)$ we can see from equation (3.27) that $\tilde{p}(N)$ becomes a constant for all N. Hence the simulation should perform a one–dimensional random walk over the range of available densities, allowing very efficient sampling of the preweighted histogram $\tilde{p}(N)$.

If a simulation is performed with a suitable preweighting function to obtain good statistics for $\tilde{p}(N)$, we may obtain $p(N)$ for the simulation by unfolding the effects of the preweighting. Since we have complete knowledge of $\eta(N)$ this may be achieved by simply dividing out the effects of $\eta(N)$ from $\tilde{p}(N)$ to yield $p(N)$. This $p(N)$ may then be used as a more refined approximation for the preweight function, and a new simulation run in the hope of obtaining still better statistics for $p(N)$.

The preweight function is usually applied by modifying the simulation acceptance probabilities to include $\eta(N)$ such that

$$\begin{aligned} \tilde{p}_{N \to N+1} &= \eta(N) p_{N \to N+1} \\ \tilde{p}_{N \to N-1} &= \eta(N) p_{N \to N-1} \end{aligned} \tag{3.28}$$

Unfortunately, the ideal preweight function $\eta(N) = \ln p(N)$ cannot be determined in general since it is the logarithm of the function which we are trying to find. Therefore, we must find a way of approximating $\ln p(N)$ well enough that the phase transitions occur with an acceptably high frequency.

3.4.2 Histogram Reweighting

Histogram reweighting makes use of the observation that histograms of observables accumulated at one set of parameters β and μ can provide estimates of the histograms for another set of parameters β' and μ' [110][109].

Let us consider the joint probability distribution of the internal energy U and particle number N for our system given ϵ, A and μ [107].

$$p(N, U, \epsilon, A, \mu) = \frac{1}{Z} \prod_{i}^{N} \left\{ \int_{V} dr_i \right\} \delta(U - U(\{\boldsymbol{r}\})) \mathrm{e}^{-\beta E} \tag{3.29}$$

where Z is the partition function, $\frac{1}{Z} \prod_{i}^{N} \left\{ \int_{V} dr_i \right\}$ gives the product of the probabilities of all possible microstates, $\delta(U - U(\{\boldsymbol{r}\}))$ is a Kroneker delta function rejecting all microstates that do not yield the required internal energy U and $E(N, U, \epsilon, A, \mu)$ is the total energy of the system. Similarly, the distribution at a different set of parameters ϵ', A', μ' can be written as

$$p(N, U, \epsilon', A', \mu') = \frac{1}{Z} \prod_{i}^{N} \left\{ \int_{V} dr_i \right\} \delta(U - U(\{\boldsymbol{r}\})) \mathrm{e}^{-\beta E'}. \tag{3.30}$$

Taking the ratio of the two distributions:

$$\frac{p(N, U, \epsilon', A', \mu')}{p(N, U, \epsilon, A, \mu)} = \mathrm{e}^{-\beta(E' - E)} \tag{3.31}$$

Thus, to map the measured histogram $p(N, U, \epsilon, A, \mu)$ onto $p(N, U, \epsilon', A', \mu')$ all we must do is find the reweighting factor $W = e^{-\beta(E' - E)}$.

In our simulation, we have defined the total system energy $E(\epsilon, A, \mu) = U(\epsilon, A) - \mu N$. Since it is useful to be able to reweight the histogram in terms of the attractive and repulsive strengths independently, we split U into its attractive and repulsive terms

U = -$U_a + U_r$ (3.32)

with $U_a = \epsilon u_a$ and $U_r = A u_r$ the total attractive and repulsive energy respectively such that

$$E = \beta(-\epsilon u_a + A u_r - \mu N). \tag{3.33}$$

From this it is clear that we can set β to unity in our simulations without loss of generality by including the temperature of the system implicitly in the values of ϵ, A and μ.

Hence we may write the reweighting factor W as

$$W = \mathrm{e}^{-(\epsilon'-\epsilon)u_a+(A'-A)u_r-(\mu'-\mu)N} \tag{3.34}$$

and so equation (3.31) becomes

$$p(N, U, \epsilon', A', \mu') = p(N, U, \epsilon, A, \mu)\mathrm{e}^{-(\epsilon'-\epsilon)u_a+(A'-A)u_r-(\mu'-\mu)N} \tag{3.35}$$

In principle, a single simulation at one point in parameter space is sufficient to obtain information for all other points. Unfortunately, due to finite sampling, it is not possible in practice to reweight a single histogram obtained at ϵ, A, μ to obtain one for ϵ', A', μ' an arbitrary distance away in parameter space. The problem occurs when we try to apply the reweighting factor to configurations that occur only very rarely in simulation and so have a high statistical uncertainty associated with them. These configurations have very low Boltzmann weights at ϵ, A, and μ and as such do not make a significant contribution to the statistical uncertainties in the expectation values of observables at ϵ, A, μ. However, when reweighting to ϵ', A', μ', these configurations may be assigned a much greater statistical weight that does not reflect their actual representation in the overall sample. The effect is to magnify

the overall statistical error of the measured expectation values and is visible in a reweighted histogram that appears "ragged" in its tail regions.

3.4.3 Mapping out a line with histogram reweighting

To draw the phase diagram of a system, one needs to map out the various lines of transitions between states. Ordinarily, to do this requires the use of parameter sweeping (varying a single parameter between simulations until the desired transition is observed), manually searching for each point on the line. This is very time consuming as it requires a large number of simulations to be run to locate even a single point on the phase diagram. Fortunately, there are more efficient ways of mapping out the features of a phase diagram.

The techniques of histogram reweighting and biased Monte Carlo can be combined to allow one to trace a line of transitions on a phase diagram much more efficiently than simple parameter sweeping for each point individually. Once an estimate for a point on the line has been obtained through parameter sweeping, one can apply histogram reweighting in order to refine the estimate. The resulting distribution may then be used as a preweight function for a simulation at the new estimate. Having thus obtained a distribution from a reasonable estimate at one point on the line, we can now obtain an estimate for a new point at a different set of parameters, with the use of histogram reweighting. Since we are unable to reweight an infinite distance away from the distribution, we must run a simulation at the new point which will allow us to reweight further along the line. By repeating this process the entire length of the line may be mapped out, stepping along the line with histogram reweighting and then running simulations so as to reweight to the next point. The process is illustrated in the flow digram in figure 3.6.

3.5 Transition Matrix Monte Carlo

In the previous section we have seen how one can use estimates of a distrbution as a preweighting function to improve statistical sampling and obtain a more refined

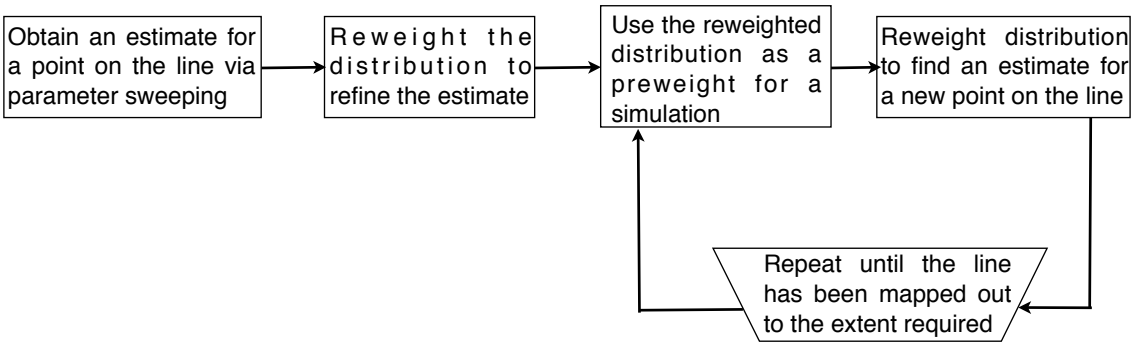

Figure 3.6: A flow chart to illustrate the process for using histogram reweighting and biased Monte Carlo to map out a line on a phase diagram.

estimate in an iterative process. Often a single iteration is enough to provide an acceptable approximation to the distribution. However, in cases where the barrier to transition is very high, or in cases where there are a number of barriers to be overcome, we may have to go through several iterations of our preweight function before we have reasonable statistics across the whole range of interest. In these cases it is useful to have some method of automating the iterative process, rather than having to constantly run new simulations manually. Transition matrix Monte Carlo is one such method.

The general idea of the transition matrix method for determining weight functions is to record the acceptance probabilities of all attempted transition and extract the states' relative probabilities from it. As all attempted transitions contribute to the weight function, it can potentially be obtained more quickly than other methods.

3.5.1 Implementing the Transition Matrix Method

For every attempted Monte Carlo move the acceptance probability is stored in a collection matrix C:

$$C(N \to N') \Rightarrow C(N \to N') + p_a. \tag{3.36}$$

At the same time, the probability for rejecting the move and thereby keeping the current value of N is also stored:

$$C(N \to N) \Rightarrow C(N \to N) + (1 - p_a). \tag{3.37}$$

It is important to note that these probabilities p_a are the bare acceptance probabilities and do not include any weights.

The transition probabilities are then calculated by normalising the collection matrix:

$$T(N \to N') = \frac{C(N \to N')}{\sum_k C(N \to N_k)}, \tag{3.38}$$

with the sum on the right hand side including all possible states to which the system can jump from a given state. For a lattice Monte Carlo simulation in the most general case, this would create a $V \times V$ transition matrix, with V being the number of lattice sites in the simulation. The desired probability distribution $p(N)$ of the order parameter is the eigenvector corresponding to the largest eigenvalue.

However, in the case of the model used for this thesis, transitions only take unit steps in N, implying that the transition matrix is tridiagonal. Hence the ratio of the probabilities for two points in the probability distribution $p(N)$ and $p(N+1)$ can be determined from the transition matrix via

$$\frac{p(N+1)}{p(N)} = \frac{T(N \to N+1)}{T(N+1 \to N)}. \tag{3.39}$$

Hence we can determine the difference between the corresponding points in the preweight function $\eta(N+1) - \eta(N)$ by taking the logarithm

$$\eta(N+1) - \eta(N) = \ln\left(\frac{T(N \to N+1)}{T(N+1 \to N)}\right). \tag{3.40}$$

Where either $\eta(0)$ or $\eta(V)$ may be chosen to be some fixed value to allow us to compute the rest of the function.

Thus, by acculmulating relative probabilities of transitions between values of N in the transition matrix over the course of a simulation, we are able to build up an estimate of the preweighting probability distribution $\eta(N)$ which may then be applied to a biaseed Monte Carlo simulation as described in section 3.4.1.

Repeatedly updating $\eta(N)$ from the transition matrix allows us to systematically extend the range of N over which statistics for the preweight function are accumulated. However, since updating the preweight function during a simulation violates detailed balance, we chose to do this at infrequent intervals of 10,000 lattice updates.

Even when using transition matrix Monte Carlo there were points in the course of this project when simulations progressed very slowly. Figure 3.7 is a plot of system density as a function of simulation time $\rho(t)$ (a "time series") for a transition matrix Monte Carlo simulation of the hard-core 2-Yukawa fluid near a first order phase transition. The simulation starts in the liquid phase and eventually finds its way to the gas phase after $\sim 2 \times 10^6$ lattice updates. Successive updates of the preweight function from the transition matrix do then allow the range of ρ sampled after reaching the gas phase to grow, but only very slowly. Figure 3.7 took several days of CPU time to generate and the simulation is still far from providing sampling over the full range of ρ by the end.

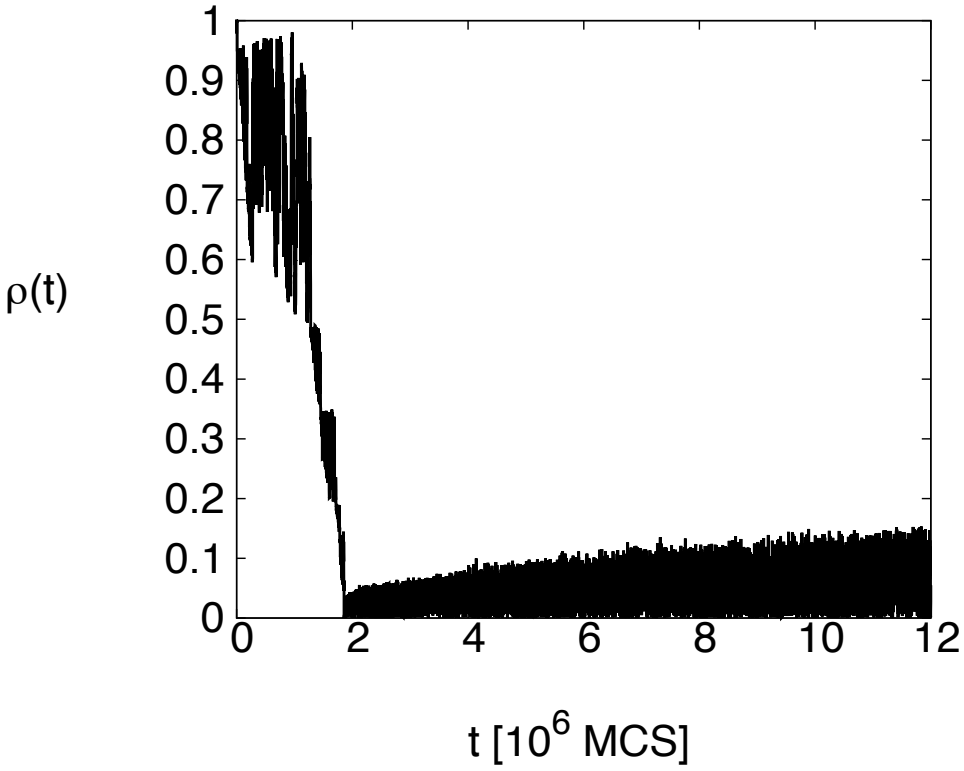

Figure 3.7: A time series for a transition matrix Monte Carlo simulation. Demonstrating how, even with the transition matrix method of biasing, simulations of the HC2YF can still be slow to obtain a preweight. This data took several days of CPU time to generate and the preweight is still far from providing full sampling in ρ.

To overcome this difficulty, we made the decision to divide up the simulation into windows, each limited to a specific range in ρ. Using transition matrix Monte Carlo simulations, we were able to obtain a preweight for each window in far less time than it would have taken to generate a preweight for the whole range. The overlapping probabilities between windows can be made equal through multiplication of the preweight of each window by a constant. One may then 'stitch' the preweights together to provide a single preweight covering the entire range of ρ. The values of the constants may be arbitrary, since it is only the relative probabilities that need be preserved.

3.5.2 Example of how biased Monte Carlo can improve statistical sampling

As an example of how biased Monte Carlo can improve statistical sampling in a simulation, figure 3.8 shows a time series plot of the system density $\rho(t)$ from an unbiased simulation that ran for 8×10^6 Monte Carlo Sweeps (MCS). The simulation was run with parameters of $A = 1.0$, $\epsilon = 2.9$, $\mu = -5.91$, $z_1 = 2$ and $z_2 = 1$. There are a few distinct states visible from the time series of this simulation, one of which is at a low density ($\rho \sim 0$) and the others shown by relative stability of certain values of $\rho > 0$. This simulation ran for a total of 24 hours CPU time and in that time the system seems to have undergone transitions between various states approximately 35 times.

By applying a bias to the simulation we raise the probability of the barrier configurations so that they are on the order of those in the peaks. This effectively reduces the barrier to transitions so that the system may move back and forth between different states freely during the simulation. Removing the bias from the distribution once the simulation has finished leaves us with the "true" Boltzmann distribution. This allows us to sample the transitions between states far more frequently and gives a more accurate estimate for the relative statistical weights of the peaks in the distribution. Figure 3.9 shows a time series for a simulation that was biased using the transition matrix Monte Carlo biasing method. Although the time scale for this simulation is only one tenth that of the simulation in fig 3.8 (8×10^5 MCS), the number of transitions between the low and high density states is much higher.

This shows us that biasing permits the sampling of transitions between states at a much higher frequency than for an unbiased simulation, and that it offers significant savings in CPU time while also providing better estimates for the locations of important features on the phase diagram. Whenever possible, we have made use of biasing techniques to speed up the simulation process.

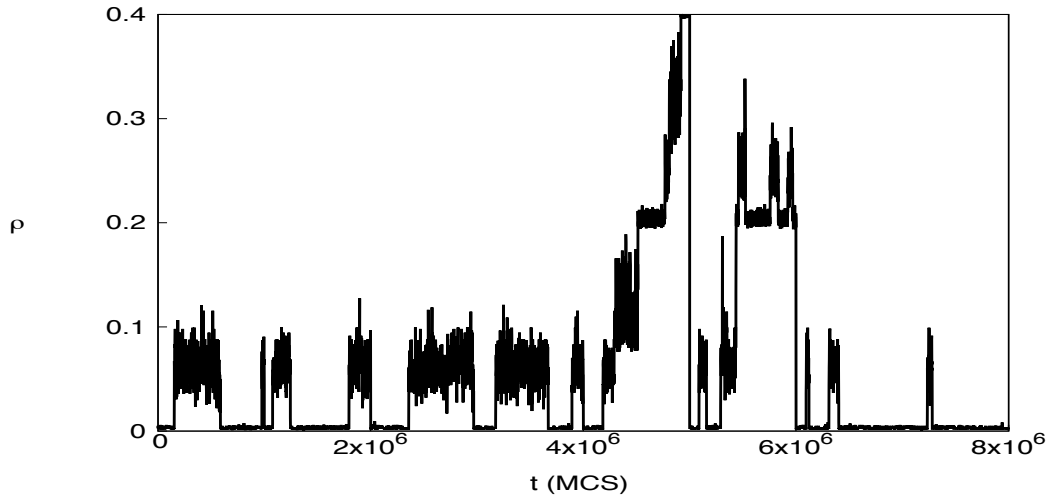

Figure 3.8: Time series plot of the system density ρ as a function of time t, measured in terms of the number of Monte Carlo sweeps (MCS). This is a time series for an unbiased simulation at $A = 1.0$, $\epsilon = 2.9$, $\mu = -5.91$, $z_1 = 2$ and $z_2 = 1$. Note that transitions between gaseous and heterogeneous states are relatively rare.

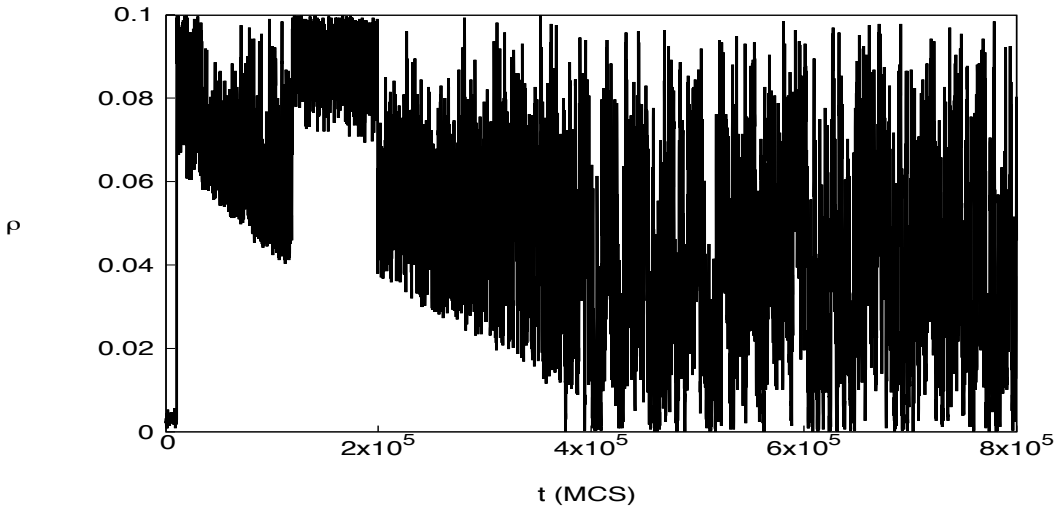

Figure 3.9: A time series $\rho(t)$ for a biased simulation at $A = 1.0$, $\epsilon = 2.9$, $\mu = -5.91$, $z_1 = 2$ and $z_2 = 1$. The simulation was biased using the transition matrix Monte Carlo method described in section 3.5 and the result is a much larger number (and hence better statistical sampling of) transitions between gaseous and heterogeneous states, despite the shorter timescale of this simulation.

Chapter 4

Introducing Repulsion to the System

4.1 3-Dimensional Phase Diagram

Before we can begin to investigate the heterogeneous behaviour, we need to understand the conditions which are needed for heterogeneity. Archer and Wilding proposed that a 3-dimensional phase diagram of the hard-core 2-Yukawa fluid (HC2YF) in inverse attractive strength ϵ^{-1}, chemical potential μ and repulsive strength A might take the form shown in figure 4.1 [5]. The schematic shows a surface of first-order gas-liquid phase transitions at low A which is bounded along one edge by a line of critical points. This critical line terminates at a Lifshitz (multicritical) point at some value of $A = A_L$, beyond which the surface of first-order gas-liquid phase transitions is instead bounded by a triple line which tends monotonically towards $\epsilon^{-1} = 0$ with increasing A and μ. Past the triple line is a region of heterogeneous structures between the gas and liquid phases which is capped off by a surface of continuous transitions at high ϵ^{-1}.

4.2 Comparison to the 3D Ising Model

Before proceeding to investigate the behaviour of the system in this region of heterogeneity, one must first determine the values of the repulsion A for which the

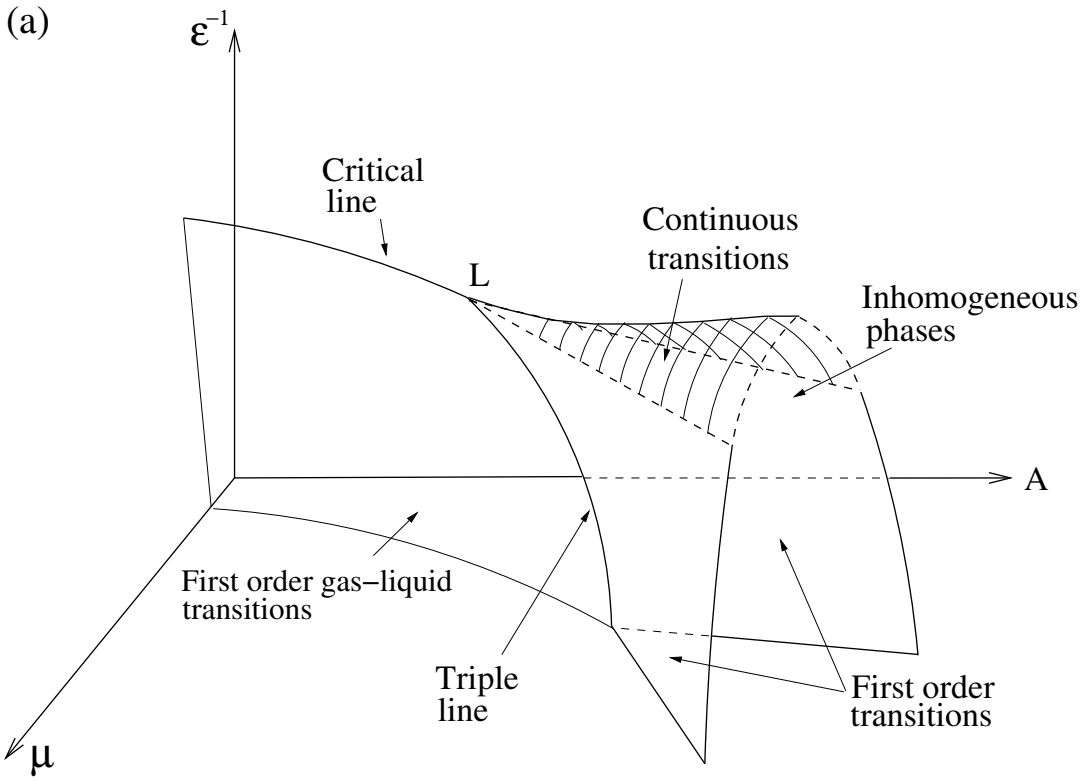

Figure 4.1: Schematic of a 3-dimensional phase diagram in ϵ^{-1}, μ and A for a SALR fluid, as proposed by Archer and Wilding taken from [5].

heterogeneous structures are stable. Figure 4.2 shows a comparison between a density distribution of a HC2YF for $A = 0.0$, $\epsilon = 0.336$, $\mu = -2.227$, close to criticality, and the distribution of magnetisation $P(M)$ of a 3D spin-half Ising model as determined by Tsypin and Blöte [6] (β is set to unity for all density distributions shown).

The order parameter of an Ising model is its magnetisation M expressed as

$$M = \frac{1}{N} \sum_{i=1}^{N} s_i \tag{4.1}$$

where N is the total number of spin sites in the Ising model and $\sum s_i$ is the sum of all spins s_i in the system with $s_i = \pm 1$. Since M thus varies in the range $[-1, 1]$, in order for a comparison to be made between these two distributions we have scaled our density distribution (which ordinarily varies in the range $[0, 1]$) and shifted it such that it is centered around the origin and varies in the range $[-1, 1]$.

The close agreement between these two distributions is a strong indication that, for zero repulsion, the Yukawa fluid belongs to the Ising universality class.

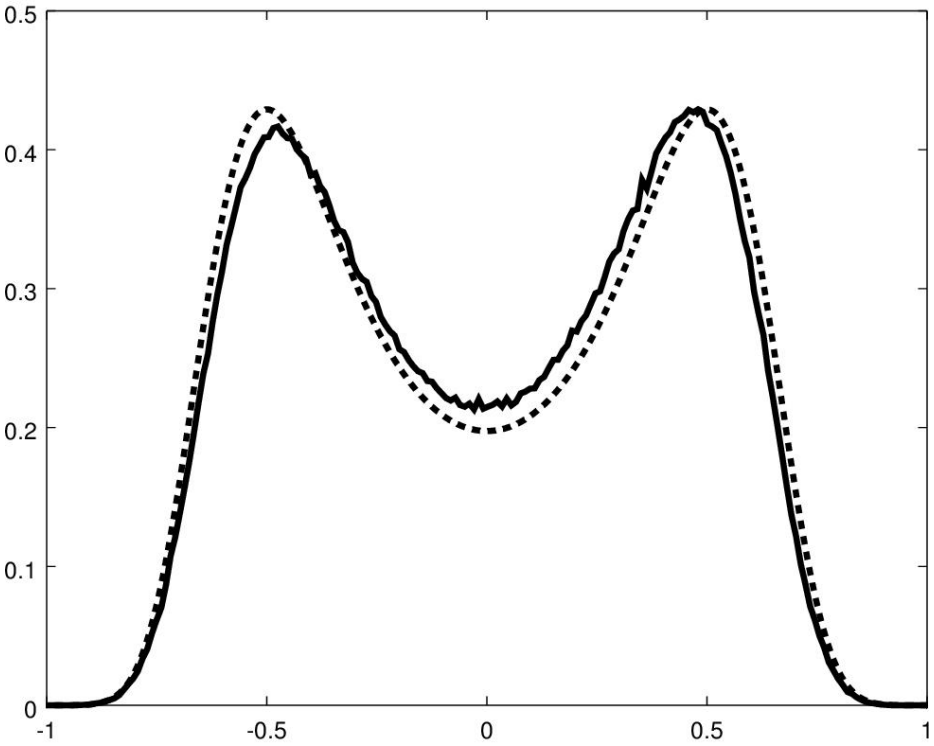

Figure 4.2: Comparison between the distributions of a HC2YF (solid line) with repulsion $A = 0.0$, attractive strength $\epsilon = 0.336$ and chemical potential $\mu = -2.227$ and that of a 3D Ising model at criticality (dashed line), as measured by Tsypin and Blöte [6]. The Yukawa distribution has been scaled and shifted so as to fit on the same axes as the Ising model distribution, to permit comparison. The two distributions show good agreement in their shape.

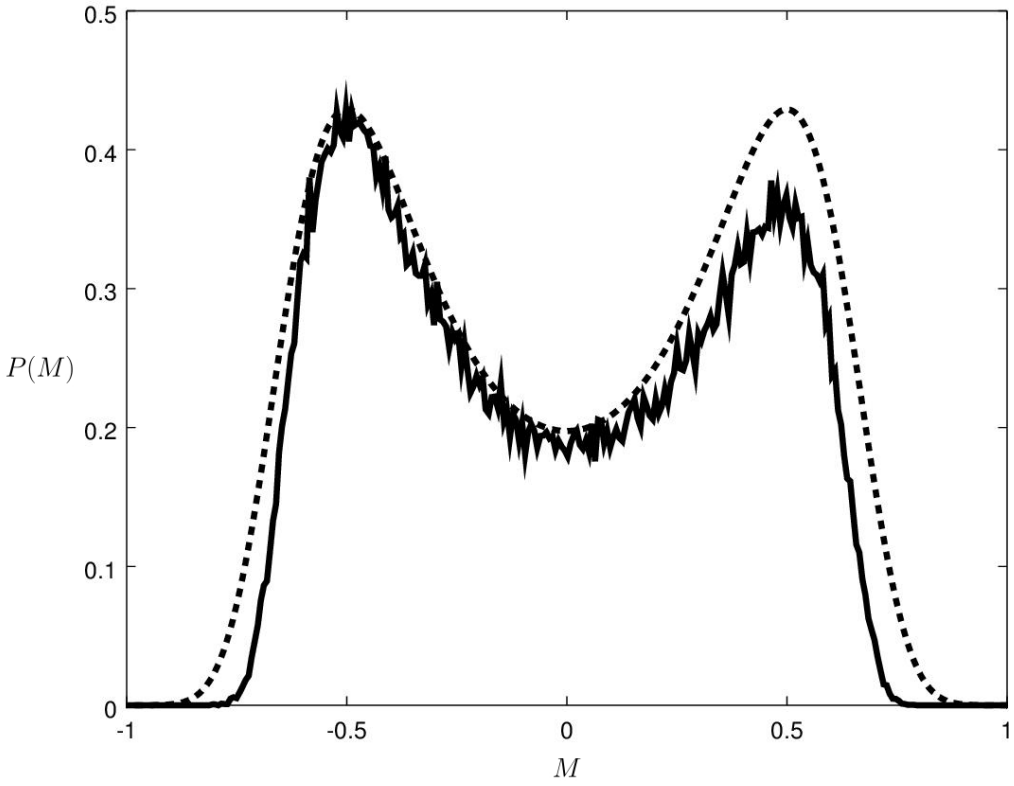

Figure 4.3: Comparison between the distributions of a HC2YF (solid line) with repulsion $A = 0.15$, attractive strength $\epsilon = 0.697$ and chemical potential $\mu = -2.575$ and that of a 3D Ising model at criticality (dashed line), as measured by Tsypin and Blöte [6]. The Yukawa distribution has been scaled and shifted so as to fit on the same axes as the Ising model distribution, to permit comparison. As in figure 4.2 the two distributions are in good agreement.

As repulsion is introduced to the system (A increased gradually from zero), one observes that the phase behaviour begins to depart from that of the Ising universality class. When $A = 0.15$ (figure 4.3) the HC2Y distribution is still in good agreement with that of the 3D Ising model. However, when the repulsive strength is increased further to $A = 0.2$ (figure 4.4) the shape of the distribution from the HC2YF is noticeably different to the distribution from the 3D Ising model.

4.3 Emergence of Heterogeneity

Figure 4.5 shows the density distributions $P(\rho)$ for the HC2YF at $A = 0.0$, 0.15, 0.2 and 0.3. It is clear that, once the repulsive strength reaches $A = 0.3$, any similarities between the HC2YF phase behaviour and that of a 3-dimensional Ising

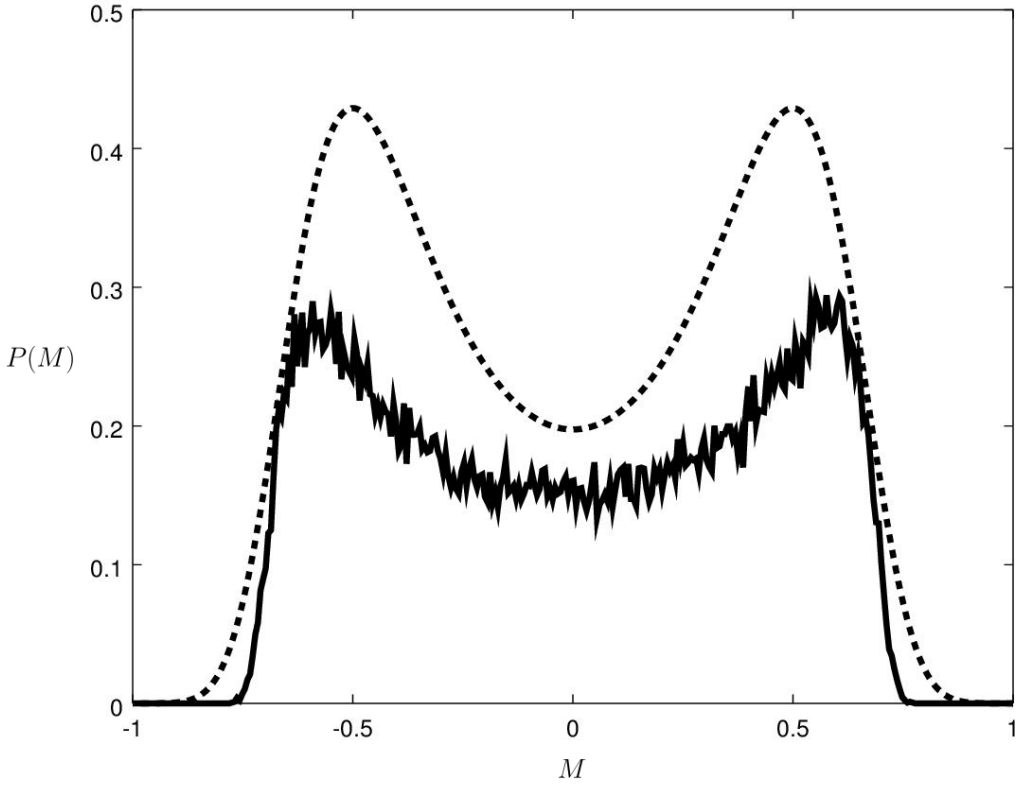

Figure 4.4: Comparison between the distributions of a HC2YF (solid line) with repulsion $A = 0.2$, attractive strength $\epsilon = 0.830$ and chemical potential $\mu = -2.777$ and that of a 3D Ising model at criticality (dashed line), as measured by Tsypin and Blöte [6]. The Yukawa distribution has been scaled and shifted so as to fit on the same axes as the Ising model distribution, to permit comparison. Unlike figures 4.2 and 4.3, the shape of the HC2Y distribution is notably different to that of the Ising model.

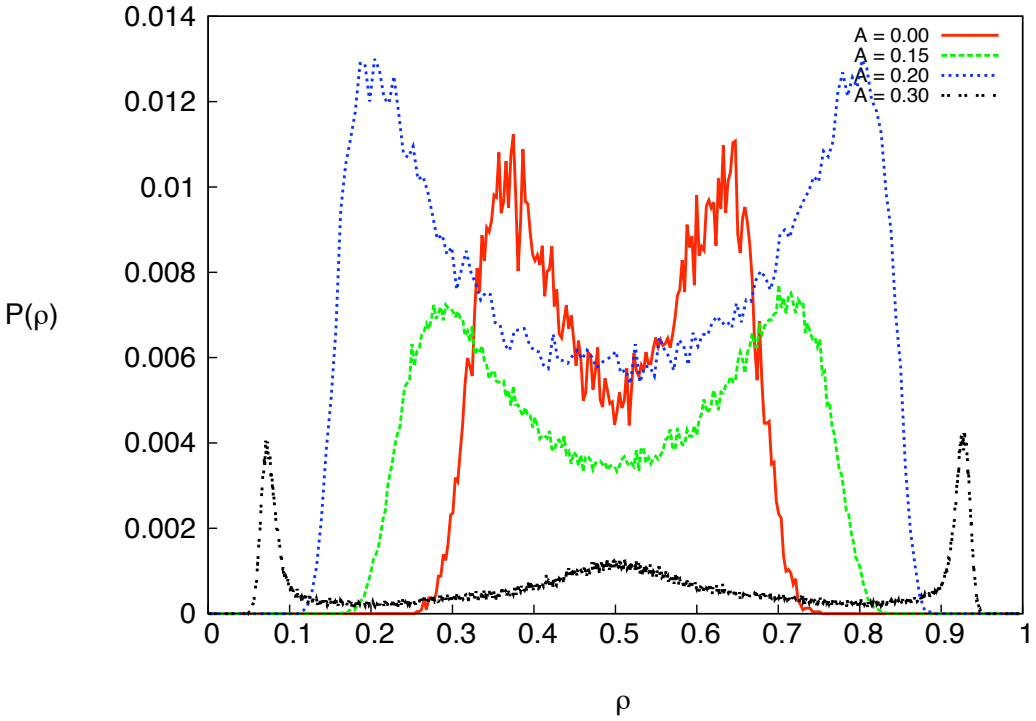

Figure 4.5: Comparison of the density distributions $P(\rho)$ of 4 different Yukawa fluids. Parameters are red: $A = 0.0$, $\epsilon = 0.336$, $\mu = -2.227$; green: $A = 0.15$, $\epsilon = 0.697$, $\mu = -2.575$; blue: $A = 0.2$, $\epsilon = 0.830$, $\mu = -2.777$; black: $A = 0.3$, $\epsilon = 1.107$, $\mu = -3.249$. As A is increased, the two peaks become more widely separated, showing that the barrier to transition between the gas and liquid phases becomes harder to traverse. By the time the repulsion has reached $A = 0.3$ a third peak has appeared between the gas and liquid phases, which we believe to be caused by the appearence of stable heterogeneous structures.

model disappear. At $A = 0.3$ the peaks corresponding to the gas and liquid phases are strongly separated and a new peak has emerged between them. An example configuration from beneath this peak is shown in figure 4.6. The picture shows regions of high and low density, with no clearly discernable barrier between the two.

If we relate the progression of distributions with increasing A in figure 4.5 to the 3-dimensional phase diagram in figure 4.1 then we can see that the distributions in the range $0.0 \leq A < 0.3$ are in fact on the critical line. At $A = 0.3$ we no longer see a twin peaked density distribution, but instead there is an additional peak between the gas and liquid phases which corresponds to non-homogeneous states. Placing this distribution on the 3-dimensional phase diagram leads us to conclude that the

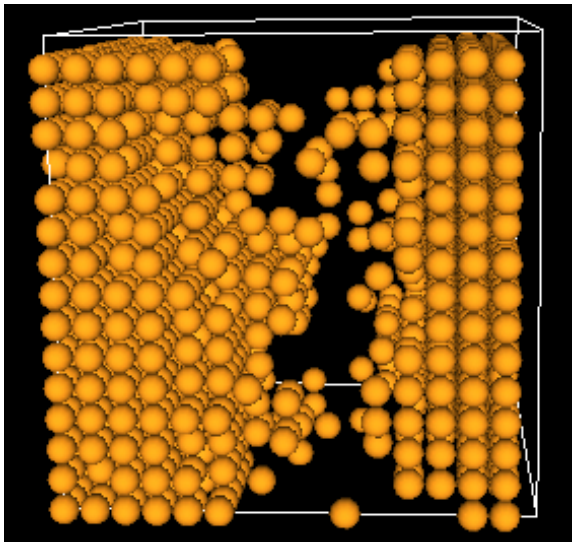

Figure 4.6: Example configuration from the middle peak of $P(\rho)$ at repulsion $A = 0.3$ attractive strength $\epsilon = 1.107$ and chemical potential $\mu = -3.249$. It shows a lamella like structure with two regions of high particle density separated by a region of lower density.

new peak is in the region of heterogeneity and hence that the Lifshitz point lies in the range $0.2 < A_L < 0.3$

4.4 Conclusions

In this section we compared the critical distributions for the HC2YF with that of the 3-dimensional Ising model as the repulsive strength A is increased. We saw that when $A = 0.0$ the Yukawa fluid critical distribution has good agreement with that of the 3D Ising model, but as the repulsion is increased to 0.15, 0.2 the Yukawa fluid moves further away from the Ising universality class and finally at $A = 0.3$, the simple fluid phase behaviour disappears entirely and a new peak appears in the distribution which corresponds to heterogeneous structures.

We also compared the progression of the density distributions as A increases with the 3D phase diagram proposed by AW for the HC2YF, and were able to deduce that the Lifshitz point - at which we see the onset of heterogeneity in the system behaviour - lies in the range $0.2 < A_L < 0.3$.

Now that we know at what point we start to see the formation of heterogeneous structures we can choose A such that $A \gg A_L$ so that the system behavioiur can

be investigated when heterogeneity is well established. To this end we choose to use $A = 1.0$ for the majority of this thesis.

Chapter 5

Delineating the Region of Heterogeneous States

5.1 Locating the Heterogeneous States

The topic of interest for this thesis is the region of the phase diagram at which the heterogeneous phases are easily accessible. With this in mind we choose to delineate the region of heterogeneous structures when the repulsion $A = 1.0$, well above the Lifshitz point. Figure 5.1 shows the average of the instantaneous particle density $\overline{\rho}$, as a function of the chemical potential μ, for attractive strengths $\epsilon = 2.3$, 2.5, 2.7 and 2.9 with attractive and repulsive lengthscales $z_1 = 2$ and $z_2 = 1$ respectively. For $\epsilon = 2.3$ one can see that $\overline{\rho}(\mu)$ is smooth. As ϵ increases, so do the gradients of the curves. Since the gradient gives the rate of change of $\overline{\rho}$ with respect to μ, a higher gradient means a greater sensitivity of $\overline{\rho}$ in μ. Hence the gradient of $\overline{\rho}(\mu)$ tells us the ease with which the system density can be increased - the compressibility - for a given ϵ, A, z_1 and z_2. For higher values of ϵ the mean density $\overline{\rho}$ no longer varies smoothly with μ but instead there are sections of the curves where the gradient (and hence the compressiblity) is high. A high compressibility means that it is easy for the system density to change rapidly between two values for a small change in μ. This implies the existence of two distinct states with different densities for a given μ. At $\epsilon = 3.2$ there is a single discontinuity between low and high densities, which is characteristic of a first-order phase transition.

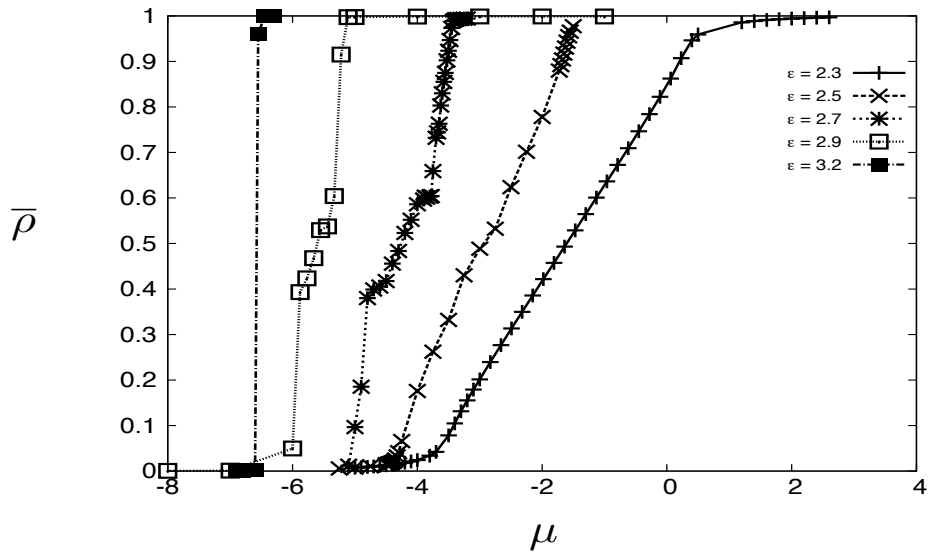

Figure 5.1: A plot of the mean system density $\overline{\rho}$, averaged over the course of a single simulation with randomised starting configuration, as a function of chemical potential μ. Lines indicate simulations with a common attractive strength $\epsilon = 2.3$, 2.5, 2.7, 2.9 and 3.2. The repulsive strength was held constant at $A = 1.0$ for all simulations shown, as were the attractive and repulsive lengthscales at $z_1 = 2$ and $z_2 = 1$ respectively.

One such kink is clearly visible at $\epsilon = 2.9$ near $\mu = -6.0$. Plotting the distribution of densities sampled $P(\rho)$ at $A = 1.0$, $\epsilon = 2.9$, $\mu = -5.91$ reveals a double-peak structure (figure 5.2). The lower density of the two peaks is taller and sharper and appears at a density of around $\rho = 0.002$. The higher density peak is shorter and broader, appearing in the range $0.03 < \rho < 0.1$. Between the two peaks is a valley with configurations that have low probabilities. The peaks themselves have equal statistical weight, which informs us that they have equal free energy. Figure 5.3 is a plot of the same distribution on a log scale. In this figure the scale of the relative probabilities of the two peaks and the valley between them is more clear. We can see that configurations with densities at the minimum have probabilites on the order of 10^5 times smaller than those at the maximum of the low density peak, indicating that there is a high free energy barrier between the gaseous and cluster configurations.

5.2 Clustering Behaviour

To understand what states are represented by the two peaks, we must look at the system configurations for various densities. Figure 5.4 demonstrates the types of configurations found in each of the two peaks. Configuration A shows a system at density $\rho = 0.0002$ and shows a low density (gaseous) state. Configurations B, C and D are at densities $\rho = 0.042$, 0.063 and 0.088 respectively. Each of these three configurations shows a system with a single, roughly symmetrical cluster, which grows in size as the system density increases. From these configurations we can determine that the low-density peak represents system configurations that are in a gaseous state and the higher density peak represents system configurations with a single symmetrical cluster. The clusters in configurations B, C, and D consist of 137, 202 and 287 particles respectively. The breadth of the high-density peak seems to be related to the range of cluster sizes, while the mid-point of the peak is related to the median cluster size.

Figure 5.5 shows a sample configuration at density $\rho = 0.025$ (inside the barrier between the two peaks), it contains a single cluster made of 75 particles. The

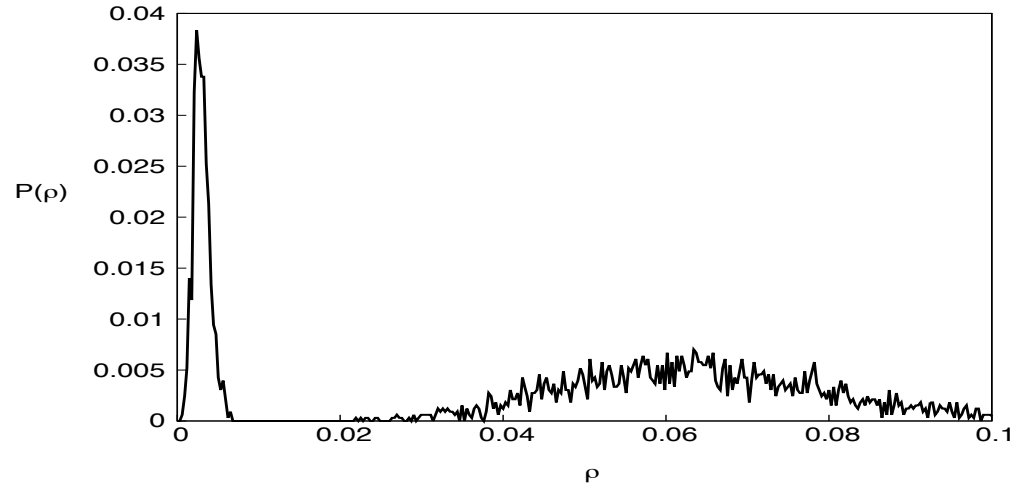

Figure 5.2: Distribution of densities sampled $P(\rho)$ in a simulation at $A = 1.0$, $\epsilon = 2.9$, $\mu = -5.91$, $z_1 = 2$ and $z_2 = 1$. The distribution has a double-peak structure with the taller, sharper peak at low densities and the shorter, broader peak at higher densities. The two peaks have roughly equal statistical weight. The separation between the two peaks indicates a high free energy barrier to transition between the two states.

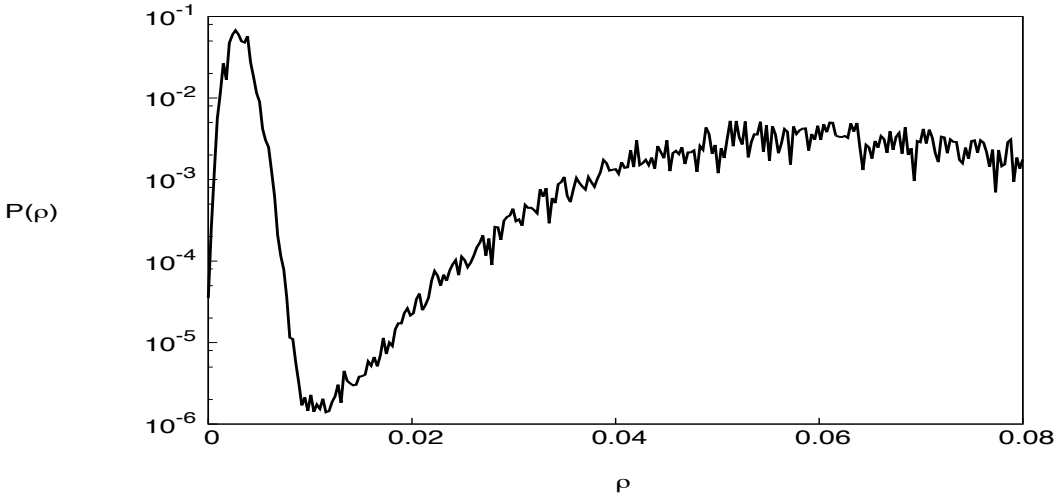

Figure 5.3: Distribution of densities sampled $P(\rho)$ from the same simulation as figure 5.2 at $A = 1.0$, $\epsilon = 2.9$, $\mu = -5.91$, $z_1 = 2$ and $z_2 = 1$. The distribution is plotted on a log scale to better show the height of the free-energy barrier to cluster formation.

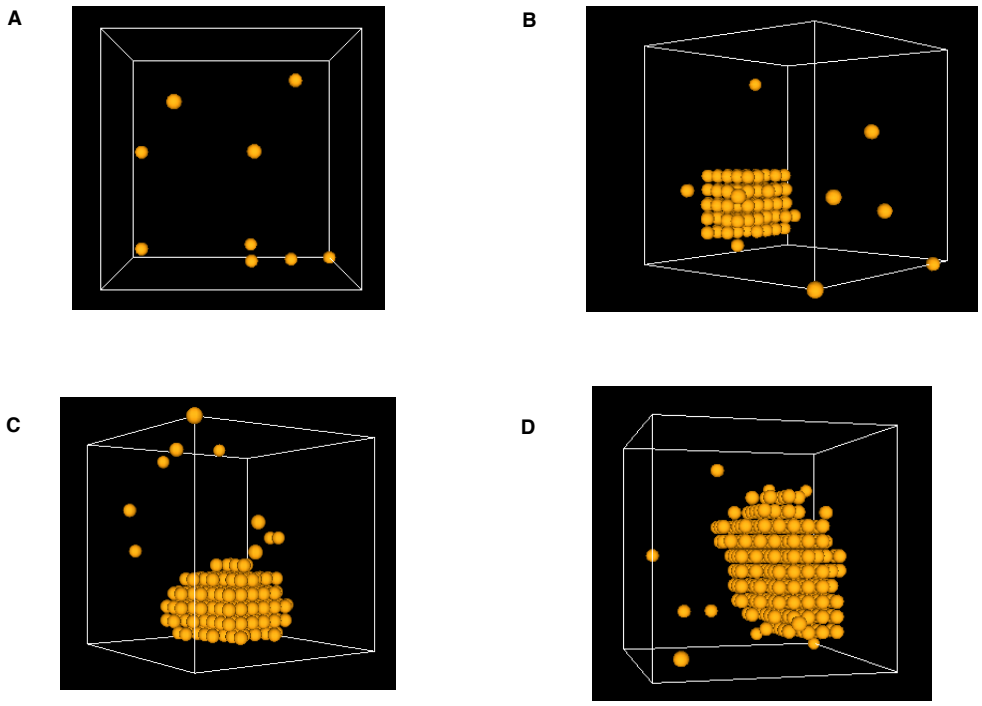

Figure 5.4: Example configurations from a simulation at $A = 1.0$, $\epsilon = 2.9$, $\mu = -5.91$, $z_1 = 2$ and $z_2 = 1$ found in the peaks of the distribution. The system densities for each configuration are A) $\rho = 0.002$, B) $\rho = 0.042$, C) $\rho = 0.063$ and D) $\rho = 0.088$. The clusters shown in configurations B, C, and D consist of 137, 202 and 287 particles respectively. Configuration A has no clusters.

probability of configurations with this density occuring is much lower than those inside the cluster peak, which means that there must be some sort of free energy barrier to cluster formation that needs to be overcome. To help explain why this may be the case, we can make use of Classical Nucleation Theory.

5.3 Classical Nucleation Theory

Cluster nucleation is the first step in the appearence of a new thermodynamic phase through the formation of a new structure via self assembly. Classical Nucleation Theory (CNT) describes the rate of nucelation (i.e. the rate at which nuclei form). According to CNT the free energy of a spherical nucleus contains two terms. The first is the bulk term and describes the stability of the nucleating phase relative to that of the surrounding phase. This term is proportional to the volume of the

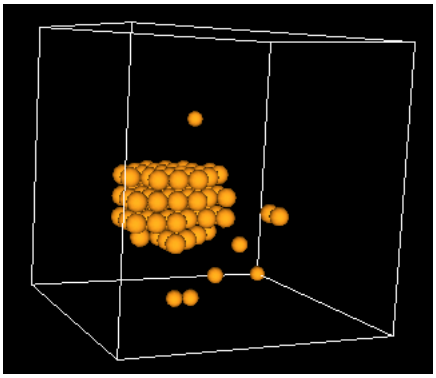

Figure 5.5: Example configuration from a simulation with $A = 1.0$, $\epsilon = 2.9$, $\mu = -5.91$, $z_1 = 2$ and $z_2 = 1$. This configuration shows a system at density $\rho = 0.025$, inside the barrier between the gas and cluster peaks. It shows a cluster consisting of 75 particles, which is smaller than those seen in the configurations from inside the cluster peak.

cluster. The second, surface tension term, describes the free energy cost associated with the creation of the interface between the two phases and is proportional to the surface area of the cluster [111].

Figure 5.6 contains a sketch of the function describing the free energy cost $\Delta\Omega$ associated with forming a cluster of radius R as predicted by CNT. CNT predicts that as R increases from zero, the surface tension term initially dominates and the free energy cost increases with R, forming a barrier to cluster nucleation. As the size of the cluster continues to grow, the contribution from the volume term grows faster than that from the surface area term and eventually comes to be the dominant term beyond $R = R_c$, with R_c some critical cluster size. For $R > R_c$, $\Delta\Omega$ begins to fall as the stability of the nucleating phase outweighs the cost of nucleation.

While CNT can help to explain the reason for a barrier to cluster formation in a system, there is a problem. CNT is used to describe the nucleation of thermodynamic phases and predicts that, once a nucleating phase reaches its critical size, it should continue to grow until it spans the entire system. This is at odds with the behaviour observed in our system which exhibits some stable cluster size beyond which there is a barrier to continued growth (see figs. 5.2 and 5.3). Figure 5.7 displays a similar sketch to that of figure 5.6, displaying the free energy cost $\Delta\Omega$ to cluster formation as expected based on the behaviour seen in figs. 5.2 and 5.3. Figure 5.7 shows $\Delta\Omega$ increasing with R as R grows from zero up to some maximum $\Delta\Omega_0$ at $R = R_c$ at which point the volume term overtakes the surface area term

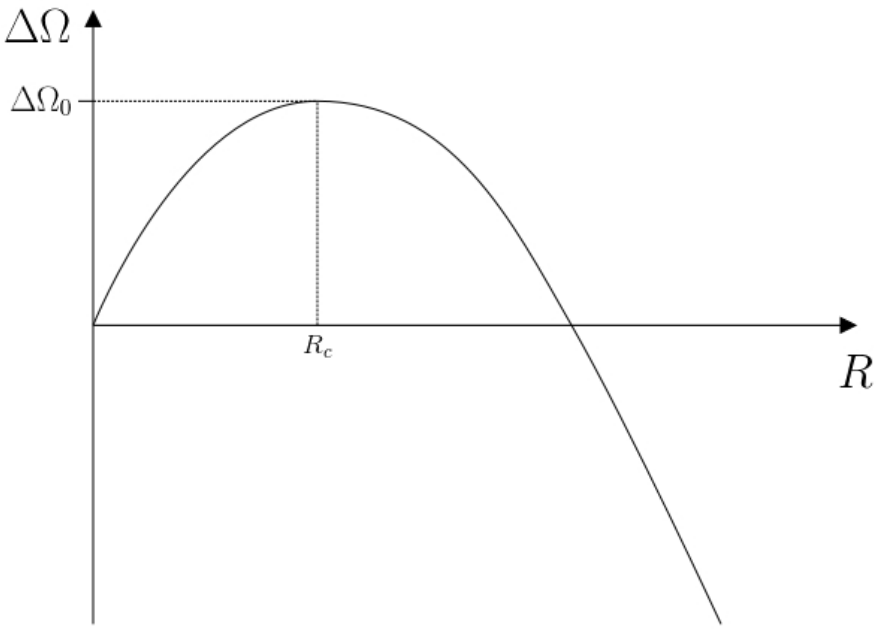

Figure 5.6: A sketch of the function describing the free energy cost $\Delta\Omega$ associated with forming a cluster of radius R as predicted by Classical Nucleation Theroy (CNT). CNT predicts that the free energy cost increases as R increases from zero as a result of the surface tension of the cluster, up to some maximum of $\Delta\Omega_0$ where $R = R_c$. Clusters of radius greater than R_c show a reduced free energy cost to formation as the energetic benefit of clustering overcomes the surface tension. Eventually the line crosses the horizontal axis and $\Delta\Omega$ becomes negative. This amounts to a prediction by CNT that, once a cluster overcomes the barrier to nucleation $\Delta\Omega_0$, it shall continue to grow indefinitely.

and becomes dominant. For $R > R_c$, $\Delta\Omega$ falls with increasing R as the cluster has overcome the initial barrier to nucleation. This barrier is represented by the valley between the two peaks in fig. 5.2. The higher density peak in fig. 5.2 indicates that clusters above a certain size become stable and this is represented by the line in fig. 5.7 crossing the horizontal axis as $\Delta\Omega$ becomes negative. Eventually however the high ρ peak in fig. 5.2 trails off as ρ increases, indicating the existence of a stable cluster size which is smaller than the system. This is likely caused by the contribution of the repulsive term in the interaction potential beginning to dominate as particles on opposite edges of the cluster start to repel one another. This implies the presence of a second turning pont in $\Delta\Omega(R)$ (shown in figure 5.7) at which point $\Delta\Omega$ again rises with increasing R, eventually becoming positive. The result is to prevent indefinite cluster growth by adding a third term due to the repulsive part of the potential introducing a second barrier to cluster growth and enforces a stable cluster size on our system.

5.4 Density as an Order Parameter

An order parameter is a variable which is allowed to vary over the course of a simulation and which is then used to obtain information about the current state of the system. It is becoming clear that in our system it is important to be able to distinguish the type of structures that the colloidal particles form. We should therefore choose an order parameter that is able to effectively distinguish between different structures such that we can tell the state of the system at any given point of time with relative ease. This is what we would call a "good" order parameter.

By taking snapshots of the system configuration (like those in figures 5.4 and 5.5) at regular intervals during a simulation and applying the cluster identification algorithm described in 3.3 to each of these snapshots, we can observe the evolution of cluster sizes over the course of the simulation. Figure 5.8 shows the volume fractions ϕ of the largest (solid line) and second largest (dashed line) clusters in the system as a function of simulation time t at $A = 1.0$, $\epsilon = 2.9$, $\mu = -5.91$, $z_1 = 2$ and $z_2 = 1$ (this data is taken from the same simulation as the plot of $\rho(t)$ in figure 3.8). By

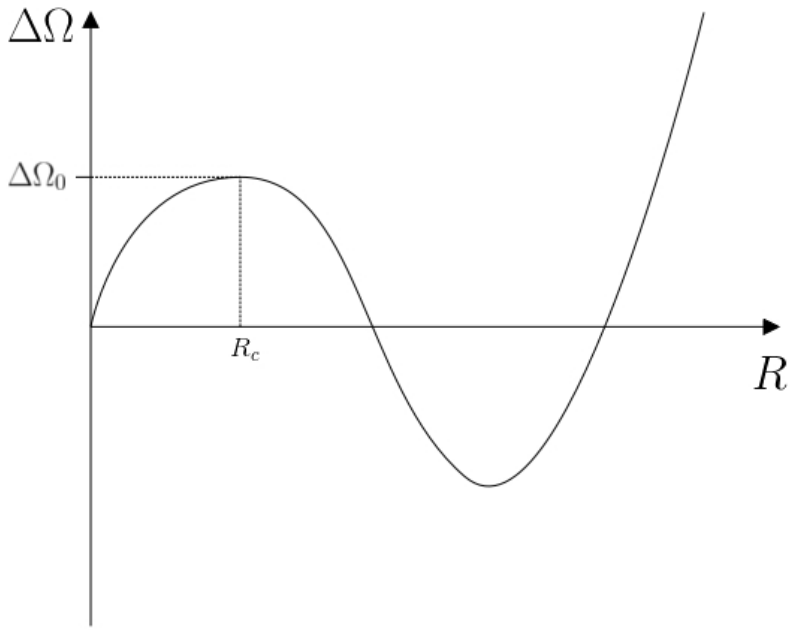

Figure 5.7: A sketch of the function describing the free energy cost $\Delta\Omega$ associated with forming a cluster of radius R in a cluster-forming SALR fluid, as expected based upon results from figs. 5.2 and 5.3. We expect that, as in Classical Nucleation Theory (CNT), the free energy cost increases as R increases from zero, again as a result of the surface tension of the cluster, up to some maximum $\Delta\Omega_0$ where $R = R_c$. Beyond this critical cluster size the cluster has overcome the barrier to nucleation and the free energy cost for continuiing to grow begins to fall. However, unlike in CNT, there is a second turning point at some $R > R_c$ caused by repulsion felt by particles across the cluster. Beyond this turning point the free energy cost to the cluster continuing to grow starts to rise and eventually becomes positive once more, preventing further cluster growth and enforcing some maximum cluster size on the system.

observing the sizes of the two larges clusters in the system, we are able to infer how the structures in the simulation change with time. Initially both clusters have sizes close to zero (the cluster identification algorithm ignores any clusters containing only a single particle). There are several times during the simulation when the largest cluster jumps from zero to non-zero size usually remaining there on the order of 10^5 Monte Carlo Sweeps (MCS) before dropping back to zero again. When the size is non-zero, the cluster's volume fraction ϕ ranges between 0.05 and 0.2. There are a few occasions when the second largest cluster also has a non-zero size, when this happens the second largest cluster's volume fraction behaves in the same way.

Using cluster sizes as an order parameter is the most direct method of obtaining information about how the system configuration varies over time, without inspecting each unique configuration by hand. However, the drawbacks of using this as our main order parameter are the difficulties in applying histogram reweighting and biasing to distributions of cluster size (which do not have a direct relationship to the system parameters), as well as the computational expense of gathering and analysing cluster size data compared with alternative order parameters. As a result, our next step is to compare the cluster size data in figure 5.8 to time series data for other variables from the same simulation to see how well those serve as order parameters for our system.

When we compare $\rho(t)$ and $E(t)$ from 5.9 with the cluster time series data from figure 5.8 we see that fluctuations in both E and ρ coincide with fluctuations in the sizes of the two largest clusters. For example, between $t = 3 \times 10^6$ MCS and $t = 4 \times 10^6$ MCS the jump in volume fraction of the largest cluster to $\phi \approx 0.2$ is reflected in a similar jump in the values of E to $\sim 3000 k_B T$ and ρ to ~ 0.2. Then later, when the volume fraction of the second cluster also jumps to $\phi \approx 0.2$, the values of E and ρ jump again to $\sim 5000 k_B T$ and ~ 0.4 respectively, roughly doubling in value. This suggests that the values of E and ρ are good indicators of the current state of the system, and that both make reasonable order parameters for our system.

Of the two observables, internal energy E and number density ρ, E is the less useful order parameter. This is because the internal energy of a system with given volume is dependent on the shape of the interaction potential, which is determined by the values chosen for A, ϵ, z_1 and z_2, as well as the number of particles in the

system (controlled by μ). Thus, two simulations of equal volume with different values of A, ϵ, z_1 and z_2 could form identical structures but have different values of E. On the other hand, ρ is only dependent on the number of particles in a system of given volume, so two systems with different interaction potentials but identical structures will have the same value of ρ. This makes direct comparisons between data from simulations with different interaction potentials simpler if we use ρ as our order parameter.

5.5 Mapping out the Gas-Cluster Line

Histogram reweighting, in combination with biased Monte Carlo, can be used to take the distribution at a point of equal free energy between two states to trace out the line of equal free energy between the two states on a phase diagram (see section 3.4.3 for a more detailed explanation). Using this technique to draw out the line of equal free energy between gaseous and cluster states results in the distributions shown in figure 5.10.

Figure 5.10 shows 5 density distributions when the gaseous and cluster states have equal free energy for $\epsilon = 2.55$, 2.60, 2.70, 2.80 and 2.90. Each of these distributions exhibits the same double peak structure as in figure 5.2, where the sharp peak at low density corresponds to the system in a gaseous state (configuration A in figure 5.4), while the second, broader peak indicates the existence of a cluster in the system (configurations B, C and D in figure 5.4). Starting from $\epsilon = 2.9$, as ϵ reduces, the mid point in the cluster peak moves to lower density and it becomes narrower. Hence the mean cluster size is smaller and there is less variation in the sizes of clusters. Also the gaseous peak moves to higher density as ϵ is reduced, and the valley separating the two becomes less deep. This tells us that the free energy barrier to cluster nucleation is lower and that the system density required for clusters to nucleate is higher.

The effect of the gas and cluster peaks moving closer together can be explained by recalling our discussion on Classical Nucleation Theory from section 5.3. CNT tells us that the free energy barrier to cluster nucleation is determined by the competing effects of the stability of the cluster relative to the gas (proportional to the cluster

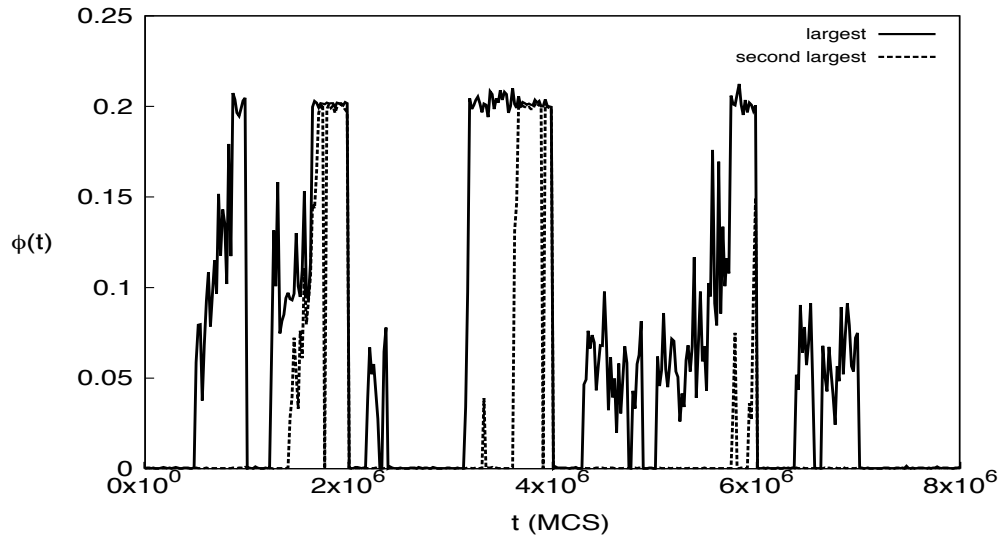

Figure 5.8: The volume fractions ϕ of the largest (solid line) and second largest (dashed line) clusters in the system, as a function of simulation time t for $A = 1.0$, $\epsilon = 2.9$ and $\mu = -5.91$.

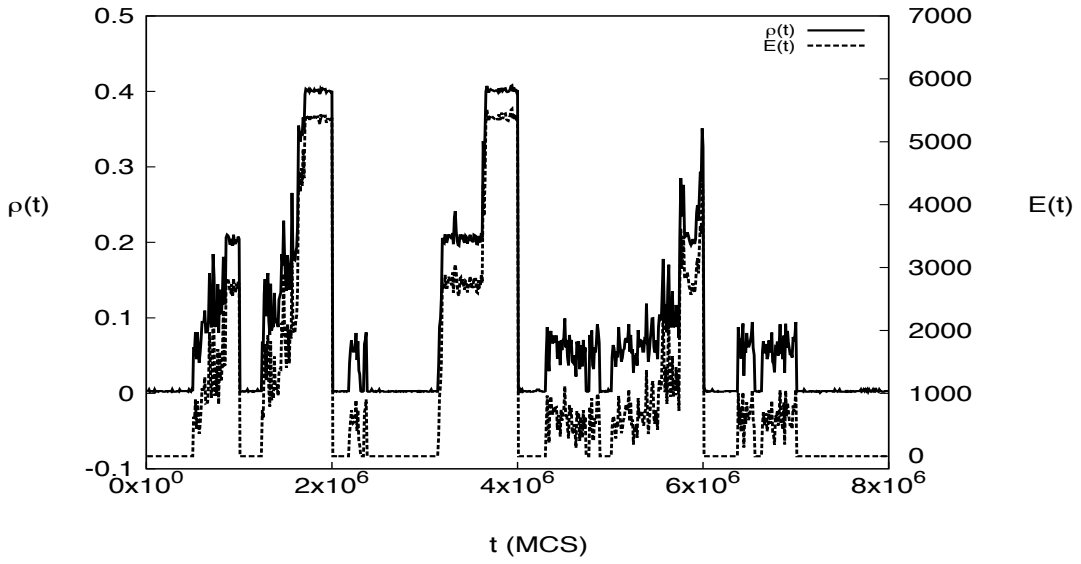

Figure 5.9: Comparison of $\rho(t)$ and $E(t)$ for the same simulation as figure 5.8 ($A = 1.0$, $\epsilon = 2.9$ and $\mu = -5.91$). The two functions have been offset from one another for clarity.

volume) which favours cluster formation, and the cost of forming the gas-cluster interface (proportional to the surface area of the cluster) which disfavours cluster formation. When ϵ is reduced, the cluster is made less stable by weakening the bonds between particles in the cluster, which reduces the contribution of the volume term. Since the critical cluster size R_c (the radius a cluster must achieve before it overcomes the barrier to nucleation) is inversely related to the volume term, the reduction in ϵ will act to cause R_c to increase, causing the gas peak to move to a higher density.

Meanwhile, the mean cluster size falls as ϵ is reduced since, for a weaker attractive strength, the effects of the repulsion felt by particles on opposite sides of the cluster through the cluster becomes dominant for smaller cluster sizes – lowering the limit on cluster size imposed by the long-range repulsion. As a result, the cluster peak moves to lower density.

Of course, the distributions in figure 5.10 are all taken from simulations with the same lattice size of 15^3 and so do not provide an indication as to the effects of finite system size. Given the periodic boundary conditions imposed on the system, we expect that there will be some repulsioon felt by particles on opposite sides of the cluster through the periodic boundaries, as well as through the cluster itself, amplifying the effects of the repulsion discussed in 5.3. If we were instead to consider the first cluster to form in an infinite system, we would still expect to see some finite stable cluster size, since particles would still feel repulsion through the cluster, but – as only repulsion felt through the cluster would contribute to the cost of continued cluster growth – it is reasonable to expect that the stable cluster size would be larger than for a finite system with periodic boundaries.

On the other side of the region of heterogeneity to the gas-cluster line, separating the heterogeneous structures from the homogeneous liquid phase, is the liquid-bubble line. Density distributions under conditions where the system spends equal time in the liquid and bubble states also have a double peak structure, reflecting that of the gas-cluster distributions for higher densities. In this case, the tall peaks at high density represent the homogeneous liquid, while the broader peaks at lower density represent the formation of symmetrical bubbles in the system. Unfortunately we are unable to show examples of these structures due to the bubbles being obscured by the surrounding liquid phase. Figure 5.11 shows 4 examples of distributions when the liquid and bubble states have free energy at $A = 1.0$, $z_1 = 2$ and $z_2 = 1$

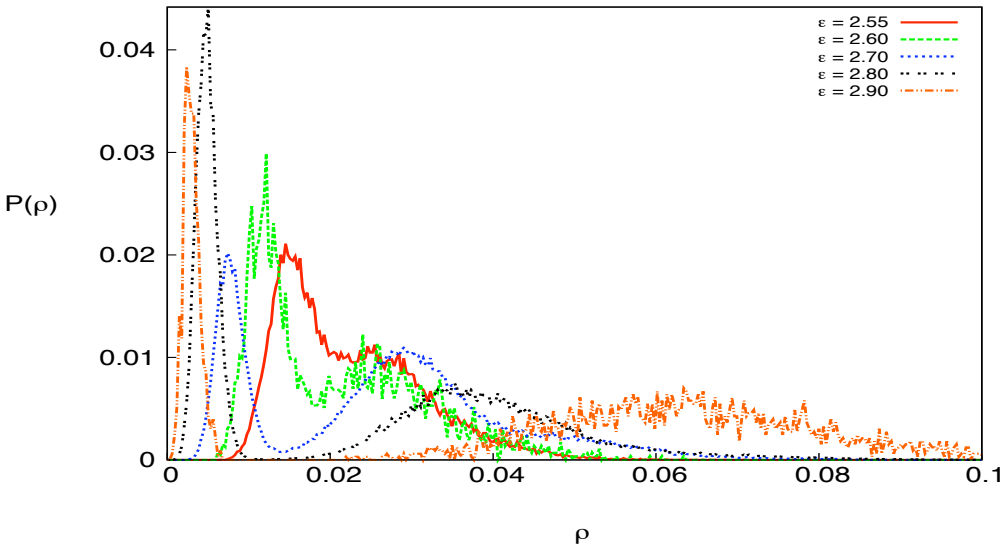

Figure 5.10: Distributions from simulation data along the gas-cluster line for $\epsilon = 2.55$ (red), 2.60 (green), 2.70 (blue), 2.80 (black) and 2.90 (orange).

when $\epsilon = 2.90$, 2.80, 2.70 and 2.60. From the similarities between the gas-cluster and liquid-bubble distributions, we can see that reducing the attractive strength ϵ reduces the mean and varience of the bubble size, while simultaneously reducing the free energy barrier to forming bubbles and reducing the critical bubble size. It is possible that there is a symmetry between the cluster formation in a homogeneous gas and bubble formation in a homogeneous liquid, but this would require direct measurement of the energy density of the interface and is outside the scope of this thesis.

In figure 5.12 the loci of points of gas-cluster and liquid-bubble equal free energies have been plotted in the ϵ-μ plane, delineating the region of inhomogeneous states for $A = 1.0$. Data is not shown for $\epsilon > 2.9$ as the simulations became very slow for larger values of ϵ. The diagram suggests that the lines of gas-cluster and liquid-bubble equiliria are moving towards some point of intersection at $\epsilon > 2.9$.

There are, unfortunately, fewer liquid - bubble distributions than there are gas - cluster distributions. This is due to the fact that the system has a much higher density at the liquid - bubble line, and hence simulations are much slower to run.

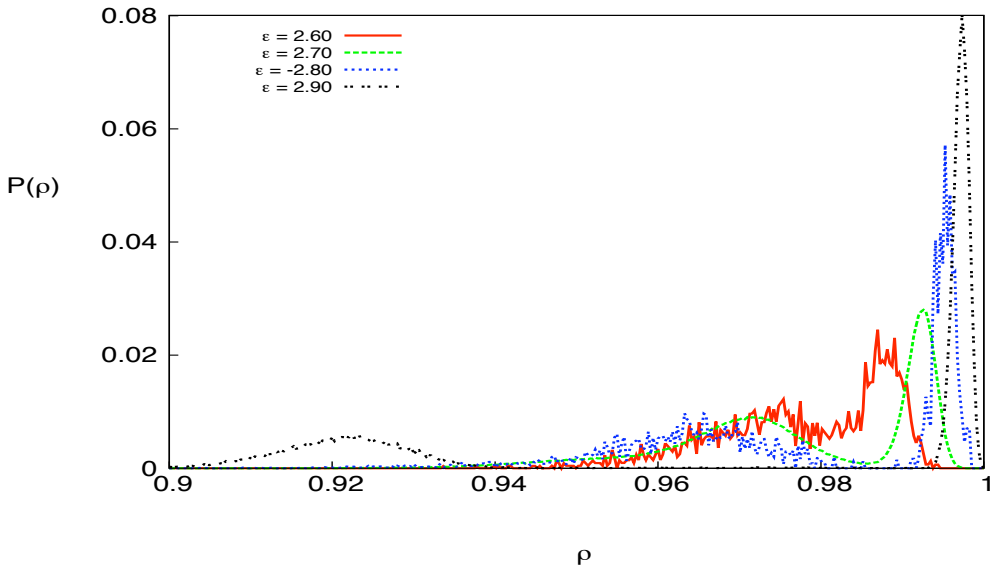

Figure 5.11: Distributions from simulation data showing the liquid and bubble states with equal free energy for $\epsilon = 2.90$ (black), 2.80 (blue), 2.70 (green) and 2.60 (red).

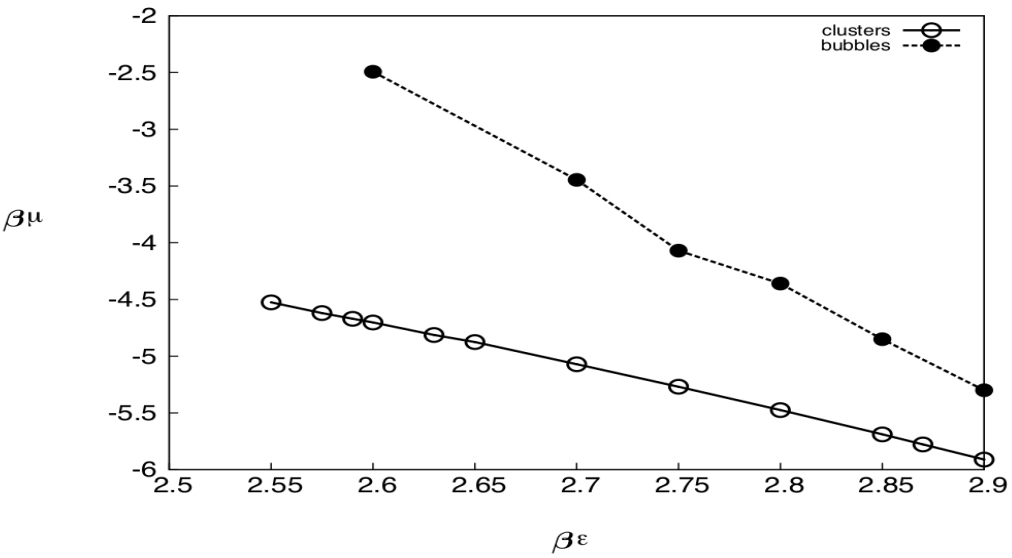

Figure 5.12: Locations of distributions corresponding to gas-cluster (empty circles) and liquid-bubble (filled circles) in the ϵ-μ plane. The lines serve as a guide for the eye.

5.6 Conclusion

In this chapter we have seen that the existence of heterogeneous states can be expressed in plots of $\overline{\rho}(\mu)$ by sections where the gradient is high (signifying high compressibility in the system). Plotting the density distribution $P(\rho)$ at these points in phase space reveals a double peaked structure, with a sharp peak at low density, a broader, lower peak at higher density and a deep valley between the two, indicative of a high free energy barrier between the two states. The distribution may be tuned so that both peaks have equal weight. It was then revealed that the low density peak corresponds to the system being in a homogeneous gas state, while the higher density peak corresponds to the appearence of clusters in the system. There also appears to be some relationship between the system density and the cluster size. Similar, mirrored, distributions, were seen at high density, with equal free energy between a homogeneous liquid state and a spherical void (bubble) state.

Looking at system configurations that appear in the barrier between the two peaks we see that they consist of smaller clusters. This drew our attention to Classical Nucleation Theory (CNT) to try to offer an explanation for the existence of the barrier. This lead to the conclusion that the turning point is due to there being some critical cluster size, beyond which the bulk term becomes dominant over the surface term in determining the free energy and so it becomes energetically favourable for the cluster to grow. However, CNT (which is used to explain nucleation events in first order phase transitions) predicts that the cluster should grow indefinitely, which does not appear to be the case for our system.

The apparent relationship between the system density and the cluster size raises the question of order parameters. A good order parameter is an observable which is able to distinguish between different states in the system. By comparing the time series of the internal system energy $E(t)$ and system density $\rho(t)$ with the sizes of the largest and second largest clusters in the system (ϕ_1 and ϕ_2 respectively), we were able to show that both E and ρ could effectively distinguish between the gaseous and cluster states. We chose the system density ρ as our order parameter since it makes for easy comparisons between systems with different parameters, which could have different internal energies despite being in the same state.

Having decided that density is a good order parameter for our system, we then

performed histogram reweighting on the density distributions where the gas and cluster states had equal free energy, in order to map out the gas-cluster line.

Chapter 6

High Attractive Strength

6.1 Introduction: Hysteresis At High Attractive Strength

In chapter 5 we saw that the mean density as a function of the chemical potential $\overline{\rho}(\mu)$ shows a sharp discontinuity at attractive strength $\epsilon = 3.2$, when the value of $\overline{\rho}$ jumps from ~ 0 (homogeneous gas) to ~ 1 (homogeneous liquid) (figure 5.1). This suggests the presence of a first order gas - liquid phase transition. Figure 6.1 shows two plots of $\overline{\rho}(\mu)$, both at $A = 1.0$ and $\epsilon = 3.2$. Each point on both lines represents an independent simulation. The points on the solid line represent simulations that were started with initial density $\rho = 0.0$ (gas), while the points on the dotted line represent simulations that were started with initial density $\rho = 1.0$ (liquid). Both lines show a phase transition, but the value of μ at which the phase transition occurs is dependent on the initial conditions of the simulation. This dependency of the apparent location of the phase transition on initial conditions is called hysteresis and is a common feature of first order phase transitions.

There is a value of μ for which both phases are equally stable (i.e. have the same free energy). This is called "phase coexistence". If a simulation were run for a sufficiently long time at coexistence we would expect to see the system spend an equal amount of time in both phases (since the system has an equal probability of being in either one) and the mean density $\overline{\rho}$ to be the average of the densities of the coexisting phases (0.5 in the case of gas - liquid coexistence in a lattice system).

Away from this value of μ, one phase will be more energetically favourable than the other, and we would expect the probability of each phase to be related to their respective free energies by $\beta F(\rho) = -\ln P(\rho)$, with $F(\rho)$ and $P(\rho)$ the free energy and probability respectively of a system configuration with given density ρ (see section 1 for more detail).

Hysteresis occurs when the probability of transitions occuring is very low (the free energy barrier to transition is high), and hence transitions occur only rarely. This means that if a simulated system in the vicinity of – but not at – phase coexistence is initially in the less energetically favourable phase, the time scale for the transition into the more favourable phase may be large relative to the time scale of the simulation itself. The result is a blurring of the point of phase coexistance as simulations which are above the phase transition still appear to be below it, and vice versa. This effect makes it difficult to obtain an accurate estimate for the location of phase coexistence. Fortunately, by artificially flattening the barrier to phase transition and hence increasing the frequency with which transitions may occur, biased Monte Carlo can help us to overcome this problem (see section 3.4).

6.2 Density distributions Below the Bifurcation Point

Transition matrix Monte Carlo (see section 3.5) is a form of biased Monte Carlo which generates a transition matrix containing the relative probabilities of the system densities as the simulation runs. The transition matrix is used to periodically generate a new preweight function for the simulation, with each iteration producing an increasingly accurate estimate for the density distribution. By generating preweight functions iteratively, transition matrix Monte Carlo plumbs the depths of $P(\rho)$ and can deal with rough free energy landscapes.

It can be seen from figure 6.1 that the gas-liquid phase transition occurs at roughly $\mu = -7.5$ for $A = 1.0$ and $\epsilon = 3.2$, since that is the mid point between the discontinuities of the two curves. Making use of transition matrix Monte Carlo we were able to obtain an estimate for the density distribution at $A = 1.0$, $\epsilon = 3.2$ and $\mu = -7.55$, plotted on a logarithmic scale in figure 6.2.

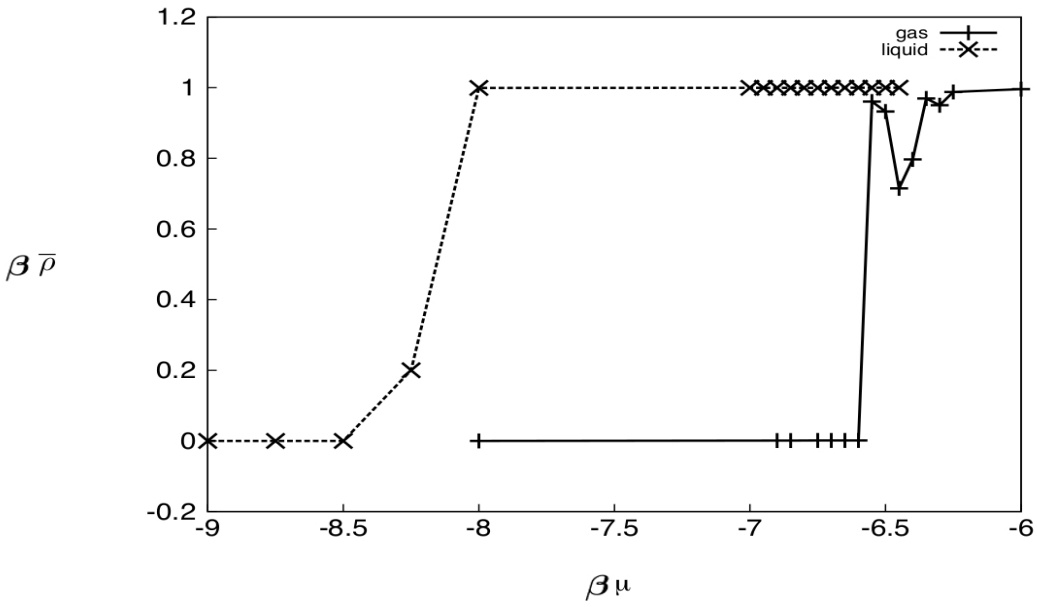

Figure 6.1: Plot of the mean density $\overline{\rho}$ as a function of chemical potential μ for multiple independent simulations initialised in either the gas phase (solid line) or the liquid phase (dashed line), averaged over the entire simulation. The simulations were run with values of repulsive strength $A = 1.0$, attractive strength $\epsilon = 3.2$, system length $l = 15$ and attractive and repulsive lengthscales $z_1 = 2$ and $z_2 = 1$ respectively. Each point represents the result from a single simulation. This figure is a repeat of figure 3.5

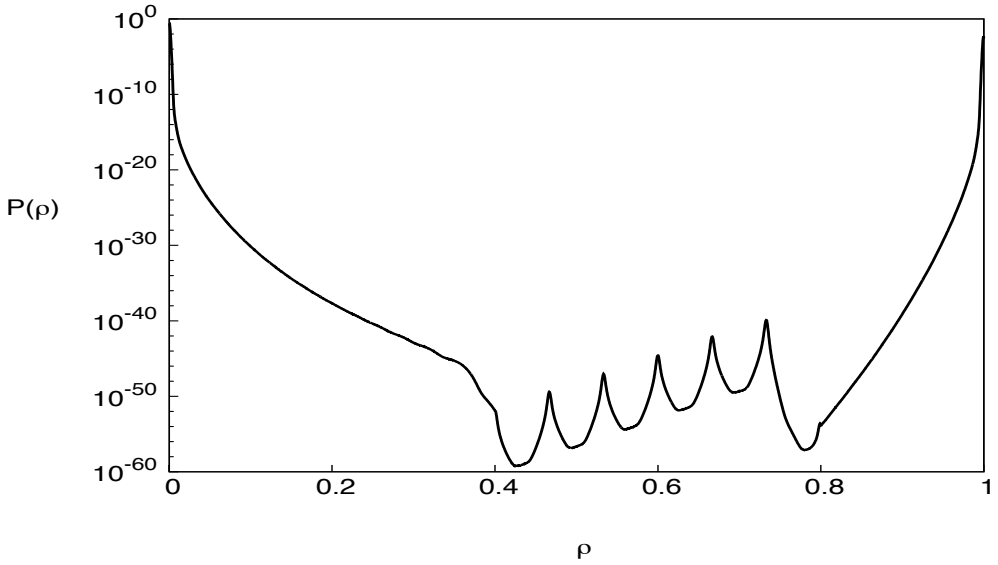

Figure 6.2: A density distribution $A = 1.0$, $\epsilon = 3.2$, $\mu = -7.55$ for a system size of $l = 15$, plotted on a log scale. The distribution shows a series of regularly spaced peaks in the range $0.4 < \rho < 0.8$. These peaks have probabilities on the order of 10^{-50}. There is also a shoulder at $\rho \approx 0.35$.

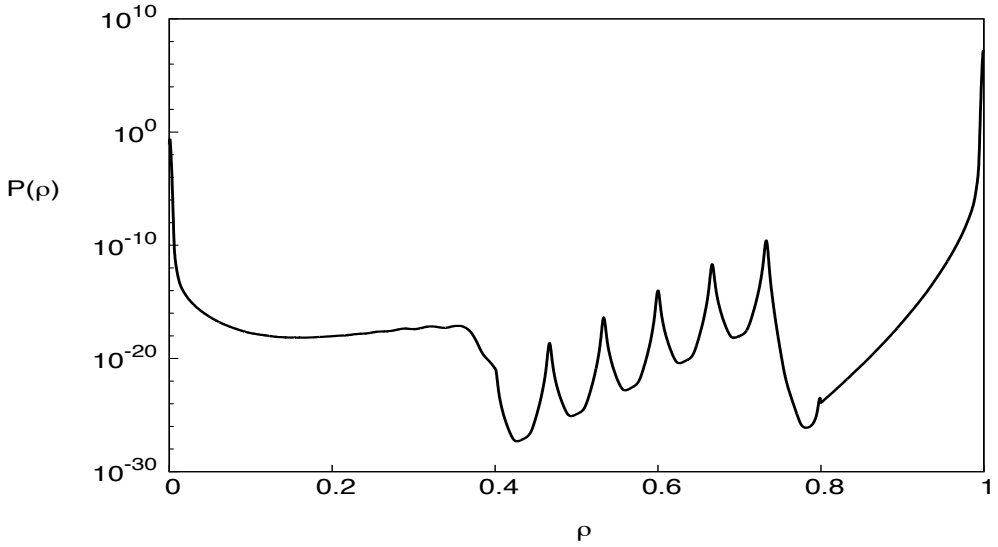

Figure 6.3: A density distrbution for $A = 1.0$, $\epsilon = 3.15$, $\mu = -7.22$, $l = 15$, plotted on a log scale. The central peaks now have probabilities on the order of 10^{-20} and the shoulder at $\rho \approx 0.35$ is more pronounced.

Figure 6.2 has two strong peaks with equal statistical weight. These peaks are at $\rho = 0.0$ and $\rho = 1.0$ and correspond to the liquid and gas peaks (that is not to say that the system is empty when in the gas phase, merely that the density is so low that the average number of particles present in a volume equal to that of the simulation size is less than 1). This is as one would expecct for a gas-liquid first order phase transition. What is interesting and unusual is the structure in the density distributions at intermediate densities which is only visible on a logarithmic scale. In the range of $0.4 < \rho < 0.8$ we can see that there is a series of regular peaks in the regime of low probability. Using transition matrix Monte Carlo in combination with histogram reweighting we were able to obtain other density distributions close to the line of phase coexistence (see section 3.4.3). Figures 6.3, 6.4 and 6.5 show the density distributions at $\epsilon = 3.15$, 3.125 and 3.1 respectively. So as to facilitate the ease of comparison, the distributions were normalised such that the mean of the heights of the gas and liquid peaks are equal to unity.

Figures 6.2 to 6.5 reveal how the density distribution changes as the attractive strength is reduced from $\epsilon = 3.2$ to 3.1. In each of these distributions there is a gas and liquid peak with probabilities on the order of unity and five peaks in the range $0.4 < \rho < 0.8$. At $\epsilon = 3.2$ these intermediate peaks have probabilities on the order of about 10^{-50}, far below the probabilities of the gas or liquid peaks. There is also what may be a shoulder at $\rho \approx 0.35$. At $\epsilon = 3.15$ the intermediate peaks have probabilities on the order of 10^{-10} (a difference of 40 orders of magnitude relative to the distribution at $\epsilon = 3.2$) and the shoulder at $\rho \approx 0.35$ is more pronounced. At $\epsilon = 3.125$ the intermediate peaks have probabilities on the order of 10^{-5}, still lower than the homogeneous phases, and the shoulder at $\rho \approx 0.35$ has now grown into a peak. Finally at $\epsilon = 3.1$ all 5 peaks in the range $0.4 < \rho < 0.8$ and the peak at $\rho \approx 0.35$ have probabilities on the order of 10^{5}, higher than the probabilities of the homogeneous gas and homogeneous liquid peaks.

In the next section we shall look at the kinds of configurations that occur when the system is under each of these peaks.

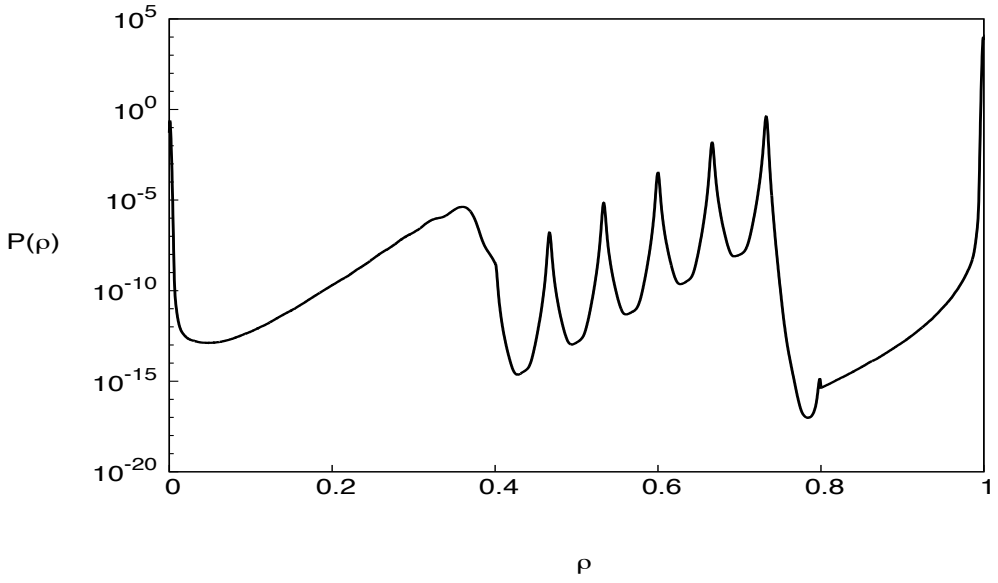

Figure 6.4: A density distribution for $A = 1.0$, $\epsilon = 3.125$, $\mu = -7.06$, $l = 15$, plotted on a log scale. For this value of ϵ, the central peaks have probabilities on the order of 10^{-5}. The shoulder at $\rho \approx 0.35$ has now become a peak.

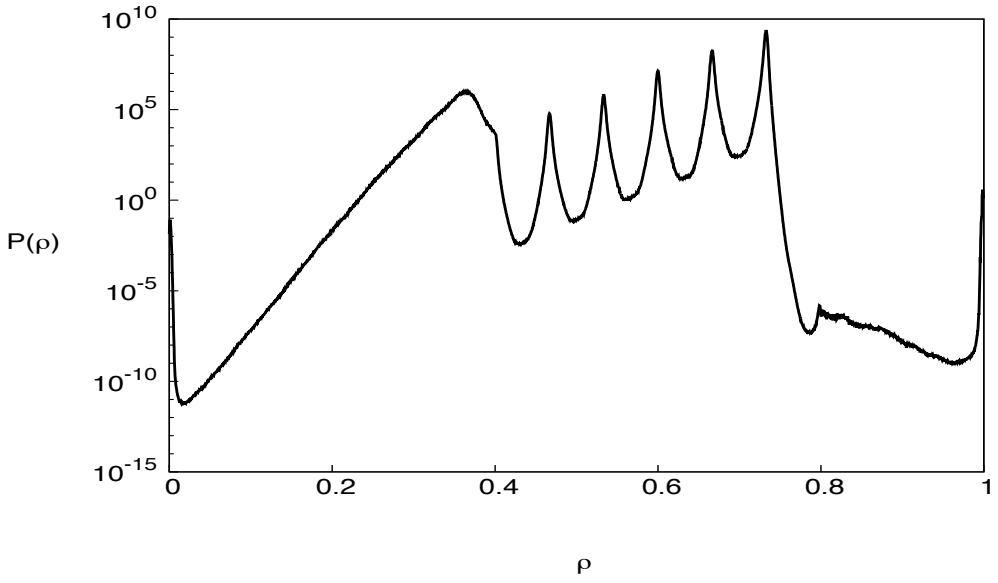

Figure 6.5: A density distribution for $A = 1.0$, $\epsilon = 3.1$, $\mu = -6.9$, $l = 15$, plotted on a log scale. Now the central peaks (in addition to the new peak at $\rho \approx 0.35$) have probabilities on the order of 10^5, which is larger than that of the gas or liquid peaks.

6.3 Configurations in the Barrier

As in chapter 5, we can use snapshots of system configurations to investigate the types of structures that form under different features of the density distribution. The density distribution gives an indication of the free energy of the system for a given value of the system density. It is the free energy (the total potential for the system to do work) that determines the relative probabilities of different states, of which the internal energy of the system is only one contributing factor. However, when the interparticle potential is high (as is the case here), the system's internal energy becomes the dominant term in the free energy. Hence, when trying to understand why the system forms into various structures, it is reasonable for us to use arguments centered on the internal energy to explain the differences in their relative stability.

Figure 6.6 shows a portion of the density distribution near gas - liquid coexistence for $A = 1.0$, $\epsilon = 3.125$, $\mu = -7.06$ in the range $0.0 < \rho < 0.4$. The distribution contains a sharp gas peak at $\rho = 0.0$ and a broader peak at $\rho \approx 0.35$. Below the density distribution there is a set of system configurations, labelled according to where they are seen on the distribution.

There are three main features to the section of the density distribution shown in figure 6.6. There are two peaks at $\rho = 0.0$ (gas peak) and $\rho \approx 0.35$ and a valley between the two peaks at $\rho \approx 0.05$. Starting off in the gas phase, clusters start to nucleate as the system density increases. As discussed in sections 5.3 and 5.5, the valley between the two peaks at $\rho \approx 0.05$ is caused by the existence of a barrier to cluster nucleation. Configuration A in fig. 6.6, taken from a system at $\rho = 0.05$ shows a small cluster has nucleated. As ρ increases the cluster can be seen to grow in size through configurations B, C and D. $p(\rho)$ also increases with ρ for $\rho > 0.05$, demonstrating the tendency for the cluster to grow once it has overcome the initial barrier to nucleation at A. Once the cluster has grown beyond a certain size, the particles on opposing sides of the cluster will start to repel one another through the cluster. As the cluster continues to grow, the repulsion felt by the outermost layer of particles will increase. With the effect of the repulsion growing, each new particle aggregating onto the sureface of the cluster will position itself in such a way as to minimise the number of neighbours which it is repelled by, with the effect of minimising the overall internal energy of the cluster. The cluster geometry that is

most effective at minimising total internal energy is an asymmetric cluster, which is elongated along one axis. Hence we see that in our system the cluster forms a cuboidal shape as shown in cofiguration C. As it continues to grow along one axis, the cluster eventually spans the entire system (configuration D). The preference of clusters to adopt asymmetric geometries bears some similarity with the theoretical predictions of Groenewold and Kegel [83].

Figure 6.7 shows a section of the density distribution in the range $0.37 < \rho < 0.48$, continuing from the distribution shown in figure 6.6. Between configurations D and E we see that the cluster has started to grow along a new axis, forming a lamella that spans the system in two dimensions. The reason for this in a finite size system with periodic boundaries, is that there is simply no more room for the cluster to continue to grow along the original axis of growth, as the cluster in configuration A now spans the periodic boundary of the system. But this is an unsatisfactory explanation for the occurrence of lamellae in an infinite system, so instead we shall consider qualitatively what happens if the cluster is permitted to grow along one axis indefinitely, without any spatial constraints.

In the case of the first cluster to form in an infinite system, as the cluster continues to grow along one axis it will become increasingly asymmetrical, making the entropy of particles on the ends much lower than on the longer sides of the cluster. This will introduce a free energy barrier to adding particles to the ends of the cluster which, once the cluster shape has reached some asymmetry limit, will surpass the barrier to adding clusters to the long sides in height. Past this point, new particles will become more likely to aggregate on one of the longer sides than at the ends, despite the fact that it is less favourable in terms of the internal energy of the cluster to do so. Since the cluster will still want to maintain some asymmetry in order to minimise it's internal energy, growth along a single axis is still desired. Thus the geometry of the cluster changes from rod-like to slab like and the system forms a lamella such as that shown in configuration E.

Figure 6.8 shows a section of the density distribution for $A = 1.0$, $\epsilon = 3.2$, $\mu = -7.55$ in the range $0.4 < \rho < 0.85$. In this section there is a series of peaks and troughs at regular intervals. Configurations H, I and J show example snapshots of the system in two adjacent peaks and the barrier between them. This reveals some information about the underlying Physics that causes the peak structure. All three

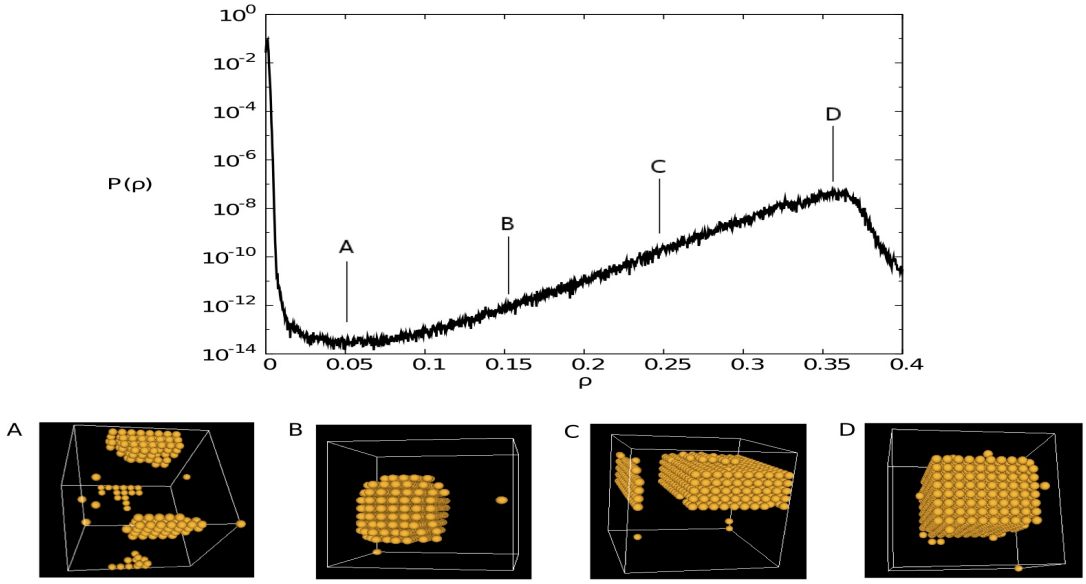

Figure 6.6: System configurations for $A = 1.0$, $\epsilon = 3.125$, $\mu = -7.06$, $l = 15$, at various points on the density distribution in the range $0.0 < \rho < 0.4$. This figure demonstrates how the clusters become elongated as the system density rises.

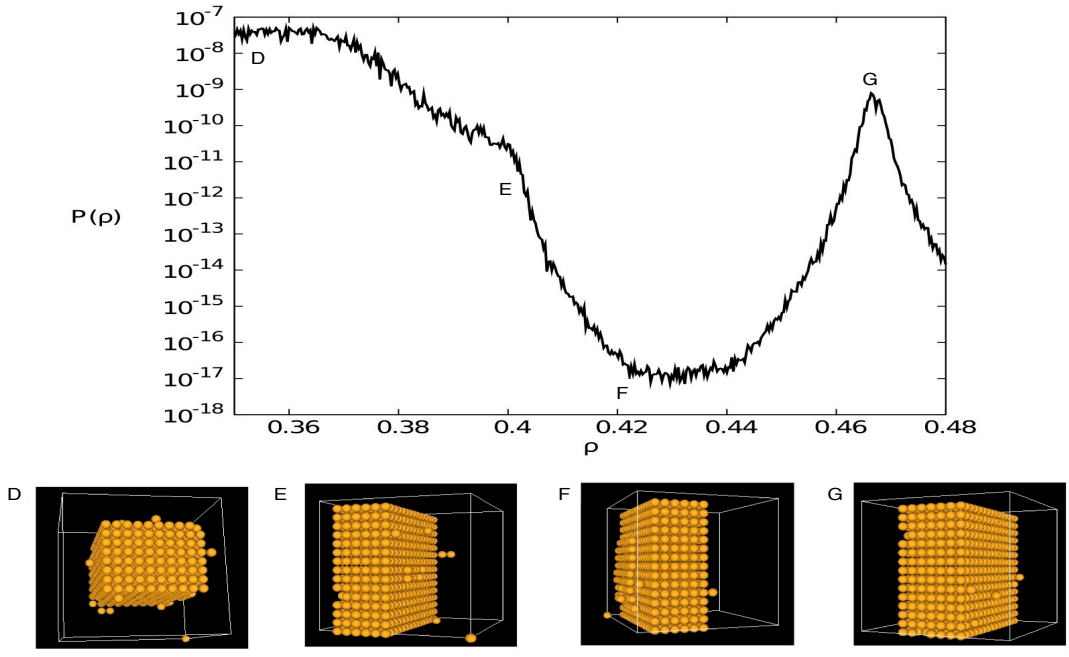

Figure 6.7: System configurations for $A = 1.0$, $\epsilon = 3.125$, $\mu = -7.06$, $l = 15$, at various points on the density distribution in the range $0.35 < \rho < 0.48$. This figure demonstrates how the elongated cluster extends along a new axis to become a lamella.

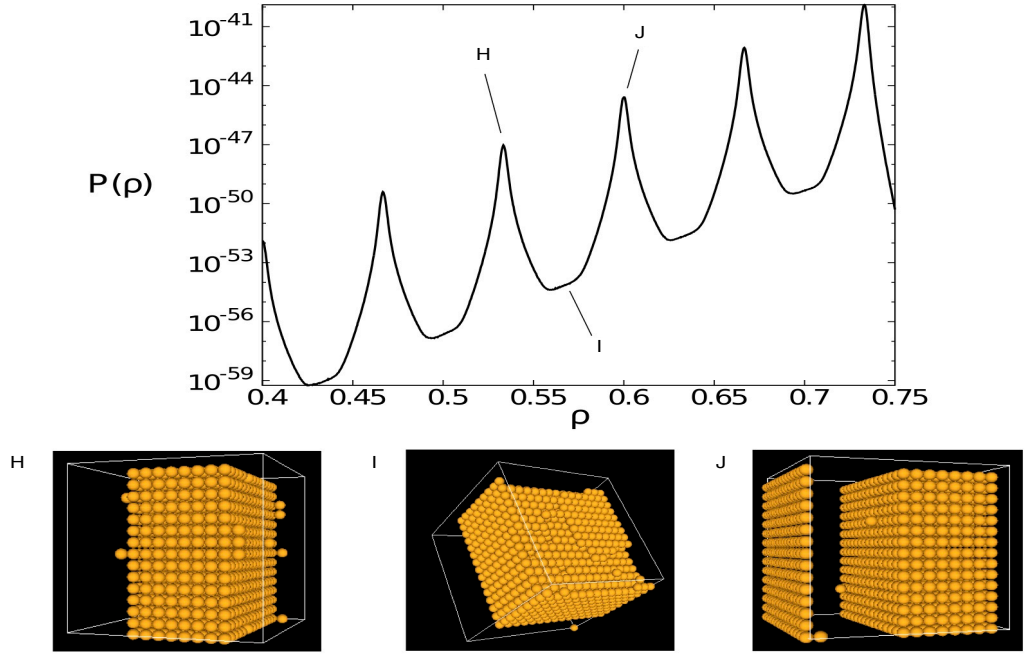

Figure 6.8: System configurations for $A = 1.0$, $\epsilon = 3.2$, $\mu = -7.55$, $l = 15$, in the range $0.4 < \rho < 0.75$. Each successive peak corresponds to a lamella with increasing number of layers (configurations H and J). In the valley between them (configuration I) we see that the lamella has a partially completed layer.

of these configurations show lamella structures, slabs made up of layers of particles that span the system in two dimensions. The lamella in configuration H has 8 layers of particles, while the lamella in configuration J has 9. The lamella in configuration I also has 8 layers, but in addition there is a partially complete layer of particles visible on the surface of the structure. This implies that the transition from H to J involves some kind of layer aggregation process. If the growth of new layers on the surface of a lamella can be shown to be energetically unfavourable until some critical number of particles have aggregated then this could help to explain the origin of the regular peak structure seen in the density distribution.

6.4 Potential Energy of Lamella Surface Aggregation

To better understand the process by which new layers aggregate on lamellar structures, we can measure how the total internal energy of the system (minus the energy from the chemical potential μN) changes as we manually add particles to the new

layer. Figures 6.9 and 6.10 show the change in the internal energy due to the particle interactions only ($U - \mu N$) as a function of the number of particles added to the new layer of the lamella. After 225 insertions the new layer is complete. Both of these figures are for lamellea with eight layers, but the method of particle insertion is different.

In figure 6.9 particle insertions were made in a spiral pattern on the surface of the lamella. The first insertion is made at a random site on the surface of the lamella and subsequent insertions are made in concentric rings around this initial particle. The curve in figure 6.9 shows that the cost to the internal energy of the system starts off negative. As more particles are inserted on the surface of the lamella the curve has a series of steps showing a climbing cost to insertions. Each step corresponds to consecutive rings of inserted particles, hence each step is longer than the previous one. The step structure tells us that every particle in a given ring has roughly the same potential energy. As the aggregating layer grows, the number of repulsive neighbours for particles in each new ring increases, hence each step in the curve has a higher cost than the previous one. Eventually the number of particles in the aggregating layer reaches some critical value beyond which it becomes favourable to add more particles to the layer, as shown by the turning point at around 200 inserted particles. This happens in our system when the aggregating layer starts to span the system and so new aggregating particles start to feel attraction from other particles in the aggregating layer through the periodic boundaries. In an infinite system we would expect groups of particles to aggregate at regularly spaced locations. These will grow until they eventually merge, creating a similar effect to the periodic boundaries in a finite system.

Figure 6.10 shows how the potential energy of the system changes as particles are inserted in a new layer in a typrwriter fashion, by inserting particles in a line until a row in the lattice is full before moving on to the adjacent row. This continues until the new layer is complete. The first few particles in the first row are strongly favourable, but subsequent particles bacome less favrourable as the number of repulsive neighbours grows. The penultimate particle in the first row corresponds to the first peak in the curve, since the final particle in the row has one more attractive neighbour than the others. Every particle in each subsequent row also has more attractive neigbours than the first row. The final particle in each row has one additional attractive neighbour, hence the regularly spaced downward spikes on the

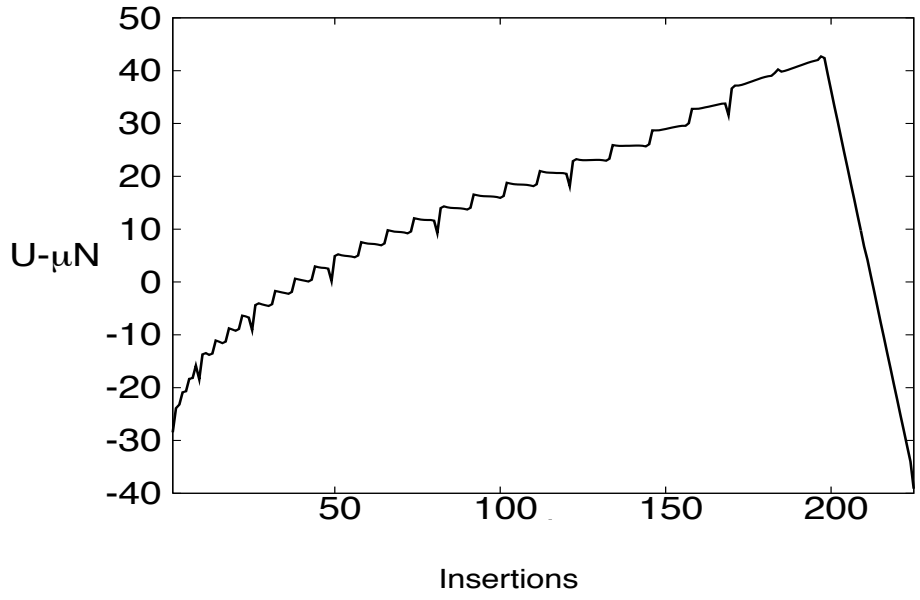

Figure 6.9: A plot of potential energy as a function of number of particles inserted on the surface of a lamella with 8 layers in a system with $A = 1.0$ $\epsilon = 3.2$ $l = 15$ (excluding the effect of the chemical potential on the system). The particles are inserted in a spiral pattern centered on the first particle in the new layer.

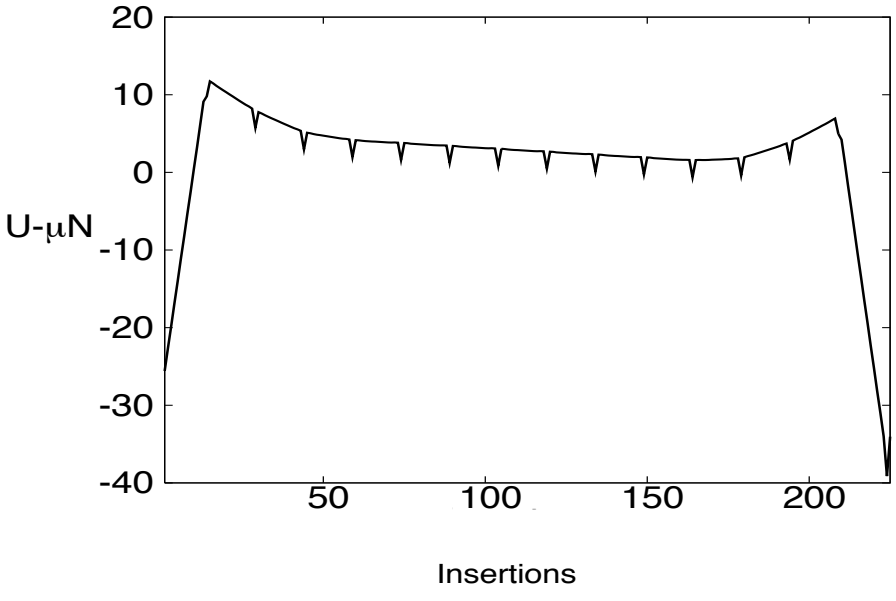

Figure 6.10: A plot of potential energy as a function of number of particles inserted on the surface of a lamella with 8 layers in a system with $A = 1.0$ $\epsilon = 3.2$ $l = 15$ (excluding the effect of the chemical potential on the system). The particles are inserted in a typewriter fashion.

curve punctuate the completion of each row. There is an upward turn in the curve for the few rows before the final row completes the new layer. This indicates that particles in these rows are starting to feel repulsion form the first few rows through the periodic boundary. The final row is much more favourable to insert, since these particles feel more attraction than previoius particles insertions, as illustrated by the sharp drop in energy cost at the end of the curve.

The two insertion methods highlighted in figures 6.9 and 6.10 differ considerably in how they affect the internal energy of the system, although both predict a turning point in the energy cost of inserting particles into the new layer. Configuration I in figure 6.8 shows that the particles in the new layer have formed into a square pattern. This give us a hint that the spiral insertion method is the more physical, since it would create patterns similar to those seen in the simulations.

6.4.1 Locating the bifurcation point

Previously we have seen that the heterogeneous structures are stable relative to the gas and liquid phases for lower values of ϵ and that generally only one or two peaks are visible for a given chemical potential μ. We define the gas-cluster and liquid-bubble lines as the lines of chemical potentials for which peaks in the gas-cluster and liquid-bubble distributions have equal weight for given ϵ. As ϵ increases the two lines move closer to one another in the $\epsilon - \mu$ plane, eventually converging at the bifurcation point. When the value of ϵ is increased beyond the bifurcation point the heterogeneous structures become metastable relative to the gas and liquid states, as seen in figures 6.2, 6.3, 6.4 and 6.5. Hence it seems that a reasonable definition of the bifurcation point for a given value of A is the highest value of ϵ for which peaks representing the heterogeneous structures are visible when the density distribution is plotted on a linear scale. Going by this definition we can use figures 6.2, 6.3, 6.4 and 6.5 to obtain an estimate for the location of the bifurcation point when $A = 1.0$.

Looking at these figures we see that the heterogeneous structures are not quite stable relative to the gas and liquid peaks when $\epsilon = 3.125$ (figure 6.4) and when $\epsilon = 3.1$ (figure 6.5) they are. This leads us to estimate that the bifurcation point is at $\epsilon = 3.1125 \pm 0.0125$ when $A = 1.0$.

6.5 Finite Size Behaviour

The structures described in section 6.3 occur in ranges where the density distribution functions are in the low probability regime. To determine if this metastability is real, or if it is some artefact of the finite system size, we should consider the high-ϵ case for different system sizes.

Figures 6.11, 6.12 and 6.13 contain density distributions at $l = 12$ for $\epsilon = 3.3$, 3.2, and 3.1 respectively. Comparison between these density distributions and those in figures 6.2, 6.3, 6.4 and 6.5 for $l = 15$ shows a number of similarities and differences between the two system sizes. Density distributions for both system sizes have the regular peaks and troughs in the mid-range densities. Figure 6.14 shows that each successive peak for $l = 12$ represents a lamella with one more layer of particles than the previous peak, while the barrier consists of partially completed layers. This is similar to the behaviour seen in section 6.3 for $l = 15$, so it is safe to conclude that the process of layer aggregation is common to both system sizes.

A discernible difference between the two system sizes is the lack of a broad peak at $\rho = 0.35$ in the $l = 12$ density distributions, when compared with the $l = 15$ density distribution. Instead at $l = 12$ the region of regular peaks and troughs is extended, with an additional sharp peak at $\rho = 0.35$ and a deep barrier followed by a sharp peak in the range $0.15 < \rho < 0.3$. Figures 6.6 and 6.15 show the density distributions for $l = 15$ and $l = 12$ respectively in the range $0.0 < \rho < 0.4$.

For $l = 15$ the density distribution turns upwards at $\rho = 0.05$ and rises towards a peak at $\rho = 0.35$. After this maximum there is a sharp drop before the regularly spaced peaks and troughs assert themselves at $\rho > 0.4$. When we look at the configurations under these features we can see that the slow growth towards the peak at $\rho = 0.35$ represents the formation of a spherical and then cylindrical cluster, while the sharp drop just before the regular peaks indicates a barrier to the formation of slabs.

The density distributions at $l = 12$ are significantly different. Instead of reaching a minimum at $\rho = 0.05$ and then growing towards a peak as larger clusters form, larger clusters are increasingly less favourable for $l = 12$ as the density increases towards $\rho = 0.2$. At $\rho = 0.2$ the cluster in the system has already grown to fill the

system in one dimension and is now trying to form a lamella. This is at a much lower density than was observed for $l = 15$.

The smaller lengthscale is responsible for the lower probability of spherical cluster growth at $l = 12$. As a cluster grows, it begins to feel the repulsion from its image in the periodic boundary sooner for $l = 12$ than for $l = 15$. It may well be the case that for $l = 12$ the system is small enough that spherical cluster nucleation is energetically unfavourable for all cluster sizes until lamellae start to form, which would explain the lack of a cluster peak in the density distributions at $l = 12$.

Similarly one can argue that lamellea form at lower densities since the lower surface area to volume ratio of the simulation box means that fewer particles are needed to form a full layer that spans the lengthscale of the simulation in two dimensions.

As a final addition to this investigation, we decided to obtain density distributions for $l = 20$, to confirm that the density distribution structure that was seen previously is preserved when using a much larger system. Unfortunately, due to the large system size and deep attractive potential, simulations at $l = 20$ took a long time to run on the hardware available and as a result we were only able to obtain a single density distribution for $l = 20$ at $\epsilon = 3.1$, shown in figure 6.16. We were unable to obtain configurational data for this distribution due to time constraints. Since only one density distribution was obtained there is little that can be concluded from this data, but the structure of the $l = 20$ density distribution is reminiscent of those for $l = 12$ and $l = 15$, which does indicate that the structures observed at those system sizes are still present and are not just caused by finite size effects.

6.6 Conclusions

In this chapter we have seen that for attractive strengths of $\epsilon > 3.1$, the heterogeneous structures seen previously are replaced by a gas-liquid first order phase transition. The gas and liquid phases appear as peaks at $\rho = 0.0$ and $\rho = 1.0$ and the intervening region occupies a wide range of ρ with very low probability, such that transitions happen only rarely. Plotting the mean density $\overline{\rho}(\mu)$ reveals that the apparent location of the phase transition is strongly dependent on the system's

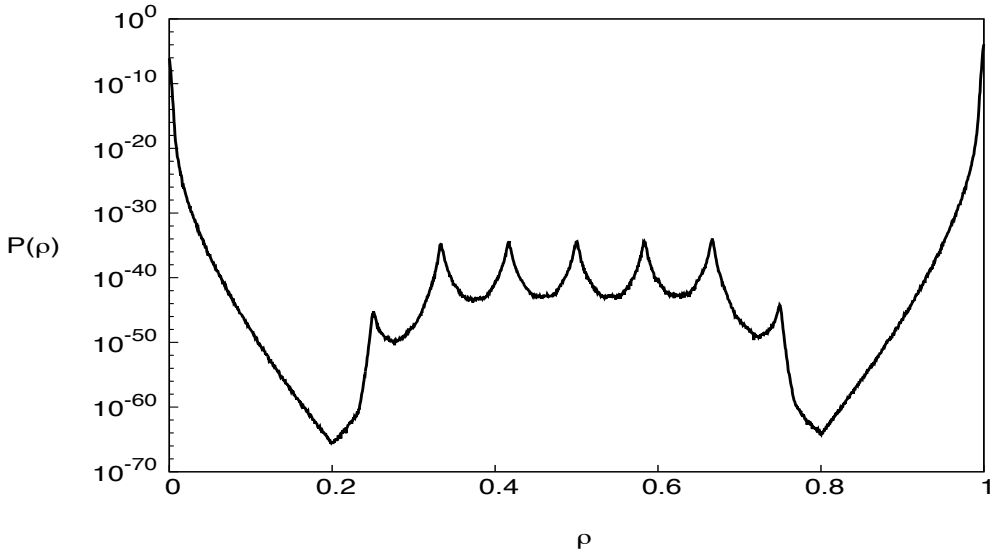

Figure 6.11: Density distribution function for $A = 1.0$, $\epsilon = 3.3$, $\mu = -8.235$, with a system length of $l = 12$ plotted on a log scale. The low probability peaks in the range $0.2 < \rho < 0.8$ are reminiscent of those seen for larger system sizes (section 6.2).

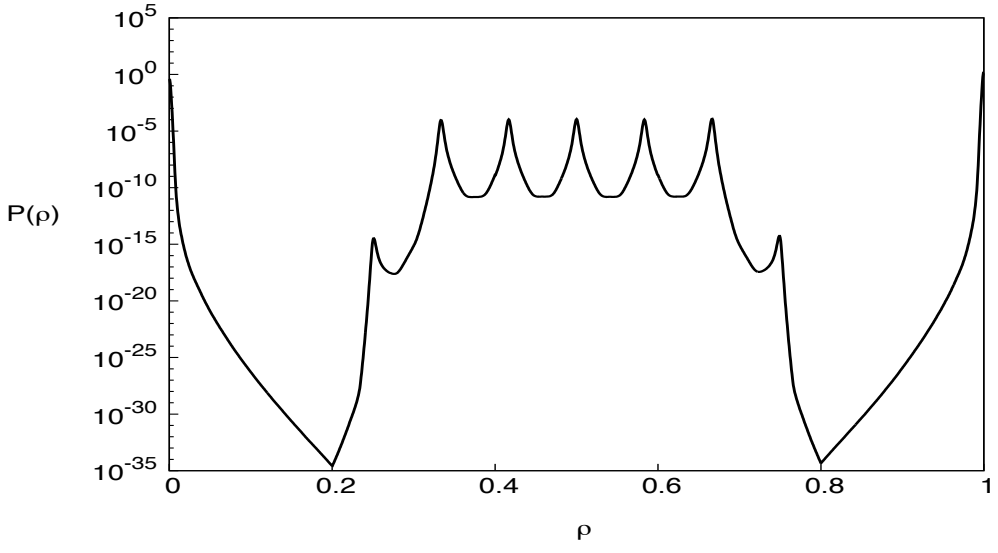

Figure 6.12: Density distribution function for $A = 1.0$, $\epsilon = 3.2$, $\mu = -7.574$, with a system length of $l = 12$ plotted on a log scale. The peaks in the range $0.2 < \rho < 0.8$ have probabilites on the order of those of the gas and liquid peaks.

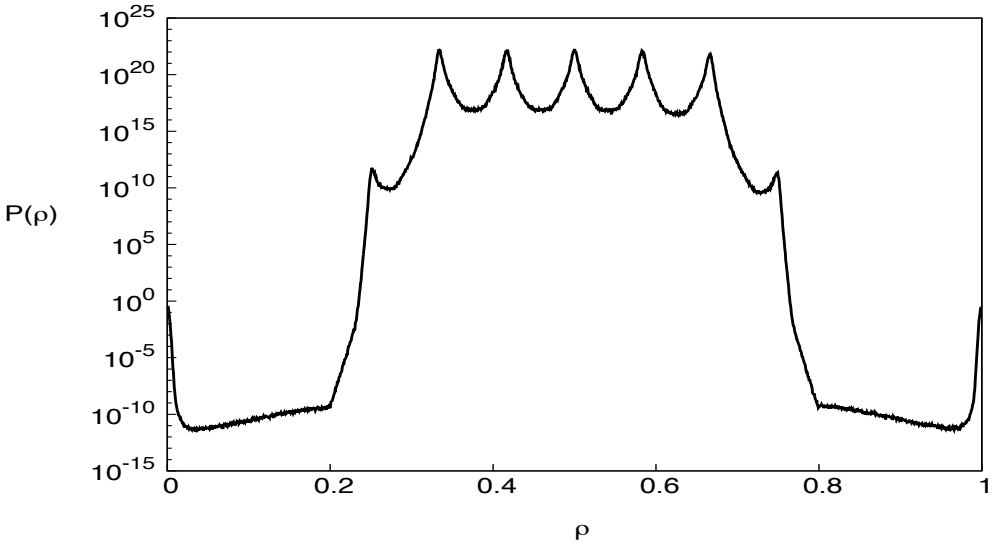

Figure 6.13: Density distribution function for $A = 1.0$, $\epsilon = 3.1$, $\mu = -6.912$, with a system length of $l = 12$ plotted on a log scale. The peaks in the range $0.2 < \rho < 0.8$ now have much higher probabilities than the gas and liquid peaks.

initial configuation. This hysteresis effect speaks to the existence of a high free-energy barrier between the two phases inside the potential barrier on acound of the low probability. Transition matrix MC, on the other hand, proved to be successful at flattening the free energy barrier and provided both density and configurational data that would have otherwise been unavailable.

Using this data we were able to observe that the heterogeneous structures seen for systems with weaker attractive strengths were still accessible to the system, albeit with very low probabilities relative to the homogeneous gas and liquid phases. Investigation into the types of configurations found in the system under certain (low probability) features of the resulting density distributions revealed insights into the mechanism of formation of somee heterogeneous structures and the transitions between them, such as the growth of lamellae via layer aggregation.

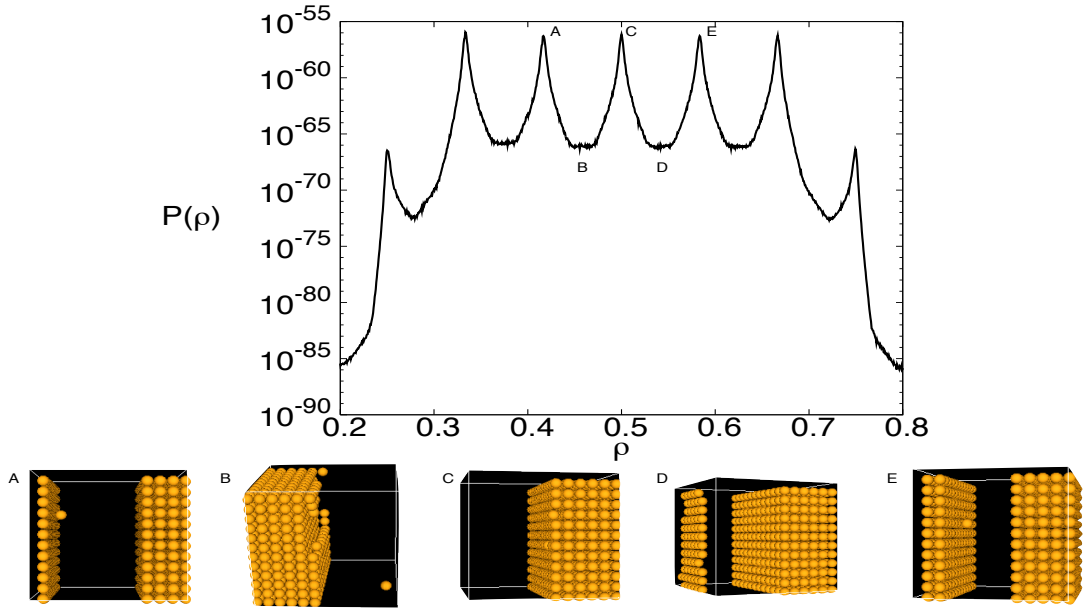

Figure 6.14: System configurations for $A = 1.0$, $\epsilon = 3.3$, $\mu = -8.235$, $l = 12$, in the range $0.2 < \rho < 0.8$, showing lamella structures.

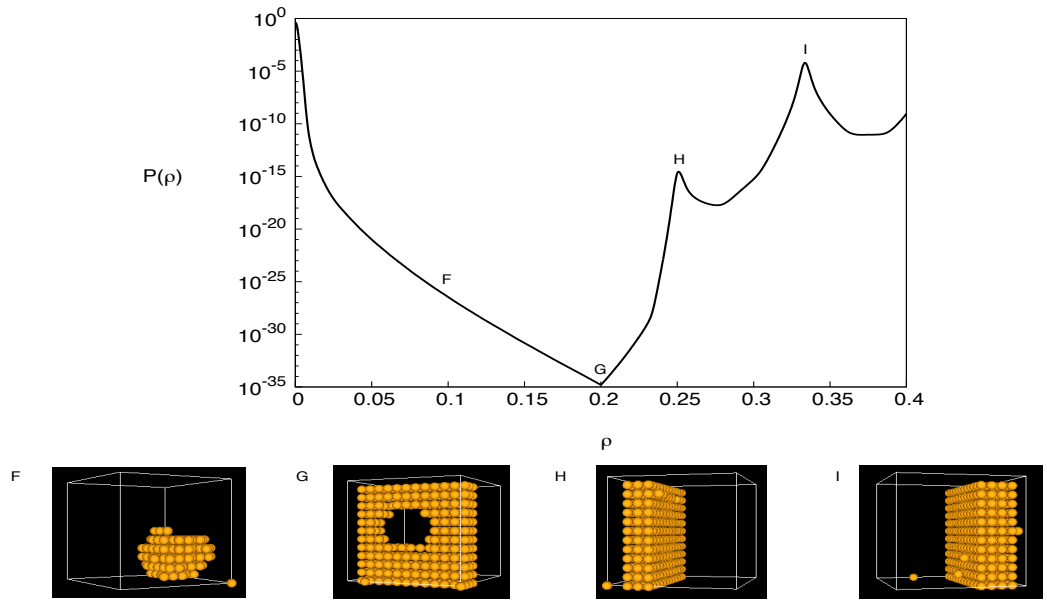

Figure 6.15: System configurations for $A = 1.0$, $\epsilon = 3.2$, $\mu = -7.574$, $l = 12$, in the range $0.0 < \rho < 0.4$, showing the barrier configurations before lamellea form.

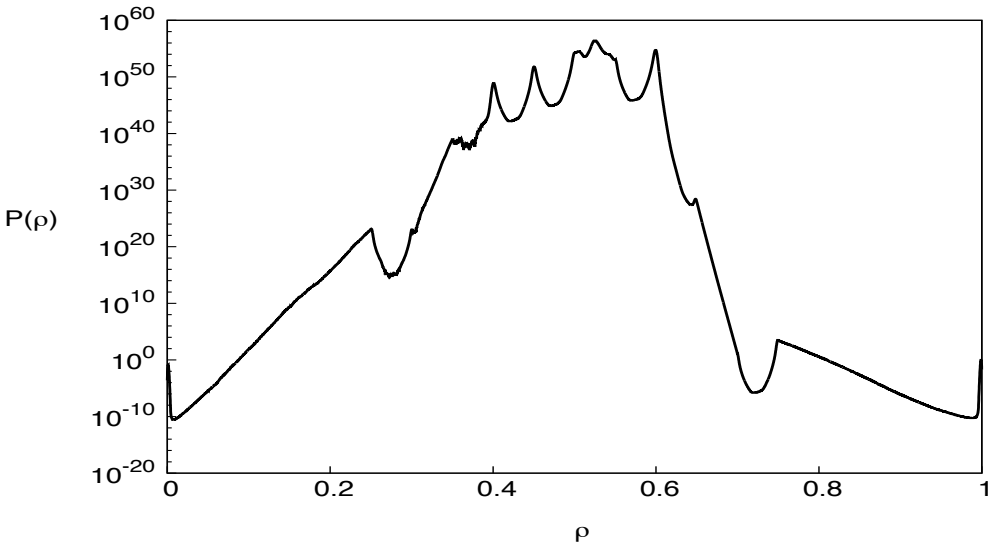

Figure 6.16: Density distribution function for $A = 1.0$, $\epsilon = 3.1$, $\mu = -6.899$ with a system length of $l = 20$.

Chapter 7

Conclusions

‘ Lattice based Monte Carlo (MC) simulations in the Grand Canonical ensemble have been used throughout this thesis to investigate the equilibrium phase behaviour of hard - core fluids with competing short - ranged attractive and long - ranged repulsive Yukawa potentials (HC2YFs). These simulations have provided more direct information regarding the exact structure of such systems under different conditions that the integral equation theories (IETs) used by much of the existing literature on the subject, while the lattice - based nature of the simulations enabled us to mitigate much of the computational expence which has limited pevious MC studies.

Beginning from a potential with zero repulsion ($A = 0$) , the phase behaviour of the fluid shows good agreement with that of the Ising lattice gas. This agreement worsens as the repulsive strength increases, eventually leading to a stabilisation of the heterogeneous structures at the Lifshitz point.

When in the region of heterogenous stability, observations of the density distrbibutions from MC simulations reveals a double - peaked structure at gas - cluster and liquid - bubble coincidence. The presence of these peaks and the deep valley between them indicates the existence of a high free - energy barrier to cluster / bubble formation. This was in a manner similar to classical nucleation theory (CNT) with the exception that the maximum cluster size could be tuned such that it was smaller than the system lengthscale, in contrast to CNT which predicts that clusters will grow to fill the system.

When the strength of the attractive potential is high relative to that of the re-

pulsive potential, the heterogeneous structures lose stability and the gas - liquid phase transition reasserts itself with a high free - energy barrier between the two phases. While configuartions inside the barrier are inaccessible to normal MC simulations on account of their extremely low relative probability, transiton matrix MC simulations revealed that the system configurations which occur inside the barrier are qualitatively similar to the configurations seen in the region of heterogeneous stability. Data from transition matrix MC simulations revealed much about the mechanism for the formation of heterogeneous structures, demonstrating the importance of thesurface area to volume ratio in determining the maximum stable cluster size and the process of lamella growth by surface aggregation. Similar results were seen for multiple system sizes, however computational considerations limited the maximum system size that could be simulated in a reasonable time frame.

Future studies may wish to undertake a deeper investigation into the nature of the phase diagram in the vicinity of the Lifshitz point. Tracking the movement of the critical point as the repulsive strength varies. Observations of the gas - cluster and liquid - bubble lines as the attractive strength is reduced may also prove fruitful. There is some evidence in the data presented here to suggest that the free - energy barrier to cluster formation would reduce as the attractive strength fell. Determining if that trend would simply continue until one reached a single phase region, or if there is a critical point, would be of great interest. Simulations of very large systems would help to shed light on the true impact of finite size effects. However, due to the cost of such simulations, such an investigation would require far greater computational power than was available for this investigation, unless significant savings could be made either through model approximations or by optimising the simulation algorithm.

Bibliography

[1] M. Seul and D. Andelman, "Domain shapes and patterns: The phenomonology of modulated phases," *Science*, vol. 267, p. 476, 1995.

[2] R. P. Sear and W. M. Gelbart, "Microphase separation versus the vapor-liquid transition in systems of spherical particles," *J. Chem. Phys.*, vol. 110, no. 9, p. 4582, 1999.

[3] A. J. Archer, C. Ionescu, D. Pini, and L. Reatto, "Theory for the phase behaviour of a colloidal fluid with competing interactions," *J. Phys.: Condens. Matter*, vol. 20, p. 415106, 2008.

[4] A. Ciach and W. Gozdz, "Mesoscopic description of network-forming clusters of weakly charged colloids," *Condensed Matter Physics*, vol. 13, pp. 23603: 1–12, March 2010.

[5] A. J. Archer and N. B. Wilding, "Phase behaviour of a fluid with competing attractive and repulsive interactions," *Phys. Rev. E*, vol. 76, p. 031501, 2007.

[6] M. M. Tsypin and H. W. J. Blote, "Probability distribution of the order parameter for the three-dimensional ising-model universality class: A high-precision monte carlo study," *Phys. Rev. E*, vol. 62, p. 73, July 2000.

[7] M. Allen and D. Tildesley, *Computer Simulation of Liquids*, ch. 2, p. 33. Oxford Science Publications, 1987.

[8] S. J. Blundell and K. M. Blundell, *Concepts in Thermal Physics*, ch. 4, pp. 34–36. Oxford University Press, 2008.

[9] S. J. Blundell and K. M. Blundell, *Concepts in Thermal Physics*, ch. 4, p. 36. Oxford University Press, 2008.

[10] S. J. Blundell and K. M. Blundell, *Concepts in Thermal Physics*, ch. 4, pp. 36–38. Oxford University Press, 2008.

[11] S. J. Blundell and K. M. Blundell, *Concepts in Thermal Physics*, ch. 4, p. 37. Oxford University Press, 2008.

[12] S. J. Blundell and K. M. Blundell, *Concepts in Thermal Physics*, ch. 16, p. 168. Oxford University Press, 2008.

[13] S. J. Blundell and K. M. Blundell, *Concepts in Thermal Physics*, ch. 28, p. 308. Oxford University Press, 2008.

[14] S. J. Blundell and K. M. Blundell, *Concepts in Thermal Physics*, ch. 28, p. 320. Oxford University Press, 2008.

[15] J. M. Yeomans, *Statistical Mechanics of Phase Transitions*, ch. 2, p. 21. Oxford Science Publications, 1992.

[16] D. Frenkel and B. Smit, *Understanding Molecular Simulations*, ch. 3, pp. 35–39. Oxford University Press, 2008.

[17] L. S. Ornstein and F. Zernike *Proc. Acad. Sci. (Amsterdam)*, vol. 17, p. 793, 1914.

[18] R. Balescu, *Equilibrium and Nonequilibrium Statistical Mechanics.* Wiley, 1975.

[19] *Theory of Simple Liquids.* Academic Press, 1976.

[20] J. M. J. V. Leeuwen, J. Groenveld, and J. D. Boar *Physica*, vol. 25, p. 792, 1959.

[21] E. Meeron *J Math Phys*, vol. 1, p. 192, 1960.

[22] T. Morita *Progr Theor Phys*, vol. 23, p. 829, 1960.

[23] G. S. Rushbrooke *Physica*, vol. 26, p. 259, 1960.

[24] L. Verlet *Il Nuovo Ciento*, vol. 18, p. 77, 1960.

[25] E. W. Montroll and J. E. Mayer *J Chem Phys*, vol. 9, p. 626, 1941.

[26] J. E. Mayer *J Chem Phys*, vol. 18, p. 1426, 1950.

[27] G. S. Rushbrooke and H. I. Scoins *Proc Roy Soc (London)*, vol. A216, p. 203, 1953.

[28] T. Morita and K. Hiroike, "A new approach to the theory of classical fluids. i," *Progress of Theoretical Physics*, vol. 23, no. 6, p. 1003, 1960.

[29] C. Caccamo, "Integral equation theory description of phase equilibria in classical fluids," *Physics Reports*, vol. 274, no. 1, pp. 1–105, 1996.

[30] J.-M. Bomont, J.-L. Bretonnet, and D. Costa, "Temperature study of cluster formation in two-yukawa fluids," *J Chem Phys*, vol. 132, p. 184508, 2010.

[31] G. Zerah and J. P. Hansen, "Self-consistent integral equations for fluid pair distribution functions: Another attempt," *J Chem Phys*, vol. 84, no. 4, p. 2336, 1986.

[32] F. J. Rogers and D. A. Young, "New, thermodynamically consistent, integral equation for simple fluids," *Physical Review A*, vol. 30, no. 2, p. 999, 984.

[33] J. M. Kim, R. Castaneda-Priego, Y. Liu, and N. J. Wagner, "On the importance of thermodynamic self-consistency for calculating clusterlike pair correlations in hard-core double yukawa fluids," *J Chem Phys*, vol. 134, p. 064904, 2011.

[34] A. Imperio and L. Reatto, "A bidimensional fluid system with competing interactions: spontaneous and induced pattern formation," *J. Phys.: Condens. Matter*, vol. 16, pp. S3769–S3789, 2004.

[35] Y. Levin and K. A. Dawson, "Fluctuation-induced transitions in an isotropic spatially frustrated lattice model," *Physical Review A*, vol. 42, no. 4, p. 1976, 1990.

[36] E. A. Jagla *J Chem Phys*, no. 111, p. 8980, 1999.

[37] N. B. Wilding and J. E. Magee *Phys Rev E*, no. 66, p. 031509, 2002.

[38] H. M. Gibson and N. B. Wilding *Phys Rev E*, no. 73, p. 061507, 2007.

[39] B. M. Mladek *Phys Rev Lett*, no. 96, p. 045701, 2006.

[40] G. Malescio and G. Pellicane *Nature Materials 2*, no. 97.

[41] R. P. Sear and D. Frenkel *Phys Rev Lett*, no. 90, p. 195701, 2003.

[42] P. J. Camp *Phys Rev E*, no. 68, p. 061506, 2003.

[43] D. Pini, A. Parola, and L. Reatto, "Freezing and correlations in fluids with competing interacions," *J. Phys.: Condens. Matter*, vol. 18, p. S2305, 2006.

[44] A. Stradner, H. Sedgwick, F. Cardinaux, W. C. K. Poon, S. U. Egelhaaf, and P. Schurtenberger, "Equilibrium cluster formation in concentrated protein solutions and colloids," *Nature*, vol. 432, p. 492, 2004.

[45] H. Sedgwick, S. U. Egelhaaf, and W. C. K. Poon *J Phys: Condens Matter*, no. 16, p. S4913, 2004.

[46] A. I. Campbell, V. J. Anderson, J. S. van Duijneveldt, and P. Bartlett, "Dynamical arrest in attracive colloids: The effect of long-range repulsion," *Physical Review Letters*, vol. 94, p. 208301, 2005.

[47] R. Sanchez and P. Bartlett *J Phys: Condens Matter*, no. 17, p. S3551, 2005.

[48] R. P. Sear, S.-W. Chung, G. Markovich, W. M. Gelbart, and J. R. Heath, "Spontaneous patterning of quantum dots at the air-water interface," *Physical Review E*, vol. 59, no. 6, p. R6255, 1999.

[49] D. Andelman, F. Brochard, and J. F. Joanny, "Phase transitions in langmuir monolayers of polar molecules," *J. Chem. Phys.*, vol. 86, p. 3673, March 1987.

[50] A. Ciach, "Universal sequence of ordered structures obtained from mesoscopic description of self-assembly," *Physical Review E*, vol. 78, p. 061505, 2008.

[51] J. Fraxedas, S. Garcia-Gil, S. Monturet, N. Lorente, I. Fernandez-Torrente, K. J. Franke, J. I. Pascual, A. Vollmer, R. P. Blum, N. Koch, and P. Orderjon, "Modulation of surface charge transfer through competing long-range repulsion versus short-range attractive interactions," *J. Phys. Chem. C*, vol. 115, pp. 18640–18648, 2011.

[52] E. Mani, E. Sanz, P. G. Bolhuis, and W. K. Kegel, "Stabilisation of nanoparticle shells by competing interactions," *J Phys Chem C*, vol. 114, pp. 7780–7786, 2010.

[53] A. Malins, S. R. Williams, J. Eggers, H. Tanaka, and C. P. Royall, "Geometric frustration in small colliodal clusters," *J. Phys.: Condens. Matter*, vol. 21, p. 425103, 2009.

[54] C. P. Royall, D. G. A. L. Aarts, and H. Tanaka, "Fluid structure in colloid-polymer mixtures: the competition between electrostatics and depletion," *J. Phys.: Condens. Matter*, vol. 17, pp. S3401–S3408, November 2005.

[55] P. N. Segre, V. Prasad, A. B. Schofield, and D. A. Weitz, "Glasslike kinetic arrest at the colloidal-gelation transition," *Phys. Rev. Lett.*, vol. 86, no. 26, p. 6042, 2001.

[56] F. L. Verso, C. N. Likos, and L. Reatto *Progr. Colloid Polym. Sci.*, vol. 133, p. 78, 2006.

[57] D. Chandler, "Two faces of water," *Nature*, vol. 417, p. 491, 2002.

[58] M. W. Deem and D. Chandler, "Charge-frustrated model of bicontinuous phases," *Physical Review E*, vol. 49, p. 4268, May 1994.

[59] M. W. Deem and D. Chandler, "Formation of interfaces in bicontinuous phases," *Physical Review E*, vol. 49, p. 4276, May 1994.

[60] L. Maibaum, A. R. Dinner, and D. Chandler, "Micelle formation and the hydrophobic effect," *J Phys Chem B*, vol. 108, no. 21, p. 6778, 2004.

[61] P. H. Nelson, G. C. Rutledge, and T. A. Hatton, "On the size and shape of self-assembled micelles," *J. Chem. Phys.*, vol. 107, p. 10777, December 1997.

[62] A. Z. Panagiotopoulos, M. A. Floriano, and S. K. Kumar, "Micellization and phase separation of diblock and triblock model surfactants," *Langmuir*, vol. 18, pp. 2940–2948, 2002.

[63] L. B. Partay, P. Jedlovszky, I. Brovchenko, and A. Oleinikova, "Formation of mesoscopic water networks in aqueous systems," *Physical Chemistry Chemical Physics*, vol. 9, pp. 1341–1346, 2007.

[64] S. A. Sanders and A. Z. Panagiotopoulos, "Micellization of behavior of coarse grained surfactant models," *J Chem Phys*, vol. 132, p. 114902, 2010.

[65] H.-J. Woo, C. Carraro, and D. Chandler, "Quantitative molecular interpretation of mesoscopic correlations in bicontinuous microemulsions," *Physical Review E*, vol. 52, p. 6497, December 1995.

[66] A. J. Archer, D. Pini, R. Evans, and L. Reatto, "A model colloidal fluid with competing attractive and repulsive interactions: bulk and interfacial properties," *J. Chem. Phys.*, vol. 126, p. 014104, January 2007.

[67] J.-L. Barrat and J.-P. Hansen, *Basic Concepts for Simple and Complex Liquids*. Cambridge University Press, Cambridge, 2003.

[68] J. Chakrabarti, S. Chakrabarti, and H. Lowen *J. Phys.: Condens. Matter*, vol. 18, p. L81, 2006.

[69] F. Ghezzi and J. C. Earnshaw *J. Phys.: Condens. Matter*, vol. 9, p. L517, 1997.

[70] G. H. Fredrickson and E. Helfand, "Fluctuation effects in the theory of microphase separation in block copolymers," *J. Chem. Phys.*, vol. 87, p. 697, 1987.

[71] C. R. Safinya, "Structures of lipid-dna complexes: supramolecular assembly and gene delivery," *Current opinion in Structural Biology*, no. 11, pp. 440–448, 2001.

[72] J.-M. Caillol, O. Patsahan, and I. Mryglod, "Statistical field theory for simple fluids: The collective variables representation," *Physica A*, vol. 386, pp. 326–344, 2006.

[73] M. Muller and M. Schick, "Ordered phases in rod-coil diblock copolymers," *Macromolecules*, vol. 29, p. 8900, 1996.

[74] F. Sciortino, S. Mossa, E. Zaccarelli, and P. Tartaglia, "Equilibrium cluster phases and low-density arrested disordered states: The role of short-range attraction and long-range repulsion," *Phys. Rev. Lett.*, vol. 93, p. 0055701, July 2004.

[75] H. ge Tan, Z. yu Wang, W. fang Zhu, Q. gong SOng, H. Li, and C. qin Bai, "Structure evolution of the cylindrical phase of diblock copolymers in films," *Chinese Journal of Polymer Science*, vol. 26, no. 6, pp. 759–766, 2008.

[76] A. M. Ferrenberg and R. H. Swendsen, "New monte carlo technique for studying phase transitions," *Phys. Rev. Lett.*, vol. 61, pp. 2635–2638, 1988.

[77] R. K. W. Spencer and R. A. Wickham, "Simulation of nucleation dynamics at the cylinder-to-lamellar transition in a diblock copolymer melt," *Soft Matter*, vol. 9, p. 3373, 2013.

[78] A. J. Archer and R. Evans, "Nucleation of liquid droplets in a fluid with competing interactions," *Molecular Physics*, vol. 109, pp. 2711–2722, December 2011.

[79] Y. Liu, W.-R. Chen, and S.-H. Chen, "Cluster formation in two-yukawa fluids," *J. Chem. Phys.*, vol. 122, p. 044507, January 2005.

[80] T. Li, P. Zhang, and W. Zhang, "Nucleation rate calculation for the phase transtion of diblock copolymers under stochastic cahn-hilliard dynamics," *Multiscale Model Simulations*, vol. 11, no. 1, pp. 385–409, 2013.

[81] D. Pini, G. Jialin, A. Parola, and L. Reatto, "Enhanced density fluctuations in fluid systems with competing interactions," *Chemical Physical Letters*, vol. 327, pp. 209–215, 2000.

[82] S. Zhao and J. Wu, "An efficient method for accurate evaluation of the site-site direct correlation functions of molecular fluids," *Molecular Physics*, vol. 109, pp. 2553–2564, 2011.

[83] J. Groenewold and W. K. Kegel, "Anomalously large equilibrium clusters of colloids," *J Phys Chem B*, vol. 105, pp. 11702 –11709, May 2001.

[84] J. Groenewold and W. K. Kegel, "Colloidal cluster phases, gelation and nuclear matter," *J. Phys.: Condens. Matter*, vol. 16, pp. S4877–S4886, October 2004.

[85] A. J. Archer, C. N. Likos, and R. Evans, "Soft-core binary fluid exhibiting a lambda-line and freezing to a highly delocalized crystal," *Journal of Physics Condensed Matter*, vol. 16, no. 23, pp. L297–L303, 2004.

[86] D. Pini, G. Stell, and N. B. Wilding, "A liquid-state theory that remains successful in the critical region," *Molecular Physics*, vol. 95, no. 3, pp. 483–494, 1998.

[87] J. S. Hoye, E. Lomba, and G. Stell *Molecular Physics*, vol. 79, p. 523, 1993.

[88] L. Belloni *J Chem Phys*, vol. 98, p. 8080, 1993.

[89] A. G. Schlijper, M. M. T. da Gama, and P. G. Ferreira *J Chem Phys*, vol. 98, p. 1534, 1992.

[90] P. G. Ferreira, R. L. Carvalho, M. M. T. da Gama, and A. G. Schlijper *J Chem Phys*, vol. 101, p. 594s, 1994.

[91] J. M. Yeomans, *Statistical Mechanics of Phase Transitions.* Oxford Science Publications, 1992.

[92] A. Parola and L. Reatto, "Hierarchical reference theory of fluids and the critical point," *Physical Review A*, vol. 31, p. 3309, May 1985.

[93] A. Parola and L. Reatto, "Liquid state theories and critical phenomena," *Adv. Phys.*, no. 44, p. 211, 1995.

[94] G. Fredricksen, V. Ganesan, and F. Drolet, "Field-theoretic computer simulation methods for polymers and complex fluids," *Macromolecules*, no. 35, p. 16, 2002.

[95] M. Mueller, K. Katsov, and M. Schick, "Biological and synthetic membranes: What can be learned from a coarse-grained description?," *Phys. Rep.*, no. 434, p. 113, 2006.

[96] J.-M. Bomont, J.-L. Bretonnet, D. Costa, and J.-P. Hansen, "Communication: Thermodynamic signatures of cluster formation in fluids with competing interactions," *J Chem Phys*, vol. 137, no. 011101, 2012.

[97] M. B. Sweatman, R. Fartaria, and L. Lue, "Cluster formation in fluids with competing short-range and long-range interactions," *J. Chem. Phys.*, vol. 140, p. 234508, 2014.

[98] M. Broccio, D. Costa, Y. Liu, and S.-H. Chen, "The structural properties of a two-yukawa fluid: Simulation and analytical results," *J Chem Phys*, vol. 124, p. 084501, 2006.

[99] D. Frenkel and B. Smit, *Understanding Molecular Simulation, Second Edition: From Algorithms to Applications.* Computational Science, Academic Press, 2 ed., 2001.

[100] M. P. Allen and D. J. Tildesley, *Computer Simulation of Liquids.* Oxford Science Publications, 1 ed., 1989.

[101] P. D. Godfrin, R. Castaneda-Priego, Y. Liu, and N. J. Wagner, "Intermediate range order and structure in colloidal dispersions with competing interactions," *J Chem Phys*, vol. 139, p. 154904, 2013.

[102] P. D. Godfrin, N. E. Valadez-Perez, R. Castaneda-Priego, N. J. Wagner, and Y. Liu, "Generalized phase behaviour of cluster formation in colloidal dispersions with competing interactions," *Soft Matter*, vol. 12, p. 5061, 2014.

[103] S. J. Blundell and K. M. Blundell, *Concepts in Thermal Physics*, ch. 22, p. 235. Oxford University Press, 2008.

[104] D. Frenkel and B. Smit, *Understanding Molecular Simulations*, ch. 5, pp. 126–130. Academic Press, 2nd ed., 2002.

[105] D. Frenkel and B. Smit, *Understanding Molecular Simulations*, ch. 3, pp. 29–31. Academic Press, 2nd ed., 2002.

[106] J. Largo and N. B. Wilding, "Influence of polydispersity on the critical parameters of an effective-potential model for asymmetric hard-sphere mixtures," *Phys. Rev. E*, vol. 73, p. 036115, 2006.

[107] N. B. Wilding, "Computer simulation of fluid phase transitions," *Am. J. Phys.*, vol. 69, pp. 1147–1155, November 2001.

[108] D. Frenkel and B. Smit, *Understanding Molecular Simulation*, ch. 5, p. 129. Academic Press, 2nd ed., 2002.

[109] D. Frenkel and B. Smit, *Understanding Molecular Simulation*, ch. 7, p. 184. Academic Press, 2nd ed., 2002.

[110] A. M. Ferrenberg and R. H. Swendsen, "Optimized monte carlo data analysis," *Phys Rev Lett*, vol. 63, no. 12, p. 1195, 1989.

[111] S. Auer and D. Frenkel, "Numerical prediction of absolute crystallization rates in hard-sphere colloids," *J Chem Phys*, vol. 120, p. 3015, 2004.